Fakultät für Medizin

Institut für Pharmakologie und Toxikologie

The role of Cullin-RING E3 ubiquitin ligase 7 in maladaptive cardiac remodelling

Melanie Bianca Anger

Vollständiger Abdruck der von der Fakultät für Medizin der Technischen Universität München zur Erlangung des akademischen Grades eines

Doktors der Medizin (Dr. med.)

genehmigten Dissertation.

Vorsitzender: Prof. Dr. Jürgen Schlegel

Prüfer der Dissertation:

1. Prof. Dr. Dr. Stefan Engelhardt

2. Prof. Dr. Jürgen Ruland

Die Dissertation wurde am 13.06.2019 bei der Technischen Universität München eingereicht und durch die Fakultät für Medizin am 12.02.2020 angenommen.

1 LIST OF CONTENTS

This work is dedicated to my parents Otto and Gerlinde, to my brother Christian and to my friends for infinite support and encouragement.

2 ABBREVIATIONS

AAV	Adeno-associated virus
AMCM	Adult mouse cardiomyocytes
AMCF	Adult mouse cardiofibroblasts
(m)A	(milli)Ampere
AMPK	AMP-activated protein kinase
AngII	Angiotensin II
APS	Ammonium persulfate
(k)Bp	(kilo)Base pair
BSA	Bovine Serum Albumin
Ca^{2+}	Calcium
CaMKII	Calmodulin-dependent kinase II
Cap	For *"Capsid"*, gene region of AAVs
CCDC8	Coiloided coil domain containing protein 8
CCN1	Cysteine-rich 61 (Cyr-61)
CCN2	Connective tissue growth factor (CTGF)
cDNA	Complementary deoxyribonucleic acid
Col1/3	Type I or III collagen
Cre enzyme	"Causes recombination" enzyme
CRL7	Cullin-RING E3 ubiquitin ligase 7
Ct	Cycle threshold
CUL7	Cullin7 protein
CVD	Cardiovascular disease
C57BL/6	Common inbred wildtype mouse strain
DAPI	4', 6-diamidino-2-phenylindole
DNA	Deoxyribonucleic acid
DCM	Diabetic cardiomyopathy
DMEM	Dulbecco's Modified Eagle Medium
ECM	Extracellular matrix
E. coli	Escherichia coli
EF	Ejection fraction
EMT	Epithelial-mesenchymal transition
ERK	Extracellular signal-related kinase
E1	Ubiquitin-activating enzyme
E2	Ubiquitin-transferring enzyme

E3	Ubiquitin ligase
E1A	Adenovirus early region E1A Protein
FAP68	Glomulin
FS	Fractional shortening
GH	Growth hormone
HCC	Hepatocellular carcinoma
HECT	Homologous to E6-AP COOH terminus
HIV-1	Human Immunodeficiency Virus type 1
HPK1	Hematopoietic progenitor kinase 1
HSP90	Heat shock protein 90
ICAM-1	Intercellular adhesion molecule 1
IGF-1	Insulin-like growth factor 1
IRS-1	Insulin receptor substrate 1
ITR	Inverted terminal repeat sequence
JNK	C-Jun N-terminal kinase
kDa	Kilodalton
LB-medium	Lysogeny broth medium
LVID	Left ventricular internal diameter
(m)M	(milli)Mole per litre
MAPK	Mitogen-activated kinase
MEF	Mouse embryonic fibroblasts
MI	Myocardial infarction
(m)l	(milli)litre
MMP	Matrix metalloproteinase
MRFAP1	MORF4 family-associated protein 1
mRNA	Messenger ribonucleic acid
mTOR	Mammalian target of rapamycin
NFAT	Nuclear factor of activated T cells
(n/m)g	(nano/milli)gram
nm	Nanometre
Obsl1	Obscurin-like 1
PBS(T)	Phosphate-buffered saline (with Tween 20)
(qRT-)PCR	(real-time reverse transcription-) Polymerase chain reaction
PEI	Polyethyleneimine
Pen / Strep	Penicillin / Streptomycin
PFA	Paraformaldehyde

PI3K	Phosphoinositide 3-kinase
PTEN	Phosphatase and tensin homologue
Rabl3	Rab-like protein 3
Rep	For *"Replication"*, gene region of AAVs
RING	Really interesting new gene
RhoA	RhoA GTPase
RNA	Ribonucleic acid
ROCK	Rho-associated protein kinase
ROC1	Regulator of cullins-1
Rpl32	Ribosomal protein L32
rpm	Rounds per minute
SASP	Senescent associated secretory phenotype
SCF complex	Skp, Cullin, F-box containing complex
SDS-PAGE	Sodium dodecyl sulfate polyacrylamide gel electrophoresis
SH2	Src homology 2
Skp1	S-phase kinase-associated protein 1
SV40 LT	Simian virus 40 large T antigen
SR/ FG	Sirius Red/ Fast Green
S6K1	p70 ribosomal S6 kinase 1
TAC	Transverse aortic constriction
TAK1	Transforming growth factor beta-activated kinase 1
TB-medium	Terrific broth medium
TBC1D	Tre-2/Bub2/Cdc16 domain family, member 1
TGF-β	Transforming growth factor-β
TIMP	Tissue inhibitor of metallopeptidase
TRPC	Transient receptor potential cation channel
TUNEL	Terminal deoxynucleotidyl transferase dUTP nick end labelling
Ub	Ubiquitin
UPS	Ubiquitin-proteasome system
(k)V	(kilo)Volt
VEGF-B	Vascular endothelial growth factor-B
WGA	Wheat germ agglutinin
5-ROX	Fluorophore 5-carboxyrhodamin
µl	Microlitre

ILLUSTRATION DIRECTORY

List of figures

List of tables

3 SUMMARY / ZUSAMMENFASSUNG

SUMMARY

In this thesis, the role of the Cullin-RING E3 ubiquitin ligase 7 (CRL7) as molecular scaffold protein of the Cullin-RING E3 ubiquitin ligase 7 complex was investigated in the heart using a mouse model. The CRL7 complex constitutes an important part of the ubiquitin-proteasome system leading to degradation of numerous substrates such as IRS-1, which can be involved in the pathogenesis of several cardiac disorders. On this account, a cardiomyocyte-specific deletion of the gene for the Cullin7 protein (CUL7) was achieved by intrapericardial delivery of a Cre recombinase-encoding adeno-associated virus of the serotype 9 (AAV9-CMV-iCre) in 4-5 days old male mice. The recombination event and the subsequent loss of Cul7 after successful expression of the Cre enzyme were achieved by transduction of transgenic mice harbouring a floxed *Cul7* allele (Cul7$^{flox/flox}$). The effects of *Cul7* ablation were investigated both under basal conditions and under cardiac disease conditions, i.e. sustained pressure overload modelled by transverse aortic constriction (TAC) for a time period of 3 weeks. Cardiac phenotyping with an assessment of cardiac function and heart hypertrophy as well as of fibrogenesis and apoptosis was performed. Moreover, underlying signalling pathways were characterized. For all experiments, AAV9-CMV-dsRed or lactated Ringer's solution injected littermate mice served as controls.

Under basal conditions at the age of 8 weeks, freshly isolated adult mouse cardiofibroblasts (AMCF) displayed unaltered *Cul7* mRNA levels, whereas a decrease by approx. 61 % of *Cul7* mRNA was detectable in adult mouse cardiomyocytes (AMCM), in line with the cardiomyocyte tropism of the AAV serotype 9. Furthermore, the protein abundance of CUL7 in AMCMs was reduced by ~80 %. Cardiac phenotyping showed a tendency towards increased heart weight but no amelioration of heart function and cardiac output. In addition, histological analyses concerning the development of cardiac hypertrophy and fibrosis did not display any significant alterations. Moreover, protein kinase B (AKT), extracellular signal-related kinase (ERK), and insulin receptor substrate 1 (IRS-1) protein expression levels were examined in AMCMs, where the phospho-AKT (p-AKT) / total-AKT (t-AKT) ratio was found to be upregulated by the factor of 3. Interestingly, ERK and IRS-1 protein levels remained unchanged.

Under disease conditions (TAC for 3 weeks), cardiac morphology, heart function and cross-sectional area as an indicator of cardiomyocyte hypertrophy were found to be unaltered in the different cohorts. Cardiomyocyte-specific deletion of Cul7 significantly prevented cardiomyocyte apoptosis and interstitial fibrosis under sustained pressure overload. Subsequently, different key factors of cardiac fibrogenesis were screened via qPCR. Results

demonstrated that depletion of Cul7 was associated with a diminution of *Transforming growth factor-β (Tgf-β)* mRNA abundance.

This thesis provides evidence for a regulatory role of the Cullin-RING E3 ligase 7 complex in the mammalian heart. Mechanistically CUL7 may constitute a novel regulator of cardiac interstitial fibrosis in the diseased heart by affecting cellular signalling pathways including PI3K/AKT, thereby leading to less apoptosis of cardiomyocytes and reduced formation of TGF-β.

ZUSAMMENFASSUNG

Die Rolle der Cullin-RING E3 Ubiquitin Ligase 7 als molekularer Grundbaustein des Cullin-RING E3 Ubiquitin Ligase 7 Komplexes wurde anhand eines kardialen Mausmodells als Gegenstand dieser Arbeit untersucht. Der CRL7 Komplex stellt einen wichtigen Bestandteil des Ubiquitin-Proteasom Systems dar, welches zum proteolytischen Abbau einer Vielzahl von Substraten, wie zum Beispiel von IRS-1, führt. Diese können wiederrum an der Pathogenese einiger Herzerkrankungen beteiligt sein. Um die Funktion von CUL7 im Herzen in vivo aufzuklären, wurde eine kardiomyozyten-spezifische Depletion des Genlokus des Cullin7 Proteins durchgeführt. Hierfür wurde intraperikardial ein Adeno-assoziiertes Virus des Serotyps 9 (AAV9), welcher eine Cre-Rekombinase exprimiert, in neonatalen männlichen Mäusen im Alter von 4-5 Tagen appliziert. Durch die gezielte Injektion von Mäusen, welche ein homozygot gefloxtes Allel für *Cul7* ($Cul7^{flox/flox}$) tragen, kann nach Expression der Cre-Rekombinase eine erfolgreiche Rekombination mit konsekutiver Depletion von Cul7 stattfinden. Folgend wurden die Auswirkungen der Ablation von *Cul7* unter physiologischen Konditionen als auch unter pathologischen Bedingungen im Rahmen einer druckinduzierten Herzinsuffizienz durch eine dreiwöchige, artifiziell herbeigeführte Konstriktion der Aorta untersucht. Es wurde eine kardiale Phänotypisierung mittels transthorakaler Echokardiographie, sowie durch Bestimmung von Parametern der kardialen Hypertrophie, Fibrose und Apoptose durchgeführt. Darüber hinaus wurden zugrundeliegende Signalwege charakterisiert. Als Kontrollgruppen dienten Wurfgeschwister, die entweder mit AAV9-CMV-dsRed oder Ringer-Laktat-Lösung injiziert wurden.

Unter basalen Bedingungen zeigten frisch isolierte Kardiofibroblasten von adulten Mäusen im Alter von 8 Wochen unveränderte mRNA Expressionslevel von *Cul7*, wohingegen in den Kardiomyozyten eine Reduktion von ca. 61 % beobachtet werden konnte. Diese Ergebnisse finden sich im Einklang mit dem Kardiomyozyten-Tropismus des AAV9. Darüber hinaus konnte in der kardialen Phänotypisierung eine Tendenz zur makroskopischen Herzhypertrophie, aber keine Verbesserung der linksventrikulären Funktion dargestellt werden. Auch histologische

Analysen bezüglich der kardialen Hypertrophie und Fibrosierung zeigten keine signifikanten Unterschiede zwischen der Test- und Kontrollgruppe. Zudem wurden die Expressionslevel der Proteine AKT, ERK und IRS-1 in den adulten Maus-Kardiomyozyten bestimmt, wo sich eine um den Faktor 3 hochregulierte Phosphorylierung von AKT in Relation zum gesamten AKT in den Knockout-Tieren zeigte. Interessanterweise blieben die Proteinlevel von ERK und IRS-1 gleich.

Unter kardialen Stressbedingungen für 3 Wochen zeigten die Parameter der kardialen Morphologie, der Herzfunktion sowie der Ausbildung einer kardialen Hypertrophie in den unterschiedlichen Kohorten keine signifikanten Unterschiede. Jedoch konnte dargestellt werden, dass die Depletion von Cul7 zu einer signifikanten Verringerung der kardialen Apoptose und interstitiellen Fibrose führte. Daher wurden folgend Schlüsselproteine der kardialen Fibrosebildung untersucht, wo sich eine Reduktion von *Tgf-ß* mRNA nachwiesen ließ.

Diese Erkenntnisse zeigen Hinweise für eine regulatorische Funktion des CRL7 Komplexes im Herzen auf. Im kranken Myokard könnte CUL7 durch Beeinflussung von zellulären Signalwegen wie PI3K/AKT zu verringerter Apoptose von Kardiomyozyten sowie reduzierter Bildung von TGF-ß führen und auf diesem Weg einen neuen Modulator der kardialen, interstitiellen Fibrogenese darstellen.

4 INTRODUCTION

4.1 Cardiovascular disease as the leading cause of death

Cardiovascular disease (CVD) is one of the most prevalent malignancies worldwide and its morbidity and mortality rates have increased tremendously in recent years (Mozaffarian, Benjamin et al. 2016). According to recently published data of the World Health Organization for the year 2015, ischaemic heart disease and stroke are the most common cause of death worldwide, with yearly increasing incidence during the last 15 years (WHO 2015) (**Fig. 1**). More specifically, approximately 8.8 million of 54 million deaths worldwide were caused by ischaemic cardiac disorders consisting of a large group of various maladies like angina pectoris, myocardial infarction or sudden cardiac death. Taken together, the CVD represents an immense health task as well as a large economic burden. The predicted global cost of CVD was 863 billion dollars in 2010 and it is estimated to rise to 1044 billion dollars by 2030 underlining the imperative necessity to understand the pathogenesis of CVD and to find new therapeutic strategies (Bloom DE 2011).

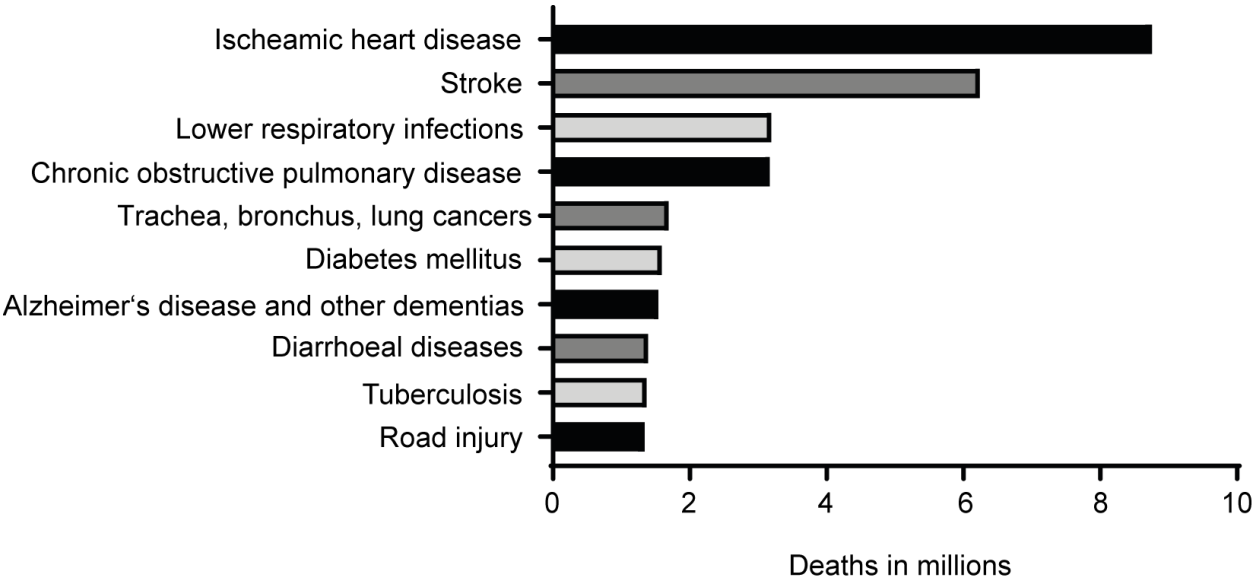

Figure 1: Top ten causes of death globally in 2015. Adopted from the global health report of the World Health Organization. Ischaemic heart disease represents the leading cause of death for approximately 15 years (WHO 2015).

4.2 Definition of heart failure and cardiac remodelling

In general, cardiovascular diseases represent a big assembly of disorders of the vessels and the heart, including coronary and congenital heart disease as well as rheumatic disorders. However, nearly all aetiologies of cardiac pathologies are associated with and exacerbated by maladaptive cardiac remodelling which leads to cardiac hypertrophy and fibrosis. In the first instance, such growth is an adaptive response to maintain cardiac function and output, preserving up blood distribution and oxygen supply to all organs. However, chronic stress or heart disease will result in ventricular dilation, decrease in contractile function and progression to heart failure over the course of time. Thus, the heart adjusts into a state of an inadequate cardiac function defined as heart failure to maintain systemic perfusion being able to satisfy the metabolic requirements of the body (Tham, Bernardo et al. 2015, Ayoub, Pothineni et al. 2017).

Initially, the term “cardiac remodelling” was used to describe the consequences of myocardial infarction regarding pump function, fibrogenesis in the infarcted myocardial region and cardiac hypertrophy (Pfeffer and Braunwald 1990). In the subsequent years, cardiac remodelling was further defined as a collection of molecular, cellular and interstitial changes that present morphologically and clinically as changes in size, mass and function. To date, two types of cardiac remodelling can be classified: physiologic remodelling in response to exercise, pregnancy or growth and pathologic remodelling in answer to heart injury or stress stimulation. It is known that similar processes like cardiac hypertrophy and fibrosis manifest after diverse types of heart injury such as pressure overload (e.g. aortic valve stenosis, hypertension), volume overload (e.g. heart valve insufficiency leading to valvular regurgitation) or inflammatory disease (e.g. myocarditis) in the maladaptive remodelling of the heart. Even if the causes of these disorders can be quite different, they have molecular, biochemical, and cellular events in common to collectively change the myocardial structures (Kehat and Molkentin 2010, Azevedo, Polegato et al. 2016).

Nonetheless, physiologic cardiac remodelling is associated with normal heart function (Shimizu and Minamino 2016). In contrast to pathological cardiac remodelling, the physiologic adaptation of the heart to an increased workload is reversible and does not result in interstitial fibrosis and finally heart failure (Wu, Xiao et al. 2017). It represents a fine-tuned and well-coordinated process of beneficial adaptations and modulations, which result in decreased cardiac wall stress, increased pump function and improved vascularization (Spaich, Katus et al. 2015). Regarding the underlying molecular mechanisms, physiological cardiac remodelling is associated with well-characterized signalling pathways, including vascular endothelial growth factor B (VEGF-B), insulin, growth hormone (GH) and insulin-like growth factor 1 (IGF-1), as well as the thyroid hormone triiodothyronine. These key mediators effectively control

cardiomyocyte contractility, sarcomere and electrical remodelling, cell survival, metabolic and mitochondrial adaptations and angiogenesis (Maillet, van Berlo et al. 2013). This beneficial homeostasis is executed by well-known cascades and down-stream targets including phosphoinositide 3-kinase/protein kinase B (PI3K/AKT), mammalian target of rapamycin (mTOR) complex, extracellular signal-regulated kinases 1 and 2 (ERK1/2) and AMP-activated protein kinase (AMPK). However, it is important to keep in mind that these downstream mediators are also relevant in maladaptive cardiac remodelling as shown in the section below which highlights only a fraction of this central topic of research (Spaich, Katus et al. 2015).

4.3 Important signalling pathways in maladaptive cardiac remodelling

Maladaptive cardiac remodelling is a leading predictor for arrhythmia, heart failure and sudden cardiac death. The deterioration of cardiac structures results from a significant disbalance in muscle growth, cell signalling and angiogenesis leading to either concentric or eccentric hypertrophy. A voluminous cardiac overload is likely to cause concentric cardiac hypertrophy whereas eccentric hypertrophy is more likely predominated by a lengthening of the cardiac myocytes at the transition to heart failure (van Berlo, Maillet et al. 2013). Generally, the distinct processes consist of myocyte loss along with compensatory cardiac hypertrophy, alteration of extracellular matrix homeostasis, perivascular as well as interstitial fibrosis, defective autophagy, metabolic abnormalities, and mitochondrial dysfunction (Schirone, Forte et al. 2017) (**Fig. 2**).

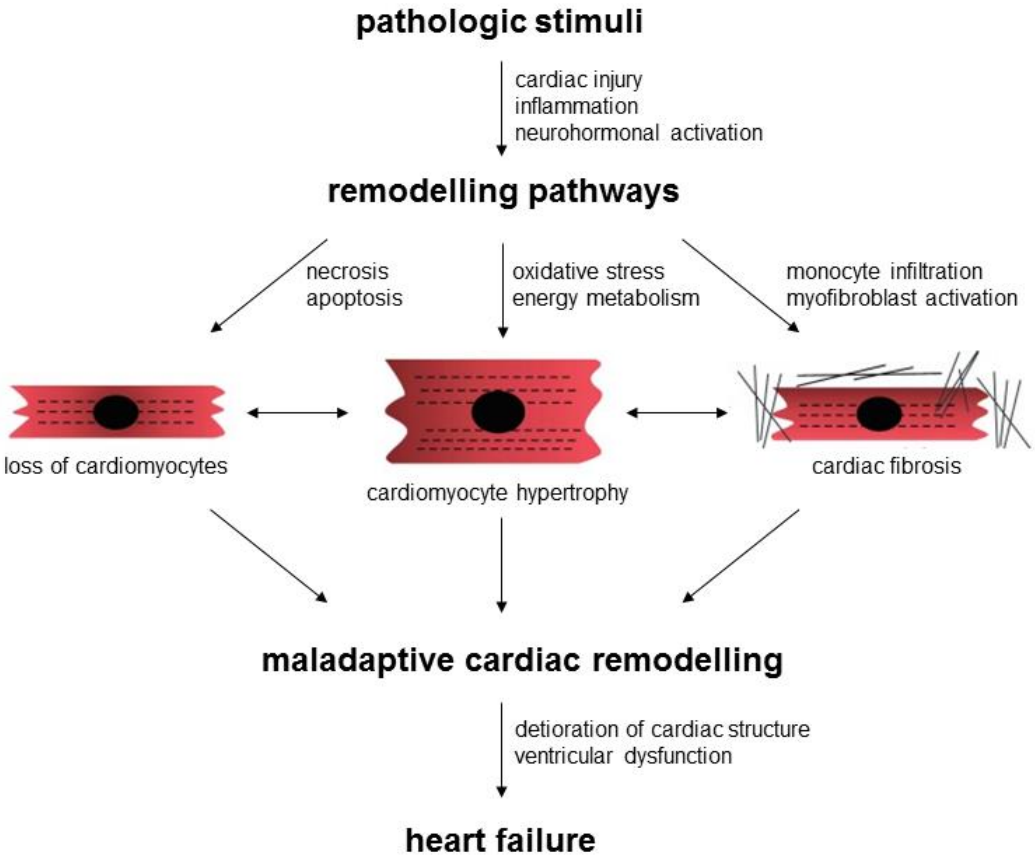

Figure 2: Overview of the main factors contributing to maladaptive cardiac remodelling. Cardiac remodelling is defined as a collection of molecular, cellular and interstitial changes that appear morphologically and clinically as changes in size, mass and function leading as main consequence to heart failure via multiple signalling pathways. Adopted from Schirone, Forte et al. 2017.

The AKT-dependent signalling pathways might be involved both in physiological and in pathological cardiac growth (Schirone, Forte et al. 2017). It was shown that cardiac-specific inducible AKT1-transgenic mice develop adaptive hypertrophy with a lack of fibrosis as well as fetal cardiac gene transduction following short-term gene induction. Nevertheless, they exhibit pathological hypertrophy and cardiomyopathy with longer periods of transgene expression. Moreover, further stimulation via AKT caused irreversible remodelling, fibrosis, and reduced angiogenesis accompanied by decreased capillary density (Shiojima, Sato et al. 2005). Among the downstream effectors of AKT, mTOR is particularly well-characterized. The inhibition of mTOR with rapamycin can prevent cardiac hypertrophy without leading to increased lethality or deterioration of cardiac function. Load-induced p70 ribosomal S6 kinase 1 (S6K1) activation and S6 phosphorylation, a key mediator of angiotensin II (AngII) carrying impact on development and progress of cardiac hypertrophy, revealed to be completely suppressed by rapamycin indicating the important role of mTOR and PI3K/AKT signalling in load-induced cardiac hypertrophy via TAC (Shioi, McMullen et al. 2003, Aoyagi and Matsui 2011). Hence,

AKT signalling plays a significant factor in maintaining cardiovascular homeostasis, with precise control of the AKT signal being required for appropriate vascular patterning and cardiac remodelling in cardiac cells.

Moreover, sustained pressure overload induces cardiac dysfunction along with changes of the extracellular matrix (ECM) such as fibrosis and vascular rarefaction which are facilitated by transforming growth factor-β (TGF-β) among other things. TGF-β is a multifunctional cytokine binding mostly to a complex of TGF-β type I and II receptors and activin or myostatin in the heart. Thus, either Smad-dependent signalling pathways such as TGF-β/MAPK or signalling pathways independent of Smad like TGF-β/Rho/ROCK can be activated. In regard to the former, the mitogen-activated protein kinase (MAPK) constitutes a family of serine/threonine kinases, including p38-MAPK, ERK1/2, and c-Jun N-terminal kinase (JNK) (Ma, Zou et al. 2017). Li and colleagues demonstrated that ERK1/2 participate in AngII-induced periostin expression, a key regulator of cardiac fibrosis, by regulating the TGF-β1/Smad pathway. By disrupting the TGF-β pathway, AngII-induced periostin expression was attenuated. In cardiofibroblasts, ERK1/2 inhibition abolished AngII-induced TGF-β1 expression and Smad2/3 nuclear accumulation was stopped. This suggests a significant interaction between ERK1/2 and TGF-β1 signalling in AngII-induced periostin expression (Li, Fan et al. 2011). On the other hand, Rho-associated protein kinase (ROCK), a downstream mediator of RhoA GTPase (RhoA), constitutes a serine/threonine kinase that has been demonstrated to exert a vital role in several cardiovascular diseases. By inhibition of ROCK with fasudil, the TGF-β-TAK1 (TGF-β activated kinase 1) pathway was significantly downregulated after TAC and myocardial infarction (MI). Although this did not avoid the development of cardiac hypertrophy, it prevented cardiac fibrosis being associated by reduced mRNA expression levels of *type I collagen*, *type III collagen (Col1/3)* and *tissue inhibitor of metallopeptidase 1* (*Timp-1)* as critical mediators of fibrogenesis (Li, Xu et al. 2012). Additionally, upregulation of the RhoA/ROCK pathway is significantly correlated with cardiac hypertrophy-related calcium (Ca^{2+}) dysregulation; thus following ROCK inhibition, contractile abnormalities improve due to impaired Ca^{2+}-handling (Olgar, Celen et al. 2017).

Furthermore, TGF-β is critically involved in the fine orchestrated regulation of matrix metalloproteinases (MMPs), depending on the differing stimuli leading to their expression (Philips, Keller et al. 2004). MMPs constitute a family of 25 proteolytic enzymes that regulate ECM turnover and inflammatory signalling to adjust the inflammatory and fibrotic components of the wound healing response to cardiac injury. Besides, MMPs serve as upstream signalling initiators with direct actions on cell signalling cascades, thus representing key enzymes in left ventricular remodelling (Lindsey, Iyer et al. 2016). In *MMP-9*$^{-/-}$ mice, it has been demonstrated that age-related left ventricular diastolic dysfunction and collagen accumulation are attenuated. MMP-9 overexpression in mouse macrophages increased age-dependent myocyte

hypertrophy and vessel rarefaction. Thereby, angiogenesis-related factors e.g. intercellular adhesion molecule 1 (ICAM-1), integrins α3 and β3, platelet/endothelial cell adhesion molecule-1 and thrombospondin-1 were reduced indicating that MMP-9 enhances ageing-induced left ventricular inflammation and fibrosis (Toba, Cannon et al. 2017).

Moreover, both physiologic and pathologic cardiac hypertrophy are associated with elevation of cardiomyocyte Ca^{2+} levels. There are various Ca^{2+}-dependent signalling pathways, including calcineurin/nuclear factor of activated T cells (NFAT) signalling and calmodulin-dependent kinase II signalling (CaMKII). Catecholamines like norepinephrine and AngII bind as neurohumoral mediators to seven-transmembrane receptors being coupled to G proteins. Gq signalling activates phospholipase C, thus inducing intracellular Ca^{2+} release and activation of calcineurin/NFAT signalling. Recently, transient receptor potential cation (TRPC) channels were reported to be involved in activation of calcineurin/NFAT signalling as mice lacking TRPC1 are protected from the deleterious effects of volume overload and show preserved cardiac function accompanied by attenuated cardiac hypertrophy (Seth, Zhang et al. 2009, Shimizu and Minamino 2016). CaMKII is a serine/threonine kinase that is, inter alia, regulated by the Ca^{2+}/calmodulin complex, catecholamines and AngII. CaMKII phosphorylates the ryanodine receptor RyR2, causing sarcoplasmic reticulum leak of Ca^{2+} with resultant heart failure as shown by Ling and colleagues. After long-term pressure overload, CaMKII is likely critically involved in cardiac decompensation, since CaMKII knockout mice exhibited diminished left ventricular dilation, cardiac dysfunction and fibrosis. Moreover, these mice presented improved survival demonstrating its critical role in the development of heart failure independent of cardiac hypertrophy (Ling, Zhang et al. 2009, Haque and Wang 2017).

Summing up, maladaptive cardiac remodelling is driven by a multiplicity of signalling pathways. However, since some patients are refractory to the beneficial effects of medicamentous guideline-therapy like angiotensin-converting enzyme inhibitors and angiotensin receptor blockers, β-blockers and Ca^{2+} channel blockers, additional targets and agents are required representing a focus of cardiovascular research. Since cardiac disease still progresses even in responsive patients, the overall efficacy of these agents is to some extent limited (van Berlo, Maillet et al. 2013).

4.4 The ubiquitin-proteasome system

In mammalian cells, the ubiquitin (Ub)-proteasome pathway is responsible for most of the protein degradation and thereby for protein homeostasis by for example decomposing misfolded proteins as well as the bulk of cellular proteins (Collins and Goldberg 2017). This is the reason why the ubiquitin-proteasome system (UPS) as a selective proteolytic system and

degradation machinery constitutes a precisely orchestrated process. Hence, it plays a fundamental role in the regulation of the cell cycle and cell survival, signal transduction and transcriptional regulation. Central to the UPS is the conjugation of Ub to a target substrate and thereby its recognition by the 26S proteasome which is mediated by a cascade of 3 enzyme classes namely the ubiquitin-activating enzyme (E1), the ubiquitin-transferring enzyme (E2) and the ubiquitin ligase (E3) (Ciechanover 2015). Firstly, E1 activates the c-terminal glycine residue of ubiquitin, a highly conserved 76-amino-acid protein, under usage of ATP and forms a ubiquitin adenylate by binding Ub to one of its cysteine residues via a thioester bond. Next, the activated ubiquitin is transferred to an active site cysteine residue of E2 through another thioester bond. In the third step catalysed by E3, ubiquitin is linked by its C-terminal glycine in an amide isopeptide bond to the lysine residues of the substrates. Thus, the ubiquitin ligases play a central role in determining the selectivity of ubiquitin-mediated protein degradation and can be divided into four major classes depending on their ubiquitination domains: the HECT (homologous to E6-AP COOH terminus) proteins, the U-box domain proteins, the RING (really interesting new gene) finger proteins and a very unique group of E3s. The last group does not show any homology to other known E3s (Hershko and Ciechanover 1998, Kwon and Ciechanover 2017).

For the HECT domain E3s, ubiquitin is transferred once again from the E2 enzyme to an active site cysteine residue on E3, to generate a third high-energy thiol ester intermediate before its transfer to the ligase-bound substrate. This means that a simultaneous bound of the activated Ub and the substrate is intermediately created (Glickman and Ciechanover 2002).

In contrast, the second type of E3s has the U-box domain whose tertiary structure resembles the ones of RING-finger domain E3 ligases. Interestingly, some of the U-box E3s (e.g. Ufd2) can promote a polyubiquitin chain, provisionally termed as “E4” activity, in the presence of E3 (Tanaka, Suzuki et al. 2004). Thus, this protein binds to Ub of preformed conjugates and catalyzes the ubiquitin chain assembly in conjunction with E1, E2, and E3 (Koegl, Hoppe et al. 1999).

The major group of E3s, specified by over 600 human genes, is named RING-type E3, which is a general term for ubiquitin ligases with a RING-finger motif consisting of a cysteine-rich consensus sequence flanked by one or two histidine residues. This motif is capable of binding zinc and is subcategorized into typical and atypical forms. The RING domain is capable of binding to an E2 close to a ubiquitin thioester and thus activates the discharge of its ubiquitin cargo catalyzing a direct transfer of the activated ubiquitin to the E3-bound substrate. Alongside, a substrate can be either monoubiquitinated or a polyubiquitin chain can be synthesized (Tanaka, Suzuki et al. 2004, Deshaies and Joazeiro 2009). The fate of proteins tagged with a monoubiquitinated or a polyubiquitinated chain differs from each other. While

monoubiquitination, named non-canonical, is often a signal for receptor internalization and endocytosis, the process of polyubiquitination, also called canonical, leads mainly to degradation of the tagged protein by the 26S proteasome (Kravtsova-Ivantsiv and Ciechanover 2012, McDowell and Philpott 2013).

The last group of E3 ligases does not resemble the other classes and has no prespecified molecular structures in common like ligase UCH-L1, which is an abundant neuronal enzyme. This protein exhibits a second, dimerization independent, ubiquityl ligase activity in combination with a hydrolyse activity. Concluding, this activity profile is inconsistent with the one gene-one-enzyme paradigm (Liu, Fallon et al. 2002).

The targeted, polyubiquitinated substrates are afterwards degraded by the 26S proteasome. This protein is a large, multicatalytic protease composed of two subunits: a 20S core particle that carries the catalytic activity capped at the top and the bottom by 19S regulatory particles, which are responsible for the recognition of a substrate which carries the requisite number and configuration of ubiquitin. In this way, this process guarantees a tightly controlled and highly specific recognition, targeting and degradation of proteins regulating almost all cellular processes (Chen, Wu et al. 2016).

4.5 The Cullin-RING E3 ubiquitin ligase 7 complex as part of the ubiquitin-proteasome system

Of the cellular E3 ubiquitin ligases, the Cullin-RING finger multisubunit complexes are the largest family constituting a group of scaffolding proteins that associate with RING proteins and ubiquitin E3 ligases thereby mediating substrate-receptor bindings. These complexes are characterized by two signature components: a cullin (CUL) family molecule, containing a domain capable of assimilating a molecule with substrate-targeting function, and a c-terminally conserved cullin domain for its RING finger partner ROC1 (Regulator of cullins-1, also termed Rbx1 or Hrt1) for tethering an E2 Ub conjugating enzyme. Up to now, there are 8 cullin proteins that have been identified in mammals: CUL1, CUL2, CUL3, CUL4A, CUL4B, CUL5, CUL7/p53-associated parkin-like cytoplasmic protein and CUL9 (Li, Liu et al. 2017). Each of these proteins contains a conserved cullin homology domain that binds to RING box proteins (Sarikas, Hartmann et al. 2011, Chen and Yao 2016).

Cullin7 (also known as p185, p193 or KIAA0076) is the seventh member of the cullin protein family and thereof the second largest cullin (Skaar, Florens et al. 2007). Firstly, it was detected and isolated in coimmunoprecipitates with T antigen, and had up to that point, unknown additional functions mediated by transformation by simian virus 40 large T antigen (SV40 LT)

(Kohrman and Imperiale 1992). It was found that Cullin7 assembles an SCF-like E3 ligase complex (Skp, Cullin, F-box containing complex) composed of the adapter protein Skp1 (S-phase kinase-associated protein 1), ROC1 and the WD40 repeat-containing F-box protein Fbxw8 (also named Fbx29 or Fbw6) (**Fig. 3**). Hence, ROC1 recruits an Ub-charged E2 Ub-conjugating enzyme for substrate ubiquitination, whereas Fbxw8 is responsible for substrate protein recognition. Up to know, Fbxw8 is the only F-box protein known to bind to CUL7 just in interaction with Skp1, underlining its notable selectivity in marked contrast to CUL1, which can bind Skp1 alone without interaction with Fbxw8 (Dias, Dolios et al. 2002, Sarikas, Xu et al. 2008).

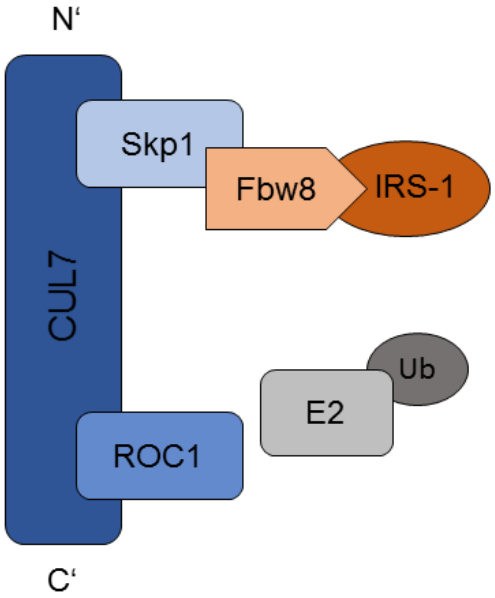

Figure 3: Composition of the Cullin-RING E3 ubiquitin ligase 7 (CRL7) complex. The CUL7 protein is capable of both integrating the ring finger protein ROC1 for attaching the E2 subunit charged with ubiquitin and the target-recognition subunit Skp1-Fbxw8 recognizing the substrate such as IRS-1. Adopted from Xu, Sarikas et al. 2008.

Besides Fbxw8, Cullin7 reportedly binds to glomulin (FAP68), a protein which is linked to inherited glomuvenous malformations in humans. The inactivation of two components (Cul7 and FAP68) contributes to vascular defects in mice. In addition, *Cul7*$^{-/-}$ embryos die immediately after birth due to respiratory distress. Moreover, their placentas show abnormal vascular structures with growth diminution, suggesting an imbalanced feto-maternal blood flow (Arai, Kasper et al. 2003). These data were further confirmed by Fahlbusch et al., demonstrating that Cullin7 and Fbxw8 expression in trophoblastic cells is regulated via oxygen tension by the trophoblast turnover being affected during intrauterine growth retardation (Fahlbusch, Dawood et al. 2012). Strikingly, the nonsense and missense mutations R1445X and H1464P of CUL7 in mammals, in each case, render CUL7 unable to recruit ROC1 leading

to 3M-syndrome in humans. This autosomal recessive inherited disease is also associated with pre- and postnatal growth retardation, facial dysmorphism characterized by a triangular face with a long philtrum, and skeletal abnormalities like tall vertebral bodies but, however, with normal intelligence (Huber, Dias-Santagata et al. 2005, Hasegawa, Tanaka et al. 2016). Similarly, it has also been shown that *Fbxw8*$^{-/-}$ embryos and placentas are smaller than the ones of wildtype and heterozygous littermates, so that only approximately 30 % of the expected litters survived birth. These mice displayed likewise growth retardation throughout postnatal development underling the significance of CRL7 in fetal growth control (Tsutsumi, Kuwabara et al. 2008).

Moreover, it has been demonstrated that TBC1D (Tre-2/Bub2/Cdc16 domain family, member 1) is an oncoprotein which activates growth factor-mediated signalling pathways promoting cellular proliferation and survival. TBC1D is ubiquitinated by CRL7 in response to growth factor stimulation leading to its degradation by the 26S proteasome. In human cancers, for example breast cancer, this growth-factor-driven negative feedback loop could be disrupted resulting in aberrant TBC1D expression and thus promotion of oncogenesis, underlining the role of the CUL7/Fbxw8 complex interacting as a tumour suppressor (Kong, Samovski et al. 2012, Kong, Lange et al. 2013). In addition, it has been shown that CUL7 may function as a tumour suppressor in interplay with T antigen, indicating its role in growth suppression. Wildtype and mutants of SV40 LT having a CUL7-binding deficiency show an increased ability to promote cell growth of mouse embryonic fibroblasts (MEFs) to high density (Kasper, Kuwabara et al. 2005). However, these results are contrasted with the findings of Hartmann et al., which showed that the binding of SV40 LT to CUL7 impairs the ability of CRL7 to mediate ubiquitin-dependent degradation of IRS-1, thereby leading to deregulation of IRS-1 downstream signalling pathways AKT and ERK/MAPK. Thus, unrestricted cell growth and oncogenesis are promoted by sustaining high promitogenic effector pathways (Hartmann, Xu et al. 2014). Interestingly, SV40 LT is not the only virus known to interact with Cullin7. Recently it has been shown that Cul7, alongside with cytoskeleton protein obscuring-like1 (Obsl1), interacts with the coiloided coil domain containing protein 8 (CCDC8), a membrane-associated host protein of Human Immunodeficiency Virus type 1 (HIV-1). This interplay leads to endocytosis, polyubiquitination and subsequent degradation of Gag, representing one of the major protein structures of HIV-1, assuming that a new pathway has been found for the containment of viral replication after HIV infection (Wei, Zhao et al. 2015).

Furthermore, the CUL7/Fbxw8-mediated degradation of MORF4 family-associated protein 1 (MRFAP1) has been demonstrated. The latter is a cell cycle-regulated protein leading to growth retardation and mitotic cell death when it is forcedly expressed. MRFAP1 accumulates during the metaphase but disappears thoroughly in the anaphase due to CUL7/Fbxw8-mediated depletion and thus reappears during the telophase. These findings suggest that this

degradation pathway via the Cullin E3 ligase 7 might play a role in the progression of the normal cell cycle, in monitoring the anaphase-telophase transition and in preventing genomic instability (Li, Liu et al. 2017). Additionally, CRL7 seems to play an important role in the degradation of cyclin D1 which regulates G1 progression in cancer cells being present in various malignant neoplasms such as lymphoma. The depletion of Fbxw8 in vitro caused a significant accumulation of cyclin D1 leading to a severe reduction of cell proliferation since the rapid turnover of cyclin D1 is needed for cell proliferation. This shows that ERK/MAPK-mediated cyclin D1 degradation through Fbxw8 is required for the malignant proliferation of cancer cells (Malumbres and Barbacid 2001, Okabe, Lee et al. 2006). Another example illustrating the impact of Cul7 is the amplicon of the 6p21.1 locus, which is a characteristic genomic alteration in metabolic syndrome-related hepatocellular carcinoma leading to overexpression of Cul7. Unexpectedly, the amplification of the 6p21.1 region was found predominantly in cases of advanced fibrosis and cirrhosis, whereas non-fibrotic-related carcinomas seemed to be unaffected (Brunt 2013). To further delineate this relation, Cul7 was downregulated using siRNA transfection in hepatoma cell lines. This led to significant higher cyclin D1 expression by the promotion of its degradation through CUL7, decreased cell proliferation and increased apoptosis. Hence, in the case of liver carcinogenesis, the oncogenic role of CUL7 overexpression has been demonstrated (Paradis, Albuquerque et al. 2013). It was further shown that the knockdown of Cullin7 inhibits the migration and invasion capacity of liver cancer cells in vitro as well as their metastatic abilities in vivo. These findings are in line with the enhancement of epithelial-mesenchymal transformation (EMT) which is associated with cancer progression and reduced long-term survival (Zhang, Yang et al. 2016). Further underlining these results, it has been recently shown that exalted Cul7 expression levels, as well as high Rab-like protein 3 (Rabl3) expression in hepatic cancer, correlate with an advanced clinical stage and lymph node metastasis, depicting Cullin7 as a potential prognostic indicator in hepatocellular carcinoma (An, Liu et al. 2017). Moreover, the CUL7/Fbxw8 complex was identified as the Ub ligase that is responsible for proteasome-mediated HPK1 degradation (hematopoietic progenitor kinase 1), a kinase which is lost in over 95 % of pancreatic cancers. Therefore, the knockdown of Fbxw8 in pancreatic cancer cells repressed their proliferation, which is in part due to the restoration of HPK1 protein expression revealing the oncogenic function of the CUL7/Fbxw8 ubiquitin ligase (Wang, Chen et al. 2014). Moreover, the proliferation, migration and invasion of cancer cells were significantly enhanced when Cullin7 was overexpressed in human breast cancer as well as in lung cancer. This was mediated by downregulation of p53 expression conveyed through CRL7 degradation (Guo, Wu et al. 2014, Men, Wang et al. 2015). In addition, CUL7's antiapoptotic function by degrading p53 leads to avoidance of c-Myc-potentiated apoptosis (Kim, Shago et al. 2007). In epithelial ovarian cancer, *Cul7* mRNA expression levels have been shown to be significantly higher and

may serve as an indicator for poor prognosis, being correlated to FIGO stage and lymph node metastasis (Xi, Zeng et al. 2016).

Another target of CRL7 is IRS-1. IRS-1 is phosphorylated at multiple tyrosine residues upon receptor activation, and then recruits SH2 (Src homology 2)-containing adaptor proteins for the activation of downstream AKT (via PI3K) and RAS/MEK/ERK (via Grb2/SOS) pathways (Sarikas, Xu et al. 2008). Interestingly, embryonic fibroblasts of *Cul7*$^{-/-}$ mice were found to accumulate IRS-1 and exhibit increased activation of IRS-1's downstream AKT and MEK/ERK pathways but displayed poor cell growth and cells associated with oncogene-induced tumour senescence. Targeted degradation of IRS-1 by CRL7 seems to constitute a core component of the mTOR negative feedback loop. In fact, the ligase recognizes seryl-phosphorylated IRS-1 generated by mTOR/S6K and mediates its polyubiquitination. By this negative feedback loop, the activity of PI3K, whose aberrant activation is a crucial contributing factor to cancer initiation and progression, is thought to be restrained. Since it has been shown that increased AKT signalling and MAPK activation as downstream effectors of IRS-1 induce senescence (Kennedy, Morton et al. 2011), the accumulation of IRS-1 through inactivation of CUL7 may launch this antiproliferative program (Xu, Sarikas et al. 2008). On this occasion, Scheufele and colleagues further provide both in vitro and in vivo evidence for a regulatory role of CRL7 as an upstream mediator of IRS-1 in the control of glucose homeostasis and insulin signalling. Their findings demonstrate that *Cul7*$^{-/-}$ mouse embryonic fibroblasts display an increase of AKT and ERK activation through phosphorylation upon insulin stimulation. In addition, the function loss of CRL7 in C2C12 myotubes and heterozygous knockout mice for either Cul7 or Fbxw8 resulted in enhanced glucose uptake and insulin-induced plasma glucose clearance, respectively, and displayed enhanced activation of IRS-1 downstream signalling pathways upon insulin stimulation. Taken together, CRL7 plays a pivotal role for the regulation of insulin and IGF signalling by targeting the central hub of the signalling cascade, namely IRS-1, for ubiquitination and thus its degradation (Scheufele, Wolf et al. 2014).

Summing up, these studies provide paradoxical evidence for CUL7 having two apparently opposing activities, namely as a tumour suppressor or an oncogene. These convertible properties are most likely attributable to a context-dependent function and manner and show the various interactions of CUL7 with its environmental molecules and proteins.

4.6 The role of Cullin-RING E3 ubiquitin ligase 7 in the heart

It has been demonstrated in cardiomyocytes derived from differentiating embryonic stem cells that the co-expression of mutant p53 and mutant Cul7 blocks E1A-induced (Adenovirus early Region E1A Protein*)* apoptosis, rendering the cells responsive to the growth-promoting

influence of the E1A viral oncoproteins (Pasumarthi, Tsai et al. 2001). Furthermore, effects of permanent coronary artery occlusion in mice expressing a dominant-interfering mutant of Cul7 (MHC-1152stop mice) in the heart have been investigated. Interestingly, within 4 weeks, cardiomyocyte DNA synthesis occurred in the regions of the interventricular septum as well as the infarct border zone. Concomitant to this cardiac cell cycle activation, the cell loss-induced hypertrophic compensatory cardiomyocyte growth was greatly reduced (Nakajima, Nakajima et al. 2004). Apart from increased DNA synthesis, cardiac function was enhanced in the transgenic mice 4 weeks post MI when compared to the non-transgenic siblings. During the acute phase of infarction, the MHC-1152stop mice and their non-transgenic littermates showed no difference in scar size expansion indicating that transgene expression was initially not cardio-protective unlike in the chronic phase of infarction. Here smaller infarcted areas became apparent probably due to an increased number of cardiomyocytes rather than reduced apoptotic rates. In fact, the number of apoptotic cardiomyocytes was surprisingly not different in mice expressing the wildtype or mutated Cullin7 (Hassink, Nakajima et al. 2009).

4.7 Aims and objective of this thesis

Based on the influence of the Cullin-RING E3 ligase 7 complex on pivotal signalling pathways in the heart, this thesis investigates whether Cul7 contributes to the regulation of myocardial remodelling and delineates underlying molecular pathomechanisms.

Therefore, a cardiomyocyte-specific knockout of CUL7 was generated using the Cre/loxP strategy. For this purpose, a transgene mouse model was created, and knockout was achieved by the intrapericardial application of AAV9, encoding a Cre recombinase under a CMV-promotor (AAV9-CMV-iCre). As controls, mice injected either with Ringer's lactate solution or AAV9-CMV-dsRed were examined. In a first instance, depletion levels of *Cul7* mRNA were evaluated in the whole heart as well as in the cardiomyocyte and cardiofibroblast cell fractions by real-time PCR and consequently, protein levels of CUL7 were assessed in isolated cardiomyocytes via immunoblotting. Afterwards, the global gene transfer of AAV9 to non-cardiac tissue such as spleen, liver and kidney was assessed by Western blot.

Subsequently, the effects of Cul7 ablation were investigated under basal conditions as well as under conditions of increased afterload attained by transverse aortic constriction surgery, inducing cardiac overload and fibrosis. For both conditions, heart weight/body weight-, heart weight/tibia length- and heart weight/lung weight-ratios were validated for cardiac phenotypisation. The heart function and left ventricular dimensions were assessed by echocardiography. To measure left ventricular fibrosis, Sirius Red/ Fast Green staining was

performed. For evaluation of cardiac hypertrophy, cardiac sections were stained with wheat germ agglutinin (WGA).

To further delineate underlying molecular mechanisms of the observed phenotype, the abundance of CRL7-regulated proteolytic target proteins like AKT, ERK and IRS-1 was investigated by immunoblot in cardiomyocyte lysates. In addition, real-time PCR analysis of fibrotic modulators such as *Tgf-β*, *Ccn1* or *Timp-1* was performed. Moreover, rates of apoptotic cardiomyocytes in the diseased heart were calculated via Terminal deoxynucleotidyl transferase dUTP nick end labelling (TUNEL) analysis.

Finally, to exclude viral side effects, C57BL/6 wildtype mice were also injected with Ringer's lactate solution and both types of AAV9 and underwent 3 weeks of increment of afterload. For validation of surgery, heart weight/body weight-, heart weight/tibia length- and heart weight/lung weight-ratios were assessed. Conclusively, heart sections were submitted to TUNEL staining, assessing cardiac apoptosis.

5 MATERIALS

5.1 Chemicals and reagents

In this work, protected trade and brand names are not indicated.

Name	Company
Acetic acid glacial	Roth (Karlsruhe, Germany)
Acrylamide / Bis solution 30%	Bio-Rad Laboratories GmbH (Munich, Germany)
Agarose	Roth (Karlsruhe, Germany)
Ampicillin	Roth (Karlsruhe, Germany)
Ammonium persulfate (APS)	Sigma-Aldrich (Taufkirchen, Germany)
Antipain	Sigma-Aldrich (Taufkirchen, Germany)
Bovines Serum Albumin (BSA) fraction V	AppliChem (Darmstadt, Germany)
Protein Assay Dye Reagent Concentrate	Bio-Rad Laboratories GmbH (Munich, Germany)
Bromophenol blue	Roth (Karlsruhe, Germany)
2,3-Butanedione monoxime (BDM)	Sigma-Aldrich (Taufkirchen, Germany)
Chloroform (Trichloromethane, $CHCl_3$)	Roth (Karlsruhe, Germany)
Phenol / chloroform / isoamyl alcohol	Roth (Karlsruhe, Germany)
Citric acid	Roth (Karlsruhe, Germany)
Desoxynucleosidtriphosphate (dNTP)	Roth (Karlsruhe, Germany)
Deoxy-thymine nucleotide (oligo(dT))	Thermo Fisher Scientific (Surrey, United Kingdom)
Dipotassium hydrogen phosphate	Roth (Karlsruhe, Germany)
Direct Red 80	Sigma-Aldrich (Taufkirchen, Germany)
Dithiothreitol (DTT)	Roth (Karlsruhe, Germany)
D-(+)-Glucose	Sigma-Aldrich (Taufkirchen, Germany)
DPBS	GIBCO (Karlsruhe, Germany)
Eosin Y Solution Aqueous	Sigma-Aldrich (Taufkirchen, Germany)
Ethylenediaminetetraacetic acid (EDTA)	Roth (Karlsruhe, Germany)
Ethanol	Roth (Karlsruhe, Germany)
Ethidium bromide solution (1%)	Roth (Karlsruhe, Germany)
Fast Green FCF	Sigma-Aldrich (Taufkirchen, Germany)

FastStart Universal SYBR Green Master (Rox)	Roche (Mannheim, Germany)
Fetal bovine serum (FBS)	PAN (Aidenbach, Germany)
Fetal calf serum (FCS)	PAN (Aidenbach, Germany)
Glycerol	Merck (Darmstadt, Germany)
Glycine	Roth (Karlsruhe, Germany)
Hematoxylin 2	Thermo Fisher Scientific (Surrey, United Kingdom)
Heparin-natrium 25000 I.U.	Ratiopharm (Ulm, Germany)
HEPES	AppliChem (Darmstadt, Germany)
Hydrochloric acid	Roth (Karlsruhe, Germany)
Iodixanol	Progen Biotechnik (Heidelberg, Germany)
Isopropanol	Roth (Karlsruhe, Germany)
Isoflurane	Abbott (Wiesbaden, Germany)
Lactated Ringer's solution	B. Braun Medical AG (Sempach, Swiss)
Laminin	BD Biosciences (Heidelberg, Germany)
Leupeptin	Sigma-Aldrich (Taufkirchen, Germany)
Magnesium sulfate ($MgSO_4$)	Sigma-Aldrich (Taufkirchen, Germany)
Methanol	Roth (Karlsruhe, Germany)
2-Mercaptoethanol	AppliChem (Darmstadt, Germany)
Minimum Essential Eagle (MEM)	GIBCO (Karlsruhe, Germany)
Monopotassium phosphate (KH_2PO_4)	Sigma-Aldrich (Taufkirchen, Germany)
Mounting medium for fluorescence with DAPI	Vector Laboratories (Burlingame, USA)
Murine RNase inhibitor	New England Biolabs (Frankfurt am Main, Germany)
Opti-MEM I	GIBCO (Karlsruhe, Germany)
Paraformaldehyde (PFA)	Sigma-Aldrich (Taufkirchen, Germany)
Penicillin/Streptomycin	GIBCO (Karlsruhe, Germany)
peqGOLD RNAPure	Peqlab (Erlangen, Germany)
Phenylarsine oxide (PAO)	Sigma-Aldrich (Taufkirchen, Germany)
Phenylmethanesulfonyl fluoride (PMSF)	Sigma-Aldrich (Taufkirchen, Germany)
Piric acid saturated solution	Roth (Karlsruhe, Germany)
Polyethyleneimine (PEI)	Sigma-Aldrich (Taufkirchen, Germany)
Potassium chloride (KCl)	AppliChem (Darmstadt, Germany)
Potassium dihydrogen orthophosphate	Roth (Karlsruhe, Germany)

RNase Zap	Applied Biosystems (Darmstadt, Germany)
Sodium chloride	Roth (Karlsruhe, Germany)
Sodiumdodecylsulfate (SDS)	Roth (Karlsruhe, Germany)
Sodium fluoride (NaF)	Sigma-Aldrich (Taufkirchen, Germany)
Sodium hydrogen phosphate dibasic (Na_2HPO_4)	Roth (Karlsruhe, Germany)
Sodium hydroxide (NaOH)	Roth (Karlsruhe, Germany)
Sodium orthovanadate (Na_3VO_4)	Sigma-Aldrich (Taufkirchen, Germany)
Taurine	Sigma-Aldrich (Taufkirchen, Germany)
Tris base	Roth (Karlsruhe, Germany)
Tetramethylethylenediamine (TEMED)	Roth (Karlsruhe, Germany)
Tri-sodium-citrate (dihydrate)	AppliChem (Darmstadt, Germany)
Triton-X-100	Sigma-Aldrich (Taufkirchen, Germany)
Tryptone-Peptone	Roth (Karlsruhe, Germany)
Toluene	Roth (Karlsruhe, Germany)
Tween 20	Roth (Karlsruhe, Germany)
Phenol Red	Sigma-Aldrich (Taufkirchen, Germany)
Xylene	Roth (Karlsruhe, Germany)
Yeast extract	Roth (Karlsruhe, Germany)

Table 1: Chemicals and reagents. Sorted alphabetically.

5.2 Oligonucleotides

Genotyping

Following primers for genotyping of the $Cul7^{flox}$; Myh6-$^{CreTg(1)/0}$ - mouse strain ($Cul7^{flox}$:(Arai, Kasper et al. 2003); Myh6- $^{CreTg(1)/0}$: (Sohal, Nghiem et al. 2001)) were purchased at Sigma-Aldrich (Taufkirchen). Stock solutions of 100 pmol / µl were prepared in ddH_2O according to the manufacturer's advice and stored at - 20°C. Working solutions of 10 pmol / µl were used.

Name	**Sequence (5'→3')**
Cre800	GCTGCCACGACCAAGTGACAGCAATG
Cre1200	GTAGTTATTCGGATCATCAGCTACAC
GABRA1F	AACACACACTGGAGGACTGGCTAGG
GABRA1R	CAATGGTAGGCTCACTCTGGGAGATGATA
SC1	CGAAAGCAGCAACAGCTGTTATTCTGGGTG

SC2	AGACCGCATCCCCCTCCGACACAGTTCTGG

Table 2: Characteristics of primers used for genotyping purposes. Sorted alphabetically.

Real-time reverse transcription-PCR

In this work, all oligonucleotides used for real-time reverse transcription-PCR (qRT-PCR) were ordered at Eurofins MWG Biotech (Ebersberg). The stock solutions of 100 pmol / µl were prepared in ddH_2O according to the manufacturer's protocol and stored at - 20 °C. For all experiments, working solutions of 20 pmol / µl were utilised.

Name	Forward (5'→3') sequence	Reverse (5'→3') sequence
CCN1	ACCTCCTTGGATTCGATGCCT	TGCCAAAGACAGGAAGCCTCT
CCN2	CGCCAAGCAGCTGGGAGAAC	GGCGATTTTAGGTGTCCGGA
Cullin7	CGGAATGGCTGTGCTGATG	GCCTTGGATCCTCTGGTCAA
MMP2	CGGAGATCTGCAAACAGGACA	CGCCAAATAAACCGGTCCTT
MMP3	TGTCCCGTTTCCATCTCTCTC	TGGTGATGTCTCAGGTTCCAG
MMP9	GCGTGTCTGGAGATTCGACTT	TATCCACGCGAATGACGCT
PDGF- AA	TGGCTCGAAGTCAGATCCACA	AGCCCCTACGGAGTCTATCTC
Rpl32	GCCAAGATCGTCAAAAAGA	GTCAATGCCTCTGGGTTT
dsAAVqS V40 rw2 *	GCGACTCTAGATCATAATCAGCC	GCTGCAATAAACAAGTTAACAACAAC A
TGF-β	CTCCCGTGGCTTCTAGTGC	GCCTTAGTTTGGACAGGATCTG
TIMP-1	CTATCCCTTGCAAACTGGAGA	ACCTGATCCGTCCACAAACA

Table 3: Characteristics of primers used for real-time reverse transcription-PCR. If not indicated otherwise the qPCR primers target mouse cDNA. Sorted alphabetically.

(*: for AAV titration)

5.3 Antibodies

Characteristics of first antibodies

Name	Target species	Host	Dilution	Manufacturer
AKT	mouse	rabbit	1:1000	Cell Signalling
CUL7 (Ab38)	mouse	mouse	1:5000	Sigma Aldrich
Heat shock protein 90 (HSP90 α/β) (F-8)	mouse	mouse	1:10000	Santa Cruz Biotechnology

IRS-1	mouse	rabbit	1:1000	Millipore
p44/42 MAPK (ERK1/2) (L34F12)	mouse	mouse	1:1000	Cell Signalling
Phospho-AKT (Ser473)	mouse	rabbit	1:1000	Cell Signalling
Phospho-p44/42 MAPK (ERK1/2)(Thr202/Tyr204)	mouse	rabbit	1:1000	Cell Signalling

Table 4: Characteristics of first antibodies. Target species, host as well as antibody dilution for immunological detection are displayed. Sorted alphabetically**.**

Characteristics of secondary antibodies

Name	**Target species**	**Host**	**Dilution**	**Manufacturer**
Anti-mouse IgG, HRP-linked Ab	mouse	horse	1:10000	Cell Signalling
Anti-rabbit IgG, HRP-linked Ab	rabbit	goat	1:10000	Cell Signalling

Table 5: Characteristics of second antibodies. Target species, host as well as antibody dilution for immunological detection are displayed. Sorted alphabetically**.**

5.4 Enzymes

Name	**Company**
Benzonase	Merck (Darmstadt, Germany)
Collagenase Type 2	Worthington Biochemical Corporation (Lakewood, United States)
DNase	Sigma-Aldrich (Taufkirchen, Germany)
Proteinase K	AppliChem (Darmstadt, Germany)
Restriction endonucleases (AhdI, BamHI HF, ScaI HF, SmaI)	New England Biolabs (Frankfurt am Main, Germany)
Reverse transcriptase Protoscript II	New England Biolabs (Frankfurt am Main, Germany)
Taq DNA Polymerase	GenScript (Piscataway, USA)
Trypsin	GIBCO (Darmstadt, Germany)

Table 6: Overview of used enzymes. Protected trade and brand names are not indicated**.** Sorted alphabetically**.**

5.5 Buffers and solutions

Common media, buffers and solutions

AAV-lysis buffer

50 mM Tris / Cl	3.03 g
150 mM NaCl	4.38 g
ddH_2O	ad 500 ml
adjust pH with HCl to pH 8.5	

Lysogeny broth (LB-) medium

Peptone-Tryptone	10 g
Yeast extract	5 g
NaCl	5 g
1 M NaOH	1 ml
ddH_2O	ad 1 l

Phosphate buffered saline (PBS; 10x)

NaCl	80 g
KCl	2 g
Na_2HPO_4 x $7H_2O$	11.5 g
KH_2PO_4	2 g
ddH_2O	ad 1 l

PBST

PBS (10x)	100 ml
Tween 20	0.5 ml
ddH_2O	ad 1 l

Terrific broth (TB-) medium

Basis of buffer	
Bactotryptone	60 g
Yeast extract	120 g
Glycerol	20 ml
ddH_2O	ad 4.5 l
Phosphate buffer	
Potassium dihydrogen orthophosphate	11.56 g

Dipotassium hydrogen phosphate	62. 7 g
ddH_2O	ad 500 ml
add 100 ml of phosphate buffer to 900 ml of basis buffer	

Tris-acetate-EDTA (TAE) buffer (50x)

Tris	0.2 M
Acetic acid	5.7 %
0.5 M EDTA	10 %
ddH_2O	ad 1 l

Buffers for DNA methods

DNA loading buffer (5x)

0.5 M EDTA pH 8.0	1.4 ml
Glycerol	3.6 ml
Bromophenol blue	0.01g
ddH_2O	7 ml

Phenol-/Chloroform-Lysis buffer for tailtip digestion

Tris	12.1 g
EDTA	1.87 g
NaCl	11.7 g
ddH_2O	ad 1 l

Buffers for RNA methods

5x Protoscript II reaction buffer

Buffers for protein methods

Protein Assay Dye Reagent Concentrate (5x)

1:5 dilution of Bradford solution

LAEMMLI loading buffer (4x)

1 M Tris/Cl pH 6.8	1.5 ml
1 M DTT	3 ml
SDS powder	0.6 g
Bromophenol blue	0.03 g
Glycerol	3.25 ml (prewarmed)
ddH_2O	ad 7.5 ml

Lower gel buffer (4x)

Tris/Cl	182 g
SDS 10%	40 ml
ddH_2O	ad 1 l
adjust pH with HCl to pH 8.8	

Protein lysis buffer „cell signalling“

Tris/Cl pH 7.5	20 mM
NaCl	150 mM
EDTA	1 mM
EGTA	1 mM
Triton-X-100	1 % vol.
Sodium pyrophosphate	2.5 mM
Na_3VO_4	1 mM
Per 10 ml: 1 tablet Complete Mini	

Transfer buffer (10x)

1M Tris/Cl pH 8.3	225 ml
Glycine	101.34 g
ddH_2O	ad 900 ml

Transfer buffer (1x)

1M Tris/Cl pH 8.3	25 ml
Glycine	11.26 g
Methanol	100 ml
ddH_2O	ad 1 l

Tris-Glycine SDS buffer (10x; running buffer)

Tris/Cl	30 g
Glycine	144 g
SDS	15 g
ddH_2O	ad 1 l

Stripping buffer

Glycine	15 g
SDS	1 g
ddH_2O	ad 1 l
adjust pH with HCl to pH 2.0	

Upper gel buffer (4x)

Tris/Cl	61 g
SDS 10%	40 ml
ddH_2O	ad 1 l
adjust pH with HCl to pH 6.7	

Buffers for histological and immunohistochemical stainings

Eosin Solution (0.1 %)

Eosin Y Solution aqueous	20 ml
ddH_2O	80 ml
Acetic acid glacial	1 drop

Fast Green (0.1 %)

FastGreen FCF	500 mg
ddH_2O	500 ml

PFA solution (4 %)

PFA	20 g
PBS (1x)	480 ml
Heat solution to 60 °C	
Adjust pH with 1 M NaOH to pH 7,2	
PBS (1x)	ad 500 ml

Sirius Red (0.01 %)

Direct Red 80	50 mg
ddH_2O	15 ml
Piric acid-saturated solution 1.3 %	485 ml
before adding the piric acid-saturated solution, the solution must be filtered	

Tri-sodium-citrate (dihydrate) buffer

Tri-sodium-citrate (dihydrate)	2.94 g
ddH_2O	1 l
Tween 20	0.5 ml
adjust pH with HCl to pH 6.0 before the addition of Tween 20	

Adult mouse cell isolation media, buffer and solutions

AMCF medium 10 %

MEM	10.8 g
Vitamin B12	1 ml
$NaHCO_3$	350 mg
ddH_2O	ad 1 l

AMCM plating medium

MEM	45.5 ml
FCS	2.5 ml
500mM BDM	1 ml
Penicillin/Streptomycin	0.5 ml
200mM L-Glutamine	0.5 ml

AMCM culture medium

MEM	49 ml
BSA	2.5 ml
Penicillin/Streptomycin	0.5 ml
200mM L-Glutamine	0.5 ml

BrdU

BrdU	230 mg
ddH_2O	74.8 ml

Buffer P1

Perfusion buffer	9 ml
FCS	1 ml
10mM $CaCl_2$	12.5 µl

Buffer P2

Perfusion buffer	47.5 ml
FCS	2.5 ml
10mM $CaCl_2$	62.5 µl

Digestion buffer

Collagenase Typ 2	46 mg
100 mM $CaCl_2$	15 µl
Perfusion Buffer	20 ml

Perfusion buffer

490 ml Stock Buffer	490 ml
500 mM BDM	10 ml
5% Glucose	10 ml

Stock perfusion buffer

NaCl	6.6 g
KCl	0.35 g
KH_2PO_4	0.082 g
Na_2HPO_4	0.085 g
$MgSO_4$	0.3 g
$NaHCO_3$	1.01 g
$KHCO_3$	1.01 g
Taurine	3.75 g
Phenol Red	0.012 g
1 M HEPES buffer	10 ml

5.6 Used kits

Name	Company
In Situ Cell Death Detection Kit, TMR Red	Roche (Mannheim, Germany)
Pierce™ ECL 2 Western blotting Substrate	Thermo Scientific (Bonn, Germany)
Power SYBR Green PCR Master Mix	Roche (Mannheim, Germany)
PureLink® Plasmid Midi/Maxi Kit	Invitrogen (Karlsruhe, Germany)
PureLink HiPure Plasmid DNA Gigaprep Kit	Thermo Scientific (Bonn, Germany)

Table 7: Overview of used kits. Protected trade and brand names are not indicated. Sorted alphabetically**.**

6 METHODS

6.1 Animal work

6.1.1 Mouse model

All animal handling protocols have been approved by the Government of Bavaria and mice were kept species-appropriate in cages up to 3-4 mice (3 for male mice, 4 for female animals, respectively) with a cycle length of 12 hours for luminosity and darkness. Litters were separated at the age of 3.5 weeks, received an earmark as identification mark and a tail biopsy of 1 mm was taken for subsequent genotyping.

The mice carrying the floxed *Cullin7* allele were created and originally obtained by DeCaprio and colleagues in 2003 (Arai, Kasper et al. 2003). The Cre/loxP-system is a genetic tool enabling site-specific recombination events in genomic DNA. The Cre enzyme is a DNA recombinase which recognizes specific LoxP sequences, so that a recombination event and subsequent DNA modification occurs. In the used mouse strain, loxP-sites are inserted downstream and upstream intron 1 and 4, leading to loss of exon 2 to 4 in case of presence of the Cre protein, which was expressed by an AAV9 (**Fig. 4**). Within this study, only transgene male homozygous floxed C57BL/6 or rather C57BL/6 wildtype mice were used for animal experiments, except for evaluation of the deletion efficacy of Cullin7, where female animals were additionally implemented.

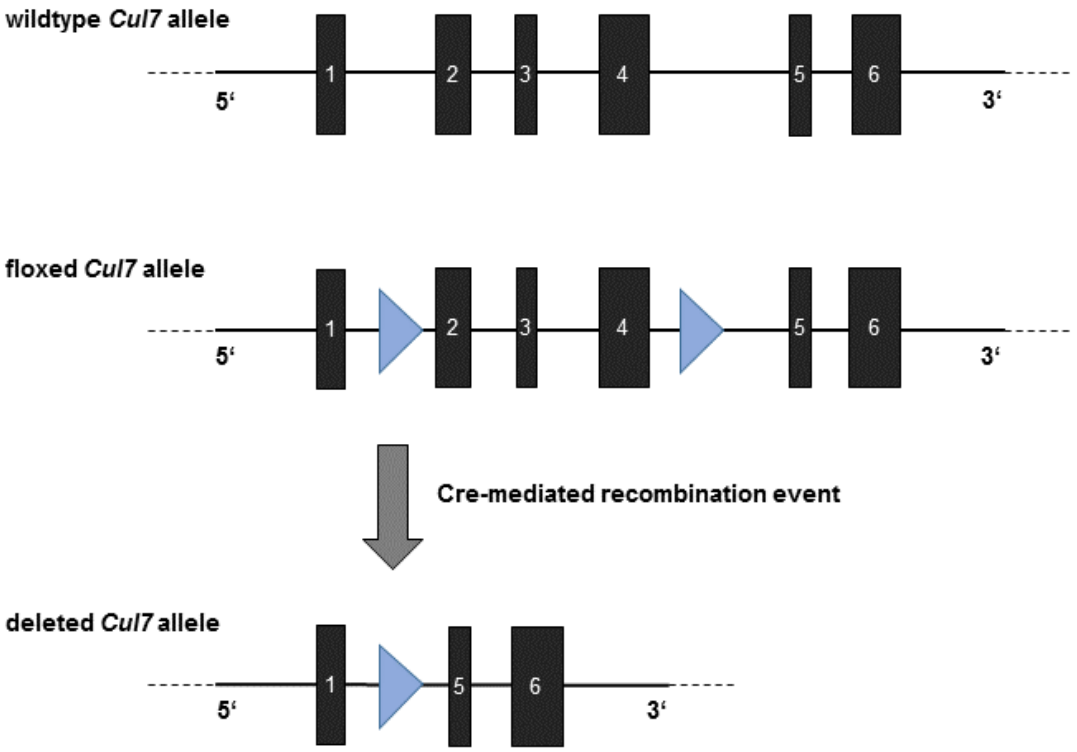

Figure 4: Cre/loxP-mediated deletion of Cul7. Scheme of *Cul7* wildtype (upper panel), floxed (middle panel) and deleted alleles (lower panel). Upon expression of the Cre recombinase by delivery of AAV9, exon 2 to 4 (black vertical boxes) are deleted by recognition of loxP sites (triangles in light blue, middle panel) and subsequently the recombination event takes place (lower panel). Horizontal black lines indicate introns.

6.1.2 Genotyping

To the mice' tailtips 500 µl of phenol/chloroform buffer and 2.5 µl Proteinase K were added in 1.5 ml tubes (Sarstedt AG & Co, Nürnbrecht, Germany) and subsequently incubated overnight gently shaking at 950 rounds per minute (rpm) and 56 °C in the Eppendorf "Thermomixer compact" (Eppendorf AG, Hamburg, Germany). Either the tailtips were used immediately or stored at - 20 °C before the start of digestion. After complete digestion of the tissue samples overnight, 500 µl phenol/chloroform/isoamyl alcohol were added and centrifuged at 14000 rpm at room temperature for 10 minutes in the Eppendorf centrifuge 5417R (Eppendorf AG, Hamburg, Germany). The upper, DNA-containing phase was transferred into a new 1.5 ml tube, 500 µl of isopropanol were added and mixed rigorously before centrifugation at 14000 rpm at 4 °C for 10 minutes. Carefully the supernatant was discarded and 500 µl ethanol 70 % were added and centrifuged similarly to the step before. Afterwards, again the supernatant was discharged, and the tubes were dried inverted on a cellulose tissue for approx. 20-30 minutes. Finally, the remaining DNA in the bottom of the tube was dissolved in 50 µl ddH_2O and stored at - 20 °C until usage and implementation of PCR for genotyping.

6.1.3 Transverse aortic constriction as cardiac disease model

Approximately 30 minutes prior to anaesthesia by inhalation with 4 % isoflurane / 96 % pure oxygen for transverse aortic constriction surgery, 9 week old male mice were analgised with the opioid buprenorphine and fixed on a 40 °C hot warming plate. After obtaining sufficient levels of anaesthesia, isoflurane concentration was reduced to 1-2 %. Thereafter, the thoracotomy was performed at the height of the second rib, discovering and preparing the aortic arch by removing surrounding adipose tissue. Then the aortic constriction was made between the left common carotid artery and the brachiocephalic artery by putting a 27 gauge cannula directly alongside the aorta and constricting the vessel with a 7-0 nylon thread and two knots until a complete derogation of the blood flow was achieved. Immediately the cannula was removed, whereby the diameter of the aorta was reduced to approx. 4 mm and then the thorax was closed again. The following 3 days, the analgesic treatment was performed by intraperitoneal injection of dipyrone 200 mg per kg body weight every 4-6 hours. Control animals were subjected to a similar operation which is termed sham with opening of the thorax and preparation of the aortic arch, but without aortic banding.

6.1.4 Cardiac monitoring

To assess cardiac function by the usage of the Vevo 770 ultrasonic machine (VisualSonics, Ontario, United States), the mice were anaesthetized with isoflurane 1 % per inhalationem, administered by a facial mask, and placed on a warming platform in the supine position. To take an electrocardiogram and to observe heart rate, the mice were in addition fixed on electrodes with electrode gel (Spectra 236 Parker, Medic, Germany) on the desk of the ultrasound stage. To guarantee precise evaluation of heart function, the chests of mice were shaved using a depilatory cream. Afterwards, the left ventricle of the heart and its long axis were focused in an angle of 30 ° using the Brightness-Mode (B-Mode) while the short axis was assessed in an angle of 90 ° in the Motion-Mode (M-Mode), recording contractility of the left ventricle. Via these measurements the parameters fractional shortening (FS), ejection fraction (EF), systolic and diastolic left ventricular internal diameter (LVID $_{d/s}$), and systolic and diastolic left ventricular volume (left ventricular volume $_{d/s}$) were calculated.

6.1.5 Intrapericardial delivery of viral vectors into neonates

Neonatal injection of Cul7$^{flox/flox}$ mice on day 4 to 5 after birth was performed intrapericardially with 5 x 10^{11} viral particles diluted in a volume of 50 µl lactated Ringer's solution via a 0.5 ml

BD Micro-Fine syringe for insulin injection in humans (Becton, Dickinson and Company, Franklin Lakes, United States). To hit exactly the pericardium and none of the other organs like liver or lungs, the sternum served as guidance, gleaming slightly white while holding the offspring gently and carefully in its neck. In this respect, the xiphoid process functioned as an orientation aid and the needle did not have to go further than 4-5 mm, otherwise the heart would be injured severely. After injection of the AAV9, the litter had to be returned to its mother very quickly, protecting it against cooling down and rejection.

6.2 DNA methods

6.2.1 Polymerase chain reaction

Polymerase chain reaction (PCR) was applied for amplification of DNA fragments for genotyping and set-up of homozygous breeding pairs of mice carrying the floxed alleles. Therefore, a specific part of the DNA defined by two different primers is amplified, and afterwards separated and analysed through an agarose gel cast. Since the floxed mice were originally crossed with animals expressing a Cre recombinase flanked by two mutated oestrogen receptors under the control of the myosin heavy chain alpha gene promoter Myh6, genotyping was always performed checking the floxed as well as the Cre-expressing allele. For this purpose, 2 different PCR-mastermixes were assembled on ice, which were composed as shown in the section below.

PCR-mastermix for the *Cul7* allele for one sample

Component	**Volume**
10x Taq buffer	2.5 µl
10 µM SC1	1.25 µl
10 µM SC2	1.25 µl
10 mM dNTPs	0.5 µl
Taq DNA polymerase	0.25 µl
ddH_2O	18.25 µl

PCR-mastermix for the *Myh6-Mer-Cre-Mer* transgene allele for one sample

Component	**Volume**
10x Taq buffer	2.5 µl
10 µM Cre 800	1.25 µl
10 µM Cre 1200	1.25 µl
10 µM GABRA 1F	1.25 µl
10 µM GABRA 1R	1.25 µl
10 mM dNTPs	0.5 µl
Taq DNA polymerase	0.25 µl
ddH_2O	15.25 µl

After assembly of the mastermixes with a total volume of 24 µl per sample in a 0.5 ml reaction tube, 1 µl of DNA was added, respectively. The amplification reactions of DNA-fragments for both alleles were carried out by T Gradient cycler (Biometra, Göttingen, Germany) with identical application settings for both attempts as follows.

PCR-program for genotyping purpose

Reaction step	**Temperature**	**Time**	**Cycles**
Pre-denaturation	94 °C	3 minutes	1
Denaturation	94 °C	30 seconds	37
Annealing	68 °C	1 minute	
Elongation	72 °C	1 minute	
Final elongation	72 °C	5 minutes	1

Table 8: PCR protocol for genotyping. The denaturation, annealing and elongation steps were repeated 37 times.

For confirmation of recombination events via PCR, primers SC1 and SC2, annealing in intron 1 and intron 5, were utilized for running the same PCR-program as described above. In the case of successful recombination and subsequent knockdown of Cul7, a 300 bps amplification product results. On these terms, an amplification of the unrecombined genome part is not possible. For internal control primers binding in intron 7 were used which are not influenced by viral delivery and recombination events. After amplification, all DNA samples were cooled down to 4 °C until usage.

6.2.2 Agarose gel electrophoresis

Preparation of agarose gels

For separating DNA fragments depending on their size, agarose gel electrophoresis was performed. In this regard, to obtain a 2 % agarose gel, 3 g agarose were mixed in 150 ml 1x TAE buffer in an Erlenmeyer flask (Fisherbrand, Surrey, United Kingdom) and boiled in a microwave (Panasonic, Kadoma, Japan) for 3 minutes at 800 watts until the powder was dissolved entirely. Afterwards, 30 µl ethidium bromide were added and distributed by smooth agitation of the flask. The suspension was then casted using Gel tray Mini M and gel comb 20 well spacer 1.0 mm (PeqLab, Erlangen, Germany) for approx. 30 minutes at room temperature.

Gel electrophoresis

The cured agarose gel was put inside the PeqLab gel electrophoresis system Mini M (PeqLab, Erlangen, Germany) with succeeding infill of the chamber with 1x TAE buffer according to the manufacturer's advice. DNA amplification products were mixed with 5 µl of 5x loading buffer. Next, 12.5 µl of the suspension were charged into the gel pockets after removal of the spacers. Additionally, a 100 bp DNA ladder (New England Biolabs, Frankfurt am Main, Germany) was loaded for identification of the size of the DNA fragments. Gel run was performed at 150 volt (V) and 400 milliampere (mA) for 25 minutes (electrophoresis power supply EPS-301, Healthcare Life Science Deloitte, Munich, Germany). Afterwards, visualization was carried out by UV transilluminator MD-25/HD-25 (Wealtec, Sparks, United States) and analysed with DeVisionG 2.0 software program (Decon Science Tec GmbH, Hohengandern, Germany).

6.3 RNA methods

6.3.1 RNA isolation from tissue and cell culture samples

Different tissue types such as heart or liver samples were shock-frozen in liquid nitrogen or else stored at - 80 °C until usage, before the RNA extraction procedure was started. For RNA extraction of cell culture dishes, cells were carefully washed with DPBS, dried to avoid thinner effects and subsequently either stored at - 80 °C or RNA preparation initiated immediately. Before the onset of RNA extraction, the whole working place was entirely cleaned with RNase Zap.

To begin with tissue samples, tissues were put in a 2 ml reaction tube and 1 ml of RNAPure reagent was added followed by homogenizing, using the ultra-turrax machine (IKA-Werke, Staufen im Breisgau, Germany) for tissue crushing. To avoid contaminations, the turrax was cleaned excessively first in water, then in 0.5 M NaOH, and again in water in between every time of use, removing all residual tissue particles of the preceding samples. Afterwards, the dispersion was incubated for 5 minutes at room temperature, 0.2 ml Chloroform were added and subsequently vortexed for a minimum of 40 seconds until the dispersion turned white-dreary. Basically, procedures for RNA isolation of cell culture samples were equal, except suspending cells in 1 ml RNAPure reagent by using a cell scraper (Sarstedt AG & Co, Nürnbrecht, Germany) for homogenization.

Afterwards, the dispersions were incubated at room temperature for 10 minutes and centrifuged at 4 °C for 5 minutes at 12000 g. Carefully the upper, RNA-containing aqueous phase was transferred into a fresh 1.5 ml tube and subsequently 0.5 ml isopropanol were added. Samples were mixed assiduously and incubated at least for 10 minutes at 4 °C until recentrifugation at 4 °C for 10 minutes at 12000 g. Without disturbing the pellet, the supernatant was discharged, and the pellet was washed twice with 1 ml ethanol 75 %, vortexed and centrifuged again at 4 °C for 10 minutes at 12000 g. Depending on the size of the pellet, the RNA was resuspended in 10 - 100 µl RNase free water after gently drying on a cellulose tissue. For RNA concentration assessment and quality control, the RNA was measured with the Nanodrop Spectrophotometer ND 1000 (Peqlab, Erlangen, Germany). Concentrations as well as the 230, 260 and 280 nanometre (nm) absorbances were determined. The RNA samples were stored at - 80 °C until usage.

6.3.2 Reverse transcription

Reverse transcription-PCR (RT-PCR), which is based on the PCR method, represents the preferred technique utilized to detect and to quantify messenger RNA (mRNA) by synthesizing mRNA to its complementary DNA (cDNA). In this thesis, only a two-step protocol was used meaning that RT-PCR was perpetually combined with quantitative real-time PCR (qPCR) measuring the amplified cDNA fragments, thus reverse transcription and qPCR were performed in two different attempts.

Firstly, reverse transcription is enzymatically conversed by the enzyme reverse transcriptase, using oligo(dT)s as primers which recognize the poly A tail of each mRNA. Thus, the poly A tail constitutes the binding site for the reverse transcriptase. A typical RT-reaction was set up for one sample as follows on ice.

Component	Amount
RNA	100 - 600 ng
10 mM oligo(dT) - primer	1 µl
10 mM dNTPs	1 µl
ddH_2O (RNase free)	ad 12 µl

This mix was first incubated at 65 °C for 5 minutes and afterwards for 2 minutes at 4 °C in the Eppendorf vapo protect mastercycler pro (Eppendorf AG, Hamburg, Germany) followed by adding 8 µl of RT-PCR-Mastermix as shown below.

Component	Amount
Protoscript II reaction buffer 5x	4 µl
0.1 M DTT 10x	2 µl
Murine RNase inhibitor	1 µl
Protoscript II	1 µl

Samples were then incubated for 60 minutes at 42 °C and subsequently cycled for 5 minutes at 80 °C. The cDNA was cooled down to 4 °C or stored at - 20 °C until usage.

6.3.3 Quantitative real-time PCR

Real-time PCR enables both the detection and quantification of specific DNA sequences using a fluorescent dye, namely SYBR Green, which intercalates with the double-stranded cDNA fragments obtained from reverse transcription. The amplification of the cDNA products thus can be observed by the real-time PCR cycler (StepOne Plus, Applied Biosystems, Foster City, United States) as an increase of SYBR Green fluorescence in accordance to fluorophore 5-carboxyrhodamin (5-ROX) fluorescence as a reference value. When the SYBR Green fluorescence significantly exceeds the reference signal of 5-ROX, a quantitative value termed Cycle threshold (Ct) can be defined which is necessary for quantification using the ΔΔCt method. The amounts of the received cDNA were put in reference to the housekeeping gene ribosomal protein L32 (Rpl32).

The qPCR-mastermix was made for one sample as shown as follows in MicroAmp-Fast 96-Well Reaction Plates (Applied Biosystems, Foster City, United States) and sealed with Optical Adhesive Covers (Applied Biosystems, Foster City, United States). For value accuracy, samples were examined in triplets. As control for specific primer binding a melting curve analysis was performed after every real-time PCR reaction.

qPCR-mastermix

Component	Amount
Primer forward / reverse	0.25 µl each
FastStart Universal SYBR Green Master	6.25 µl
ddH_2O	3.75 µl
cDNA	2 µl (≙ 10-20 ng)

qPCR-program

Reaction step	Temperature	Time	Cycles
Pre-denaturation	95 °C	10 minutes	1
Denaturation	95 °C	15 seconds	40
Hybridization	60 °C	1 minute	
Elongation	65°C	1.5 minutes	
Melting curve			
	95 °C	15 seconds	
	60 °C	60 seconds	
	95 °C	15 seconds	

Table 9: Cycle protocol for quantitative real-time PCR. Denaturation, hybridization and elongation steps were repeated 40 times. As control for specific primer binding melting curve analyses were performed.

6.4 Protein methods

6.4.1 Protein isolation from tissue and cell culture samples

For protein isolation from different tissues as well as cell culture samples the lysis buffer “cell signalling” was prepared and every time freshly supplemented with phosphatase and protease inhibitors like shown below.

Phosphatase and protease inhibitors addendum

Component	Amount
Antipain (25 mg / ml)	2 µl
DTT (1 M)	5 µl
Leupeptin (25 mg / ml)	2 µl
Lysis buffer “cell signalling”	4741 µl
NaF (500mM)	125 µl
Na_3VO_4 (100mM)	50 µl
PAO (40 mM)	50 µl
PMSF (200 mM)	25 µl

All steps of protein isolation were performed on ice for both murine tissues and cells. The types of different tissues were frozen in liquid nitrogen in 1.8 ml cryotubes (Sarstedt, Nümbrecht, Germany) and subsequently either stored at - 80 °C or directly used for protein preparation. 800 µl of lysis buffer were needed per tissue sample, being subsequently homogenized with the ultra-turrax until the tissue was completely resolved. The disperger was cleaned after every sample rigorously in water and in 0.5 M NaOH to evite contamination. In case of necessity, 10 µl of 5 % benzonase were added and incubated at room temperature for 10 minutes. Afterwards, the lysates were vortexed and incubated in the ultrasonic ice bath (Bandelin electronic, Berlin, Germany) for 5-10 minutes, followed by centrifugation for 10 minutes at 4 °C and 14000 rpm. The supernatant was carefully transferred into a new 1.5 ml reaction tube and stored at - 20 °C.

Unlikely, cell culture dishes were carefully washed with DPBS, temporary dried for 2 minutes and directly resuspended with 150-300 µl lysis buffer, depending on cell confluency, using a cell scraper. Next, the lysates were pipetted up and down for several times. The lysates were transferred to a 1.5 ml tube, incubated for 10 minutes on ice and afterwards subjected to the same procedure as tissue samples as described above.

Determination of protein concentration

The protein concentration of lysates was assessed by Bradford Protein Assay which is a colourimetric protein assay based on the absorbance shift of the dye Coomassie Brilliant Blue G-250 for detection and quantification of total protein in solution. The red form of the dye is transferred into its bluer form building a complex with different protein side chains in an acidic environment. The bluer form can be measured at an absorbance of 595 nm. For this regard, 2 µl of the protein lysate were given to 1 ml of 1x Bradford solution. Afterwards, 200 µl of this

mixture were transferred in triplets onto a 96 well plate and absorbance was measured (Tecan infinite M200 Photometer/Luminator, Tecan Group, Männefeld, Swiss). Ensuing, mean values were evaluated by using BSA standards and a protein standard curve as reference.

6.4.2 SDS-Polyacrylamide gel electrophoresis

Sodium dodecyl sulfate polyacrylamide gel electrophoresis (SDS-PAGE), constitutes a technique for separation of proteins according to their molecular weight under denaturized conditions. The polymerization of two compounds, namely acrylamide and N, N-methylene bisacrylamide, leads to formation of polyacrylamide gels. Polymerization is initiated by the addition of ammonium persulfate (APS) as well as tetramethylethylenediamine (TEMED) as catalysts. Pore size of the gel is determined by the amount of acrylamide. Within this thesis, a discontinuous gel system was used, meaning that a separating, as well as a stacking gel with different pH values of running and gel buffer, were prepared. Depending on the size of the targeted proteins, either 8 % acrylamide separating gels for CUL7 detection or 12 % gels for blotting against AKT and ERK were used, meanwhile HSP90 served as a housekeeping gene for every detection. The compositions of the gels are shown below.

Separating gel 8 %

Component	**Amount**
Acrylamide 30 % + 0.8 Bis	1500 µl
Lower buffer	1425 µl
ddH_2O	1763 µl
Glycerol	938 µl
APS 10 %	27 µl
TEMED	5 µl

Separating gel 12 %

Component	**Amount**
Acrylamide 30 % + 0.8 Bis	2250 µl
Lower buffer	1425 µl
ddH_2O	1013 µl
Glycerol	938 µl
APS 10 %	27 µl
TEMED	5 µl

Stacking gel

Component	Amount
Acrylamide 30 % + 0.8 Bis	125 µl
Upper buffer	313 µl
ddH_2O	800 µl
APS 10 %	12 µl
TEMED	2 µl

For SDS gel casting, Mini-PROTEAN Tetra Cell Casting Stand (Bio-Rad, Munich, Germany) was used, keeping up cleaned glass plates and combs (1 mm). Without supplement of APS and TEMED, the mixtures for the stacking and the separating gel were set up in 50 ml falcon tubes (Sarstedt, Nümbrecht, Germany). Firstly, the completed separating gel was filled in between the glass plates, afterwards covered with water to avoid bubbles and dried for approximately 25 minutes at room temperature. After curing, the supernatant water was discharged, and the stacking gel was carefully pipetted above the separating gel after APS and TEMED were added. When both gels were completely polymerized, they were placed in the Protean 4 Mini gel electrophoresis chambers (Bio-Rad, Munich, Germany), the combs were removed, and the chambers were filled with 1x SDS running buffer according to the manufacturer's recommendation.

20-40 µg of protein were mixed with an appropriate volume of 4x LAEMMLI loading buffer and denatured by boiling at 99 °C for 5 minutes. Prior to loading of the denaturized protein lysates into the pockets of the stacking gel, the samples were centrifuged for several seconds at 14000 rpm and gel run was performed afterwards with 30 mA per gel for 1 hour. Precision Plus Protein All Blue Standards (Bio-Rad, Munich, Germany) was used as size marker.

6.4.3 Immunoblot (Western blot)

Within the SDS-PAGE technique, the separated proteins are transmitted to a PVDF membrane (PVDF Immobilon Transfer Membranes Immobilon-P, Merck Millipore, Darmstadt, Germany), meanwhile applying an electrical field. After activation of the gently agitating membrane in methanol for 5 minutes, it was laid down in between two Whatman papers soaked with 1x transfer buffer. The gel was rinsed carefully in transfer buffer and placed above the membrane. Air bubbles between the activated membrane and the gel should be avoided. Then blotting was performed for 2 hours at 375 mA with a cool pack in the chamber and next, blots were blocked overnight smoothly pivoting at 4 °C in BSA 5 % and PBST 0.05 % (1.25 g BSA in 25 ml PBST for one membrane).

Thereupon, the membranes were incubated with the first antibodies for 2 hours at room temperature under agitation on a tumbling table at 25 rpm (WT12, Biometra, Göttingen, Germany). The first antibodies were diluted as shown above (5.3) in 10 ml PBST 0.05 % containing 0.5 g BSA as well as 100 µl sodium azide 2 % and stored at - 20 °C. After incubation, the blots were washed 4 times for 5-10 minutes with PBST and subsequently incubated with the in PBST diluted secondary antibodies for 1 hour at room temperature under agitation. Afterwards, the membranes were once again washed for 4 times for 5-10 minutes. The detection was performed with the chemiluminescence reader LASmini4000 (Fujifilm, Düsseldorf, Germany) using the ECL 2 Western Blotting Substrate Kit according to the manufacturer's instructions. The intensity of the resulting protein bands was directly corresponding to the protein amount for whose quantification and analysis the Multi Gauge Software was used (Fujifilm, Düsseldorf, Germany).

Stripping of Western blot membranes

Stripping constitutes the removal of primary and secondary antibodies from Western blot membranes, thus being able to investigate more than one protein on the same blot. In this case, the stripping technique was used for the detection of phosphorylated AKT and ERK as well as their total protein levels. Therefore, the stripping buffer was warmed to 50 °C in a water bath and membranes were incubated 2 times for 20 minutes in hot stripping buffer under agitation, followed by 3 times of washing in PBST for 5 minutes. Membranes were then detected with the next primary antibody, starting from the blocking step as described above.

6.5 Histology in cardiac sections

6.5.1 Paraffin preservation and paraffin-sectioning

After removal of surrounding adipose tissue, murine hearts were intersected into 4 pieces for RNA purification, protein extraction, and paraffin preservation for diverse stainings. An approx. 1.5 mm thick axial slice of the ventricles was given into 4 % PFA solution and incubated at room temperature overnight under agitation. Afterwards, the PFA was discharged and heart slices were washed 3 times with PBS. With an automated Spin Tissue Processor (STP 120, Thermo Fisher Scientific, Surrey, United Kingdom) embedding steps were conducted, incubating the tissue in serial concentrations of ethanol for 2 hours each. Followed by treatment with Roti-Histol and liquid paraffin 2 times for 2 hours, the hearts were manually embedded in paraffin blocks on ice. Afterwards, the embedded tissue was cut into paraffin sections with a thickness of 6 µm, transferred on polylysine-coated slides (Thermo Fisher Scientific, Surrey,

United Kingdom) and dried at 42 °C. Paraffin slides were stored at room temperature in the dark until usage.

6.5.2 Hematoxylin/ Eosin staining

Due to Hematoxylin/ Eosin staining the cytoplasm of cardiac cells reveals pink and nuclei blue. Therefore, cardiac sections were deparaffinised and rehydrated as described as follows. First, the slides were incubated twice in toluene for 10 minutes, followed by a decreasing concentration line of ethanol, starting with incubation in 100 % ethanol two times for 5 minutes. Afterwards, slides were successively put for 5 minutes each into 90 %, 70 %, 50 % ethanol, and tap water. Next, Hematoxylin staining was performed with Hematoxylin solution for 2 minutes. Cardiac sections were afterwards washed firstly with tap water for 30 seconds, the second time for 2 minutes, followed by incubation in the Clarifier2 for 10 seconds, and then sluiced down in tap water for 60 seconds. Thereupon, slides were given into Bluing Reagent for 30-60 seconds and again washed with tap water for 1 minute. The counterstaining colouring eosinophilic structures was performed in 0.1 % Eosin solution for 1 minute and slides were subsequently dehydrated in tap water for 10 seconds, 80 % ethanol for 10-30 seconds, 100 % ethanol for 1 minute and 100 % toluene for 3 minutes. Finally, the slides were coated with approx. 50-70 µl DEPEX per sample (Thermo Fisher Scientific, Surrey, United Kingdom) and a 24 x 55 mm coverslip (Roth, Karlsruhe, Germany).

6.5.3 Sirius Red/ Fast Green staining

As described in 6.5.2, slides were deparaffinised in the same manner for Sirius Red/ Fast Green staining which was used for assessment of fibrosis in cardiac tissue highlighting collagens in red and cellular structures like cytoplasm in green.

Afterwards, slides were incubated in preheated Bouin's solution at 58 °C for 1 hour and rinsed in tap water for 10-15 minutes. Followed by staining in 0.1 % Fast Green for 30 minutes at room temperature, heart sections were washed in 1 % acetic acid for 1 minute and in tap water for 5 minutes. Dehydration was performed in 70 % ethanol for 10 seconds, in 100 % ethanol for 1 minute and in 100 % toluene for 3 minutes and conclusively the slides were covered as described above (see 6.5.2).

6.5.4 Wheat germ agglutinin staining

For wheat germ agglutinin staining, visualizing surface membranes, deparaffinization of slides was performed by consecutive incubation in xylene twice for 4 minutes, afterwards for two minutes each in 100 %, in 90 %, in 70 %, and in 50 % ethanol, then in ddH_2O and lastly in PBS for 1 minute. The antigen retrieval was performed using 10 mM sodium citrate buffer heating the sections for 4 minutes at 800 watts in the microwave with following rinsing 1 x in PBS. Around the heart sections, circles with a hydrophobic barrier pen (Pap Pen, Sigma, Taufenkirchen, Germany) were drawn, avoiding the free flow of the staining solutions. Next, WGA staining solution (Alexa Fluor 647 conjugate, Life Technologies, Carlsbad, United States) was diluted 1:100 in PBS and incubated on deparaffinised heart sections for 1.5 hours in a dark, humid incubation chamber at room temperature. This was followed by two washing steps with PBS. Nucleus staining was performed thereupon using SYTOX Green dye (Life Technologies, Carlsbad, United States), diluted 1:1000 in PBS, and slides were incubated in a dark, humid chamber for 10 minutes at room temperature with subsequent rinsing in PBS for 3 times. After removal of remaining liquids on the slides, sections were covered with one drop of Aquatex (Merck, Darmstadt, Germany) and 24 x 55 mm coverslips, dried at room temperature at least for 1 hour and stored at 4 °C up to one week until usage.

6.5.5 TUNEL staining

Terminal deoxynucleotidyl transferase dUTP nick end labelling (TUNEL) staining is a technique for detection of DNA fragments and for assessment of apoptotic cells. Therefore, In Situ Cell Death Detection Kit, TMR red (Roche, Mannheim, Germany) was used according to the manufacturer's advice for difficult tissue. For dewaxing, the slides were first incubated for 2 times in xylene for 4 minutes and then subjected for 2 minutes each to a decreasing serial concentration line of ethanol, namely to 100 %, to 95 %, to 90 %, to 80 %, and to 70 % ethanol. After rinsing the slides in PBS, they were put into 10 mM sodium citrate buffer, thus applying 800 watts microwave irradiation for 1 minute, and again immersed in PBS. Prior to the first blocking step with 10 mM dNTPs for 30 minutes at room temperature in a dark humid chamber, a hydrophobic barrier line was drawn around the heart sections. The second blocking step constituted the immersion of slides in 10 MM Tris/Cl pH 7.5, containing 3 % BSA and 20 % fetal bovine serum (FBS), for 30 minutes at room temperature, followed by 2 washing steps in PBS. Next, for positive control, 1 heart was incubated with DNase for 10 minutes, meanwhile 2 hearts were subjected to labelling solution as negative controls. The TUNEL reaction mixture was then incubated on heart sections for 1 hour at 37 °C in a humidified atmosphere in the dark, followed by 3 times of rinsing in PBS for 5 minutes. Excess fluid was drained off and

slides were covered with DAPI mounting medium, visualizing the nuclei, and sealed with a coverslip.

For image acquisition for all performed methods the subsequent set up was utilised: Software MetaMorph Basic Imaging Software Packets (Molecular Devices, Downingtown, United States), ImageJ software (U. S. National Institutes of Health, Bethesda, United States) Microscope AxioObserver.Z1, (Zeiss, Jena, Germany), Lumen200 fluorescence illumination system (Prior, Cambridge, United Kingdom), and Retiga-4000DC CCD camera (QImaging, Surrey, Canada).

6.6 Cell culture

6.6.1 Cultivation of HEK293T cells

HEK293T cells were mainly used for the production of AAV9. In this regard, thawed fresh cells were incubated in dishes with a diameter of 15 cm (Sarstedt, Nürnbrecht, Germany) in Dulbecco's Modified Eagle Medium (DMEM) (GIBCO, Karlsruhe Germany), containing 1 % Penicillin / Streptomycin (Pen / Strep) and 10 % FCS at 37 °C and 5 % CO_2, until the cells were confluent. At this point, cells were splitted by aspiration of the old growing solution, rinsed once in PBS and 5 ml 0.05 % Trypsin were added prior to transferring the cell dishes to the incubator for 5 minutes. Afterwards, different volumes of preheated medium were added to the detached cell suspension. This was depending on the desired confluency of the new cell culture plates, so that the cell suspension was either diluted 1:5 or 1:10. The cell dishes were supplemented by fresh preheated culture medium and restored in the incubation chamber until the transfer to triple flasks for virus production.

6.6.2 Isolation and cultivation of adult mouse cardiomyocytes and cardiofibroblasts

All buffers and media were prepared freshly and prewarmed in a water bath as described in 5.5 before the beginning of the cell isolation procedure. Additionally, dishes were coated with laminin for seeding of AMCMs and incubated at 37 °C and 5 % CO_2. Before starting the actual procedure, the mouse was heparinised with 50 µl heparin dissolved in 150 µl 0.9 % NaCl and 5 minutes later anaesthetised with 600-700 µl avertin solution intraperitoneally. As soon as the mouse was narcotised deeply, the heart was removed, erased off fatty tissue and cleaned in perfusion buffer. Thereupon the aorta was tied to a self-made plastic cannula of a perfusion

system (Julabo, type 13, pump type EC-BRÜ-PU; Amersham Bioscience, Little Chalfont, United Kingdom) under a microscope and the heart was retrogradely scoured out, first manually with perfusion buffer and then with a flow rate of 4 x 10 ml / h for 3 minutes. Afterwards, the heart was perfused with digestion buffer for 6-7 minutes with a constant flow of 4 x 10 ml / h, until the consistency of the heart was slightly softer, loose and fainter, followed by removal of the atria. The ventricles were then transferred into digestion buffer and carefully mechanically minced with a syringe for 3 minutes after the addition of 2.5 ml stop buffer P1. This was done until the heart was completely dissolved. After filtration of the suspension through a 100 µm cell strainer (Falcon 100µm Cell Strainer, Corning, New York, United States) into a falcon, it was incubated for 10 minutes in a 37 °C warm water bath for sedimentation of cardiomyocytes. For simultaneous isolation of AMCMs and AMCFs, the resulting supernatant was centrifuged for 1 minute at 55 g and again transferred carefully to a fresh 15 ml falcon for non-cardiomyocyte isolation. For this purpose, the supernatant was once again centrifuged for 5 minutes at 220 g at room temperature, followed by discharge of the supernatant. The pellet, containing cardiofibroblasts and non-cardiomyocytes, was dissolved in 10 ml of 10 % AMCF medium, plated on a 10 cm dish and incubated for 2 hours at 37 °C and 1 % CO_2. Next, the plates were washed twice in PBS and stored at - 80 °C for protein and RNA isolation.

However, for the cultivation of the cardiomyocyte cell fraction, the pellet and the sediment were pooled in 10 ml of stop buffer P2 and transferred into a 25 ml autoclaved conical flask. Calcium reconstitution was performed adding firstly 50 µl of 10 mM CaCl for 2 times, then 100 µl of 10 mM CaCl, afterwards 30 µl of 100 mM CaCl and finally 50 µl of 100 mM CaCl with an incubation time of 4 minutes for each step. The flask was gently pivoted for a short time during the respective incubation step. Afterwards, the cell suspension was transferred to a fresh 15 ml falcon tube and incubated at 37 °C for 10 minutes for sedimentation. Thereupon, the supernatant was centrifuged for 1 minute at 55 g and the thereof resulting supernatant was discarded without disturbing the pellet containing the cardiomyocyte fraction. Prior to the addition of 10 ml AMCM plating medium, the sediment and the pellet were pooled, and surplus laminin removed from the coated dishes. Cardiomyocytes were afterwards plated and incubated at 37 °C and 5 % CO_2 for 2 hours, followed by rinsing twice in PBS. The dishes were frozen and stored at - 80 °C until usage.

6.7 Production of AAV9

6.7.1 Electroporation of plasmids and transfection into HEK293T cells

Electroporation of plasmids and their amplification

The inverted terminal repeat regions (ITRs) of viral plasmids are necessary for viral replication and assembly, but they can be often lost during amplification in conventional Escherichia coli (E. coli) strains. This is the reason why for DNA amplification the strain E. coli SURE (Stratagene, La Jolla, United States) was preferred. Therefore, 50 µl of bacteria were thawed on ice, supplemented by 100 ng of plasmid DNA and transferred into a cuvette (Gene Pulser, Bio-Rad, Munich, Germany). After a short electrical stimulation through a pulse of 1.8 kV (Micro-Pulser, Bio-Rad, Munich, Germany), the bacteria were resuspended in 500 µl LB-medium and cultured for 1 hour at 37 °C and 800 rpm in a thermoshaker. Subsequently, 200 µl of the bacteria suspension were plated on agar, having as selection antibiotic Ampicillin (100 µg / ml), followed by incubation overnight at 37 °C.

Clones were then picked and used for large-scale production of plasmid DNA. One clone was selected and cultivated in 400 ml LB- or 2 l TB-medium, respectively. For amplification of AAV9-CMV-iCre as well as AAV9-CMV-dsRed plasmids, PureLink Maxiprep Kit and LB-medium were utilized according to the manufacturer's protocol. Since helper plasmids like pDP9rs were required in extremely large numbers, amplification and cultivation of plasmids were performed by using, therefore, PureLink Gigaprep Kit and TB-medium.

For verification of the isolated DNA, sequencing of AAV9-CMV-iCre as well as restriction digestion of all plasmids were performed (**Fig. 5**). For sequencing of the insert of the cre-carrying plasmid, 2 µg of DNA were diluted in 20 µl of ddH_2O and send to Eurofins Genomics (Ebersberg, Germany), where primers for sequencing were ordered and stored. The obtained results of the company were compared and controlled using the software MacVector Version 12.7.3 (MacVector, Cary, United States) which enables to exclude punctual mutations.

Moreover, restriction digestion was made to check the inverted terminal repeat (ITR) regions. Firstly, restriction enzymes AhdI and SmaI were used for dsAAV9-CMV-iCre as well as AAV9-CMV-dsRed, launching therefore 2 different restriction digestion mixes, respectively, containing one of both enzymes. For this purpose, either 1 µl AhdI or SmaI was added to 1 µl of CutSmart buffer and 0.5-1 µl of plasmid DNA (depending on DNA concentration; 0.5 µl for a concentration of 1 µg / ml DNA) and filled up to 10 µl with ddH_2O. Afterwards, the AhdI-mix was incubated at 37 °C for 1 hour whereas the SmaI-mix was incubated for 1 hour at 25 °C.

In contrast, for pDP9rs, a double digest was performed using the similar amounts of enzymes BamHI HF and ScaI HF and same aliquots of all other components with subsequent incubation at 37 °C for 1 hour.

Finally, for all plasmids gel electrophoresis, separating DNA fragments, was performed at 150 V and 400 mA for 30 minutes in a 1 % agarose gel using the same instruments as described in 6.2.2.

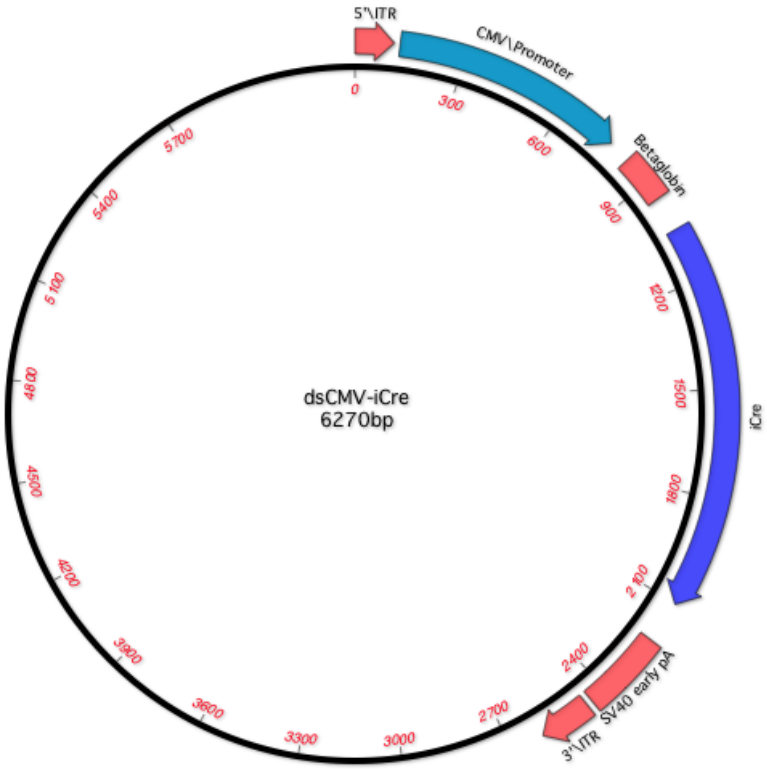

Figure 5: Genome map of AAV9-CMV-iCre. The plasmid consists of 6270 base pairs and is driven by a CMV promoter. The ITRs are required for the start of replication, packaging, integration in the host genome, and regulation of gene expression, whereas the *Rep* and *Cap* regions (for description of functions see 8.1) are replaced by the sequence encoding the Cre protein.

Transfection of HEK293T cells with plasmids for virus production

In the first instance, confluent grown cell dishes having a diameter of 15 cm had to be transferred into triple flasks (Thermo Fisher Scientific, Surrey, United Kingdom), containing a total volume of 110 ml medium per flask. For this regard, the number of required dishes for the desired count of triple flasks was calculated by the formula $number\ of\ cell\ culture\ dishes = \frac{3 \text{ x number of desired triple flasks}}{2.5}$.

Most of the time 5 triple flasks were produced per experimental group. For this reason, the medium of 12 cell dishes was aspirated, cells were washed once with PBS and then incubated with trypsin for 5 minutes as described in 6.6.1. Cell solutions of 6 dishes were afterwards transferred into 500 ml preheated DMEM medium containing 1 % Pen / Strep and 10 % FCS, followed by charge of 5 triple flasks with 110 ml medium each and incubation for 1 day until cells were rather confluent. Next, for transfection of the cells with plasmids being able to produce viral particles, polyethyleneimine (PEI) was used leading to endocytosis of plasmids. 2 mixes had to be set up as composed as follows for transfection of 5 triple flasks.

Mix 1

Component	**Amount**
vector plasmid (either dsAAV9-CMV-iCre or AAV9-CMV-dsRed)	139 µg
pDP9 helper plasmid	585 µg
DMEM medium (devoid of Pen / Strep)	ad 30 ml

Mix 2

Component	**Amount**
PEI	1550 µl
DMEM medium (devoid of Pen / Strep)	ad 30 ml

Both mixes were assembled, shortly vortexed and incubated at room temperature for 15 minutes under the hood. Afterwards, the transfection mix was given to prewarmed DMEM medium (1 % Pen / Strep, 10 % FCS), followed by replacement of the old medium in the triple flasks. The flasks were incubated at 37 °C and 5 % CO_2 for 72 hours until harvest of the virus.

6.7.2 Harvest and purification of the virus

Harvest of AAV9 and ultracentrifugation

For harvest of the virus, triple flasks were shaken vigorously while rapidly detaching the cells from the bottom, ensued by transfer of the medium into 500 ml conical centrifugation tubes (VWR International, Radnor, United States). Then 50 ml DPBS were given into the empty triple flasks for minimizing cell loss. Triple flasks were shaken again, and the resulting solution also transferred into centrifuge buckets. Centrifugation (Beckmann Coulter Biomedical, Munich, Germany) was performed at 4 °C and 1000 rpm for 15 minutes, followed by discharge of the supernatant afterwards. Pellets were washed in turn twice with 50 ml DBPS and centrifuged in 50 ml falcons at 4 °C and 220 g for 15 minutes with subsequent discharge of the supernatant.

Pellets, for AAV9-CMV-dsRed glowing strongly pink, were dissolved in 3-4 ml AAV-lysis buffer, attending a total volume of approximately 5 ml and could be stored afterwards at - 80 °C until the next step.

To lyse the cells and breakup cell structures, the cell suspension was thawed and warmed at 37 °C in a water bath and alternating frozen in liquid nitrogen for 15 minutes each and for 3 times, respectively. Subsequently, digestion of the cell rests was performed using 0.5 µl benzonase per 1 ml of suspension and it was incubated at 37 °C for 30 minutes in a water bath. After subsequent centrifugation at 4 °C and 3000 g for 15 minutes, the supernatant, containing the virus (approximately 4 ml), could be taken off.

For the separation of empty capsids and non-functional virus particles from virulent particles based on their different densities, an iodixanol gradient for ultracentrifugation was used. For this purpose, the gradient, as depicted in **Fig. 6**, of 15 %, 25 %, 40 % and 60 % iodixanol was set up in a Quick-seal centrifugation tube (Quick-seal Polypropylene tubes 16 x 76 mm, Beckmann Coulter Biomedical Biomedical, Munich, Germany) after transfer of the viral solution into it. The tubes were balanced with a difference smaller than 0.01 g, sealed (Quick-seal Cordless Tube TuppERKit 50 HZ, Germany) and covered with metal caps. The subsequent centrifugation was performed with an ultracentrifuge (Optima L-80 XP, Beckmann Coulter Biomedical Biomedical, Munich, Germany) using a 75Ti Rotor at 4 °C and 60000 rpm for 2 hours with maximal acceleration and a deceleration of 7. After centrifugation, the virus containing-phase (40 % iodixanol) could be drawn off with a sterile 20 Gauge thick needle (Sterican Standardkanülen, B. Braun Medical AG, Sempach, Swiss) while fixating the tube in a fastener. Another needle was put into the top of the tube for air exchange. Importantly, the other phases should not be disturbed, and approx. 1.5 ml viral solution could be taken off. The virus was collected in cryovials and could be stored at 4 °C up to 2 weeks until its purification.

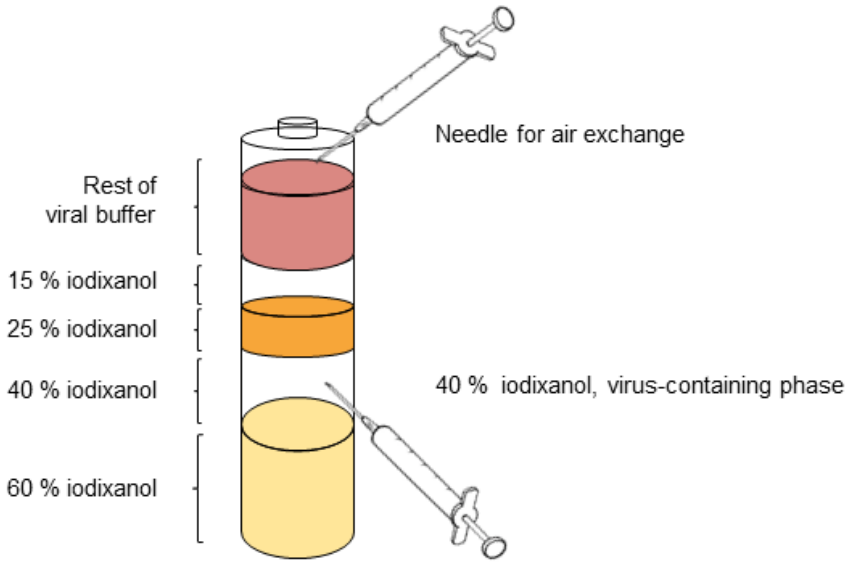

Figure 6: Ultracentrifugation and harvest of the virus using an iodixanol gradient. The iodixanol gradient was set up with decreasing concentrations of iodixanol (60 %, 40 %, 25 %, and 15 %). The virus-containing phase was the 40 % iodixanol phase and drawn off with a 20 gauge thick needle. For air exchange and avoidance of negative pressure, a second needle was inserted at the top of the centrifugation tube.

Purification and concentration of virus

Since iodixanol is toxic for neonatal hearts, it has to be leached out by several centrifugation and washing steps with sterile lactated Ringer's solution. Therefore, VIVASPIN centrifugation columns (Sartorius Stedim Biotech, Göttingen, Germany) were used, having a total capacity of 6 ml.

First of all, the column was washed twice with 4 ml of sterile lactated Ringer's solution by centrifugation at 4000 g and 20 °C for 5 minutes. The filtered eluates were discarded afterwards. The unconcentrated viruses were diluted 1:6 in lactated Ringer's solution and transferred into the upper compartment of the centrifugation tube. As before, 3-7 centrifugation steps at 4000 g for 2 minutes were performed as long as approximately 1 ml of the diluted virus remained in the column above the filter. The flow through in the bottom tube was removed. Afterwards, 5 ml of lactated Ringer's solution were once more added, releasing the virus of iodixanol, followed by several careful centrifugation steps as described before. The volume should not have been further reduced than a total volume of 500-800 µl, otherwise precipitation of the virus would have been risked. Next, the concentrated and purified viruses were collected from the upper tube, followed by measurement of the viral titers by qPCR.

Real-time PCR for AAV9 titration

Before running a qPCR for virus titration, the viral samples had to be pretreated. Therefore, 10 µl of the virus were added to 10 µl TE Buffer and 20 µl of 2 M NaOH and subsequently incubated for 30 minutes at 56 °C and 500 rpm. After supplementing 960 µl 40 mM HCl, the mix was cooled down at room temperature for 10 minutes before usage of 1 µl / well for the titration PCR. The PCR-mastermix for one well and the qPCR-program were performed as shown below. For calculation of the virus amount viral DNA plasmid standards, ranged from 10^5 to 10^{10}, were used, which were analysed afterwards with a pre-assembled concentration standard curve (**Fig. 7**). For mean value accuracy, samples were pipetted in triplets using the same set up for performing real-time PCR as described in 6.3.3.

PCR-mastermix

Component	**Amount**
FastStart Universal SYBR Green Master	12.5 µl
ddH_2O	10.5 µl
dsAAVqSV40 rw2 primer mix	1 µl
Virus lysate or plasmid standard	1 µl

Real-time PCR program

Reaction step	**Temperature**	**Time**	**Cycles**
Pre-denaturation	95 °C	10 minutes	1
Denaturation	95 °C	15 seconds	40
Elongation	60 °C	1 minute	

Table 10: Real-time PCR program for virus titration.

In general, typical viral concentrations ranged from 4 x 10^{12} viral particles per millilitre before purification to 5 x 10^{13} virus particles per millilitre afterwards. Virus solutions were diluted to a concentration of 1 x 10^{13} in sterile lactated Ringer's solution and stored as 100 µl aliquots in cryotubes at - 80 °C.

A

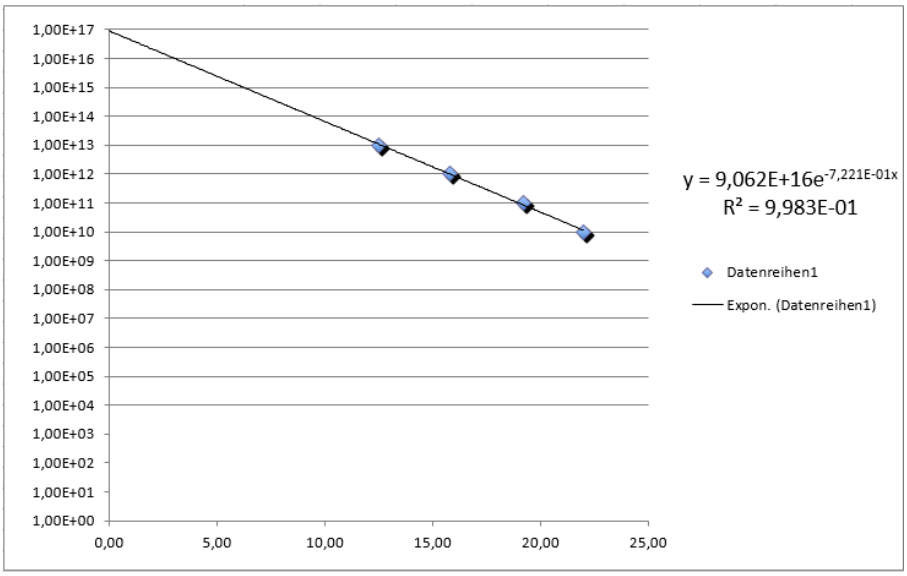

B

Standard 10	22,02	1,00E+10
Standard 11	19,22	1,00E+11
Standard 12	15,84	1,00E+12
Standard 13	12,53	1,00E+13
dsAAV9 - CMV - dsRed	9,10	1,27E+14
dsAAV9 - CMV - iCre	10,61	4,26E+13

Figure 7: Defining the titer of both AAV9s. (A) Example of an AAV9 titration standard curve. (B) Inserting Ct values into the formula of the standard curve of (A), AAV titers can be evaluated. Titers of 1.27 x 10^{14} for dsAAV9-CMV-dsRed and 4.26 x 10^{13} for dsAAV9-CMV-iCre after concentration and purification steps are presented.

6.8 Statistics

Data are presented as means ± SEM as not indicated otherwise. For testing the statistical difference between the means of two student's t-test was performed. To compare more groups one- or two-way ANOVA following Bonferroni post-test was utilized. For statistical calculation, GraphPad PRISM Ver. 6 (GraphPad Software, La Jolla, United States) was used and P-values < 0.05 were considered as statistically significant.

7 RESULTS

7.1 Generation of a cardiomyocyte-specific knockout of Cullin7 in a murine model

To generate a Cullin7 knockout mouse model in order to investigate the influence of Cul7 on cardiac disease and outcome, homozygous *Cul7*-floxed neonates (6.1.1) were injected intrapericardially with an adeno-associated virus of the serotype 9 encoding a Cre recombinase under a CMV-promoter (AAV9-CMV-iCre). At day 4 to 5 after birth mice were injected either with AAV9-CMV-iCre, inducing knockout of the protein, or AAV9-CMV-dsRed, representing the viral control, or lactated Ringer's solution as control for viral infection. This was followed by transthoracic echocardiography at an age of 4, 6 and 8 weeks. The mice were sacrificed with 8 weeks of age, parameters of cardiac morphology were analysed, and heart sections were subsequently examined regarding the development of fibrosis as well as cardiomyocyte hypertrophy (**Fig. 8**). Additionally, protein levels of CUL7 were determined in different tissues after AAV-injection under basal conditions.

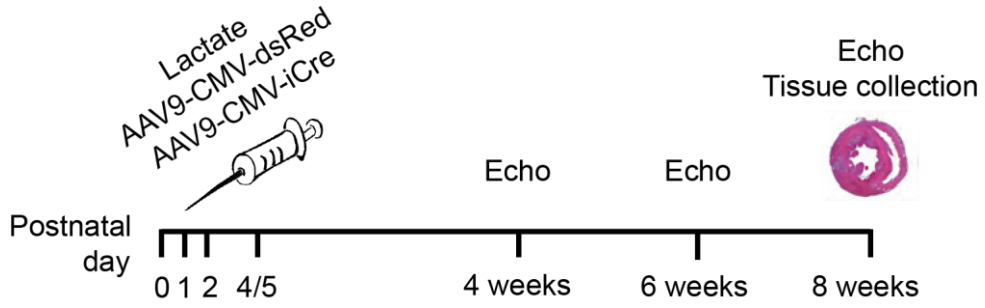

Figure 8: Experimental strategy and timeline. On day 4 to 5 after birth mice were transduced pericardially with AAV9-CMV-iCre, AAV9-CMV-dsRed or lactated Ringer's solution and subsequently the assessment of cardiac function and output was performed at an age of 4, 6 and 8 weeks by echocardiography (Echo). At week 8, mice were euthanized for further analysis of cardiac histology and cellular signalling.

7.1.1 Effective cardiomyocyte-specific deletion of the CUL7 protein in the murine heart

For verification of Cul7 depletion in cardiac tissue after virus injection, firstly a recombination PCR (6.2.1) was performed using isolated cardiomyocytes (**Fig. 9A**). An amplification product could be only observed in cardiomyocytes of Cul7$^{flox/flox}$;AAV9-CMV-iCre mice (lanes 6-9, n=3) whereas in the respective control animals (lanes 1-6, n=3) no recombination event took place. To further investigate the quantity of Cul7 depletion, qRT-PCR was performed, first in whole heart samples (**Fig. 9B**), and afterwards in isolated cell fractions of the heart (**Fig. 9C**), in order to understand which cell fractions were targeted as well as to investigate the impact of AAV9-CMV-dsRed injection on *Cul7* expression levels under basal conditions. In the whole heart, *Cul7* mRNA levels were reduced to 39.0 ± 0.05 % in comparison to the respective viral AAV9-CMV-dsRed control animals (n=7-9, $P < 0.001$). Furthermore, in AMCFs no reduction of *Cul7* mRNA was observed (n=3-9, $P > 0.05$) while in contrast a decrease by 60.1 ± 0.1 % (n=3-7, $P < 0.001$) of *Cul7* expression in adult mouse cardiomyocytes (AMCMs) was detected, underlining the cardiomyocyte tropism of AAV9-CMV-iCre. Next, the extent of CUL7 deletion in protein expression and also the affection of CUL7 by AAV9-CMV-dsRed viral vectors were assessed. The CUL7 protein abundance in AMCMs from Cul7$^{flox/flox}$;AAV9-CMV-iCre mice was found to be significantly reduced by 79.9 ± 0.1 % (n=3-7, $P < 0.01$) in comparison to both control groups (**Fig. 9D**). Between the control groups, no difference in CUL7 levels could be observed, indicating that AAV9-CMV-dsRed delivery does not alter Cul7 expression on both mRNA and protein levels (**Fig. 9E**). In conclusion, CUL7 knockdown was sufficiently mediated by intrapericardial delivery of AAV9 which is particularly targeting cardiomyocytes, whereas the non-cardiomyocyte cell fraction remained unaffected.

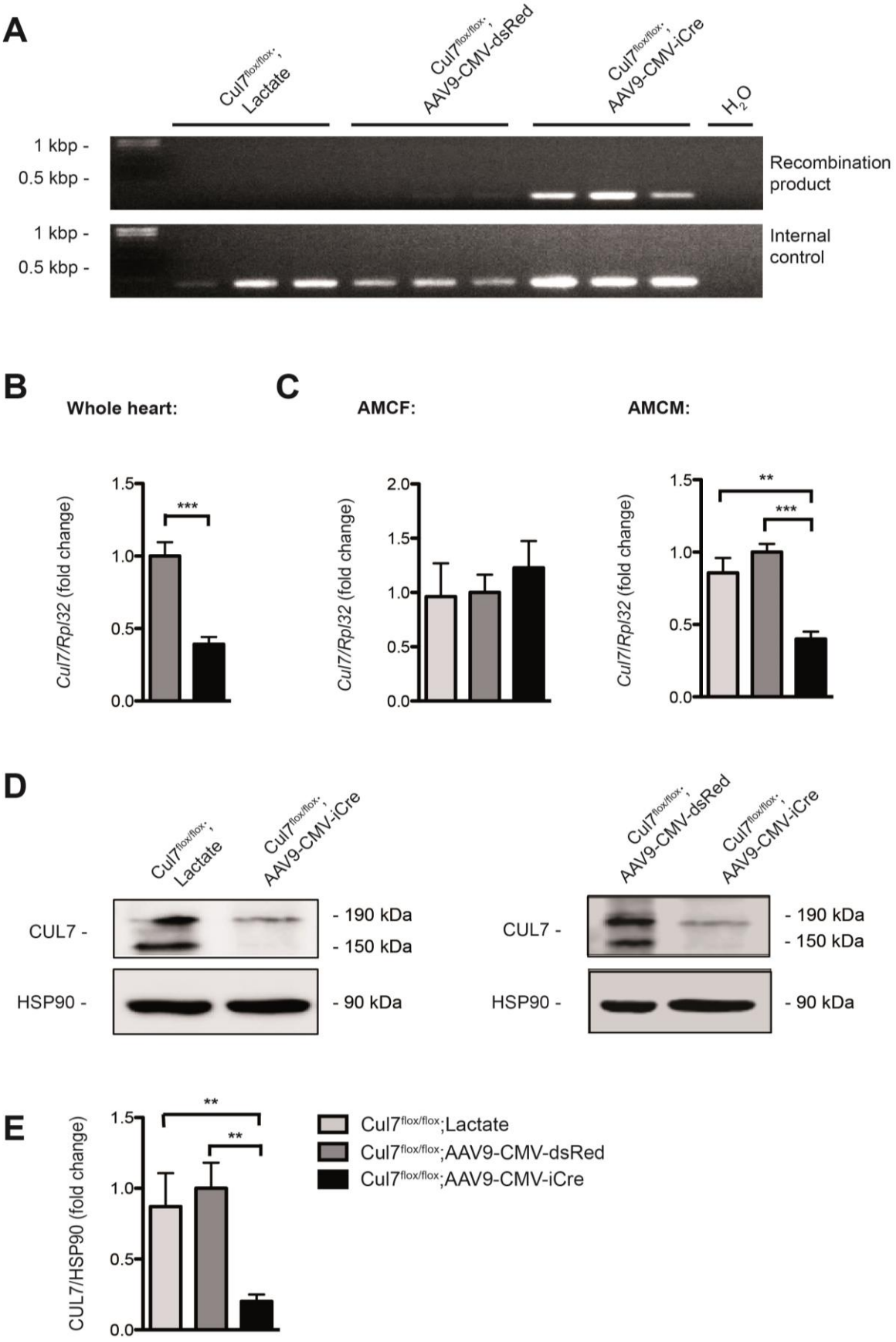

Figure 9: Ablation of CUL7 after injection of AAV9. All mice were sacrificed at 8 weeks of age for this experiment. Data are shown as fold change normalized to respective control animals. (A) Recombination PCR screening for recombination events in isolated

cardiomyocytes, n=3 per group. (B) Real-time RT-PCR analysis for *Cul7* mRNA relative to the housekeeping gene *Rpl32* in whole heart samples. n=7-9 mice/group; *** P < 0.001 (student's t-test). (C) Examination of *Cul7* mRNA expression levels in isolated cell fractions of the heart using qPCR. n=3-9 mice/group; ** P < 0.01, *** P < 0.001 (one-way ANOVA + Bonferroni post-test). (D) Lysates of isolated cardiomyocytes were subjected to immunoblot studies to evaluate the abundance of the CUL7 protein referred to HSP90. Representative immunoblots depicted for cardiomyocyte-specific CUL7 knockdown compared to respective lactate (left) and AAV9-CMV-dsRed treated animals (right). (E) Quantification of protein levels. n=3-7 mice/group; ** P < 0.01 (one-way ANOVA + Bonferroni post-test).

7.1.2 Biodistribution of AAV9 in different types of tissue

Since it is well known that pericardial injection of AAV9 in neonates leads to superior global gene transfer also to non-cardiac tissues due to biodistribution of the virus (Bish, Morine et al. 2008), several organs of mice at an age of 8 weeks were subjected to immunoblot analysis studying the impact of virus delivery under basal conditions. Since the liver, the lungs, the spleen and the kidney function as regulators of metabolic processes and hormone balance, they have an influence on blood pressure as well as on cardiac function. For this reason, these organs were selected for investigation and subsequently immunoblot analysis against CUL7 was performed (**Fig. 10A**). In all examined organs a reduction of CUL7 expression was observed (**Fig. 10B**), most prominent in kidney and spleen. However, for all of them, the reduction was not statistically significant by virtue of great variances of the knockdown efficiency in these organs (n=3-7, P > 0.05). Additionally, no macroscopical changes in these organs could be observed.

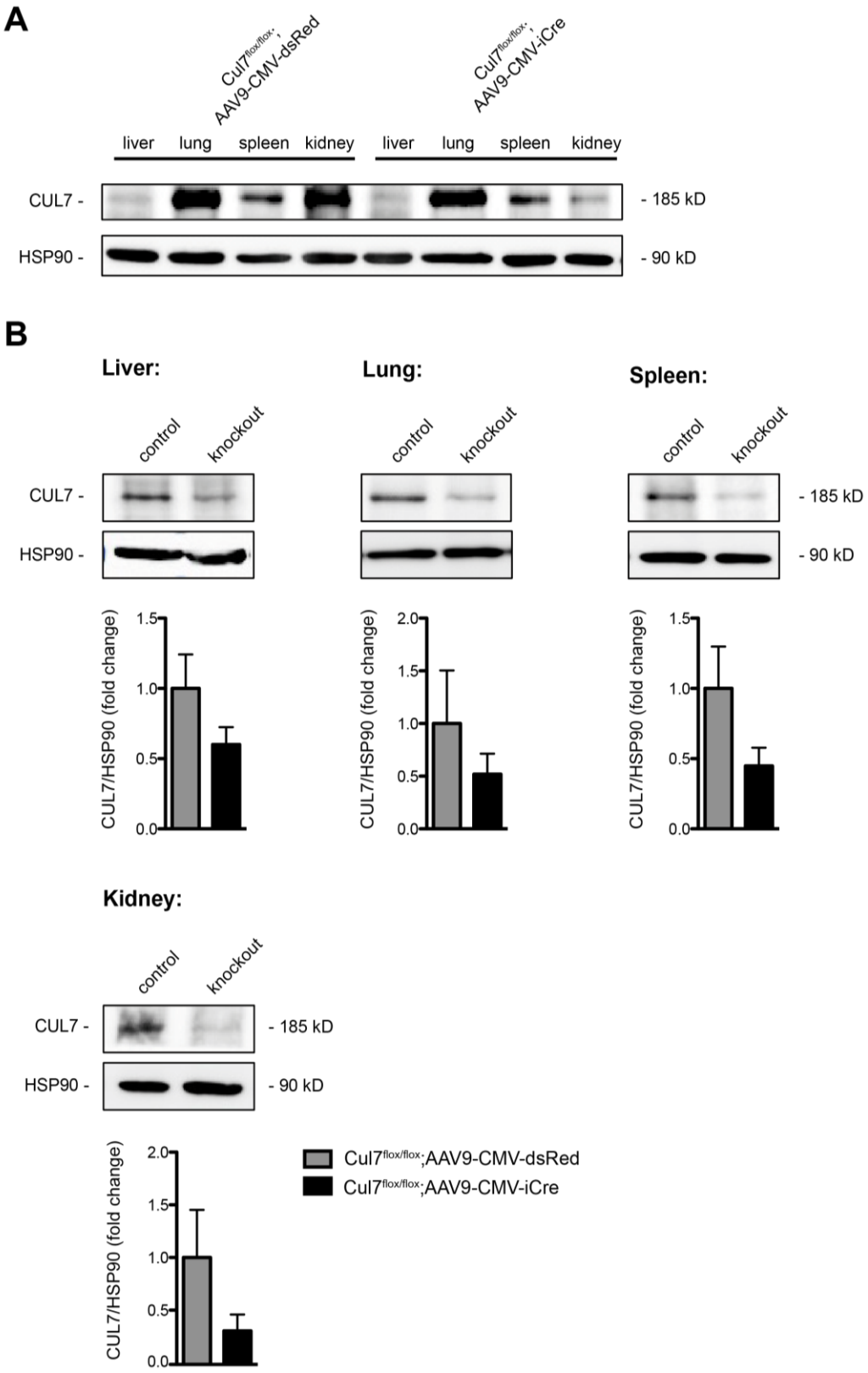

Figure 10: Global gene transfer of AAV9 in different types of tissue. Data are shown as fold change normalized to respective control animals. (A) Representative Western blot depicted for basal CUL7 expression levels in the liver, the lung, the spleen and the kidney in comparison to CUL7 abundance in these organs of CUL7 deficient mice. HSP90 served as housekeeping gene. (B) Direct line-up of organs and corresponding quantifications of CUL7 protein amounts referred to HSP90 (upper panel immunoblots and lower panel quantifications). Values are not statistically significant. n=3-7 mice/group; * $P < 0.05$ (student's t-test).

7.1.3 Cardiac phenotyping under basal conditions

To assess the impact of Cul7 ablation on cardiac structure, 8 week old mice were sacrificed, and parameters of cardiac morphology were determined. More specifically, heart weight, body weight, lung weight as well as tibia length were measured and therefrom ratios were built (**Fig. 11A-C**). It could be observed that mice injected with AAV9-CMV-dsRed displayed a moderate diminution of heart weight/tibia length- as well as of heart weight/body weight-ratio (HW/BW: 4.8 ± 0.03 mg/g, n=8) in comparison to lactate treated animals (HW/BW: 5.3 ± 0.1 mg/g, n=6, $P < 0.01$), which was not detectable in the respective CUL7 depleted animal group (HW/BW: 5.2 ± 0.1 mg/g, n=5, $P < 0.05$) (**Fig. 11A-B**). However, lung weight/tibia length-ratio remained unchanged for all experimental groups (**Fig. 11C**). Generally, all ratios displayed common values for 8 week old mice depicting no macroscopic toxic effect of viral delivery and intrapericardial injection in neonates.

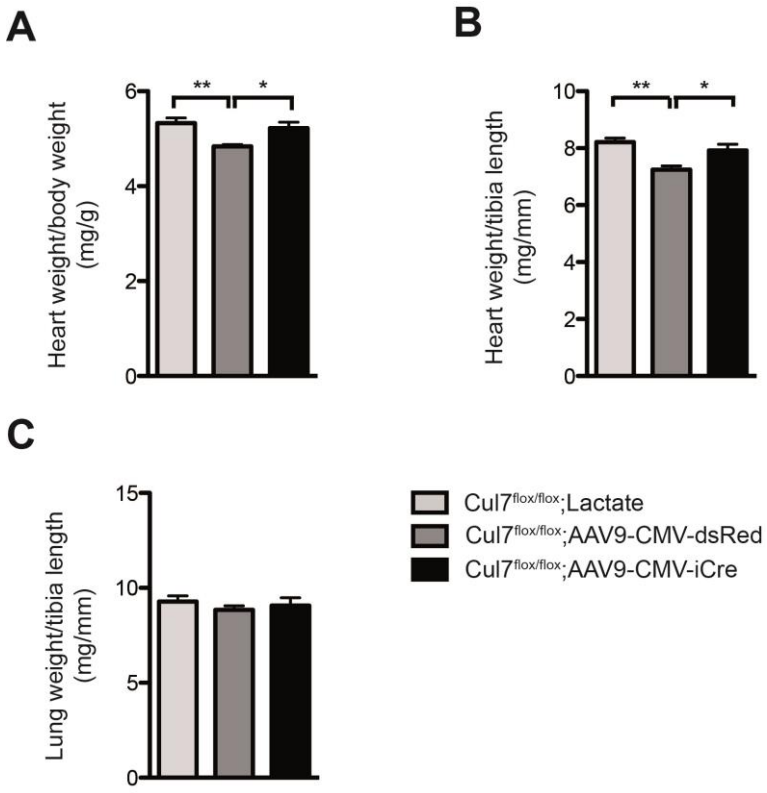

Figure 11: Cardiac phenotyping of Cullin7 deficient mice under basal conditions. (A-C) Screening for macroscopic cardiac hypertrophy by assessment of heart weight/body weight- (A), heart weight/tibia length- (B), and lung weight/tibia length-ratio (C). n=5-8 mice/group; * $P < 0.05$, ** $P < 0.01$ (one-way ANOVA + Bonferroni post-test).

7.1.4 Assessment of parameters of cardiac function

To evaluate the impact of cardiomyocyte-specific depletion of CUL7 on cardiac output over the course of time, heart function was monitored at 3 different time points. The mice had an age of 4 weeks (**Fig. 12A**), 6 weeks (**Fig. 12B**), and 8 weeks (**Fig. 12C**), when cardiac dimensions were assessed. In this regard, the cardiac parameters fractional shortening (FS), ejection fraction (EF), left ventricular, systolic and diastolic internal diameter (LVID $_{d/s}$), and left ventricular, systolic and diastolic volume (left ventricular volume $_{d/s}$) were calculated and their correlation determined. At any point of time, no significant alteration in cardiac function in between the experimental groups was detectable, but yet an improvement by trend in EF as well as FS of Cul7$^{flox/flox}$;AAV9-CMV-iCre mice when compared to respective Cul7$^{flox/flox}$;AAV9-CMV-dsRed animals, foremost aged 4 (FS Cul7$^{flox/flox}$;AAV9-CMV-dsRed: 30.2 ± 1.7 %, n=11 vs. Cul7$^{flox/flox}$;AAV9-CMV-iCre: 33.0 ± 2.0 %, n=11, P > 0.05) and 8 weeks (FS Cul7$^{flox/flox}$;AAV9-CMV-dsRed: 24.5 ± 0.8 %, n=11 vs. Cul7$^{flox/flox}$;AAV9-CMV-iCre: 26.7 ± 1.0 %, n=8, P > 0.05). Interestingly, despite this amelioration by trend concerning the functional parameters, the morphological parameters LVID $_{d/s}$ and ventricular volume $_{d/s}$ showed a tendency towards decreased values in *C*ul7 deficient mice. At an age of 4 weeks, *Cul7*$^{-/-}$ mice displayed for instance a systolic left ventricular volume of 18.6 ± 2.2 µl (n=11), whereas the AAV9-CMV-dsRed cohort showed a systolic left ventricular volume of 21.1 ± 3.0 µl (n=11, P > 0.05), indicating that knockout mice develop a mild cardiac hypertrophy resulting in moderate reduced systolic and diastolic volumes. However, these tendencies towards improved cardiac function are not statistically significant under basal conditions.

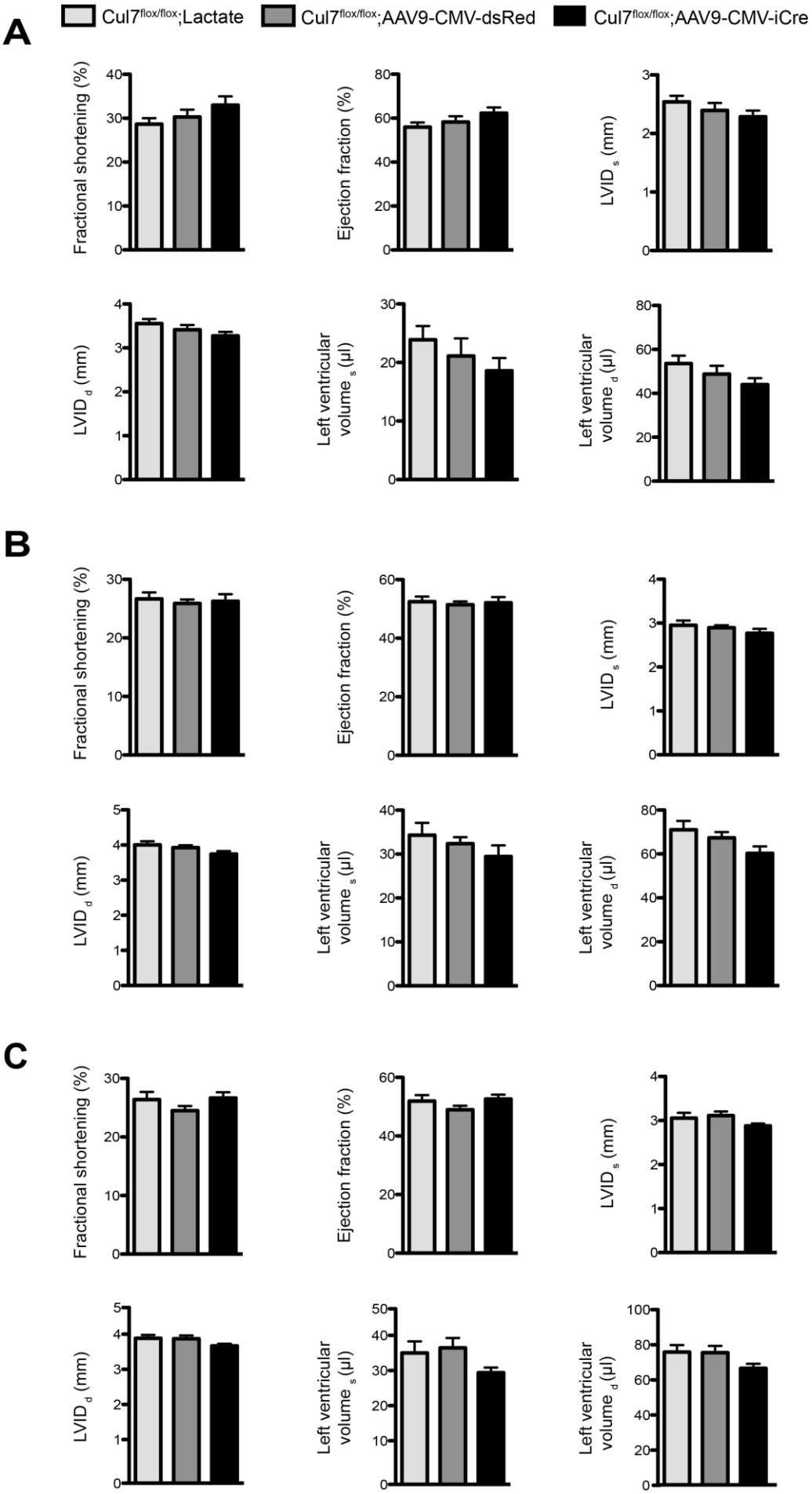
A
Cul7flox/flox;Lactate
Cul7flox/flox;AAV9-CMV-dsRed
Cul7flox/flox;AAV9-CMV-iCre
Fractional shortening (%)
Ejection fraction (%)
LVIDs (mm)
LVIDd (mm)
Left ventricular volumes (µl)
Left ventricular volumed (µl)
B
Fractional shortening (%)
Ejection fraction (%)
LVIDs (mm)
LVIDd (mm)
Left ventricular volumes (µl)
Left ventricular volumed (µl)
C
Fractional shortening (%)
Ejection fraction (%)
LVIDs (mm)
LVIDd (mm)
Left ventricular volumes (µl)
Left ventricular volumed (µl)

Figure 12: Echocardiographic assessment of cardiac function. 4 weeks old mice underwent echocardiographic assessment with measurement of fractional shortening, ejection fraction, left ventricular internal diameter in diastole and systole as well as systolic and diastolic left ventricular volume (A). Presentation of same data contents of 6 (B) and 8 (C) week old mice compared to respective control animals, injected either with lactated Ringer's solution or AAV9-CMV-dsRed. n=8-11 mice/group; * $P < 0.05$ (one-way ANOVA + Bonferroni post-test).

7.1.5 Influence of CUL7 knockdown on cardiac hypertrophy under basal conditions

Within the findings described in 7.1.3, a wheat germ agglutinin assay was performed on myocardial sections, as designated in 6.5.4, assessing cardiomyocyte hypertrophy and cell growth (**Fig. 13**). For this purpose, heart sections of 8 week old male mice were collected and 2 sections of the left ventricle, each composed of approx. 100 cells, were analysed. In this case, too, in line with the findings of cardiac phenotyping, the analysis of heart sections revealed an inclination towards increased cardiomyocyte size in the $Cul7^{flox/flox}$;AAV9-CMV-iCre cohort (375.3 ± 22.1 μm^2, n=6) when compared to $Cul7^{flox/flox}$;AAV9-CMV-dsRed control animals (343 ± 4.8 μm^2, n=8, $P > 0.05$). Nevertheless, this effect was not statistically significant, underlining the already observed very mild effects.

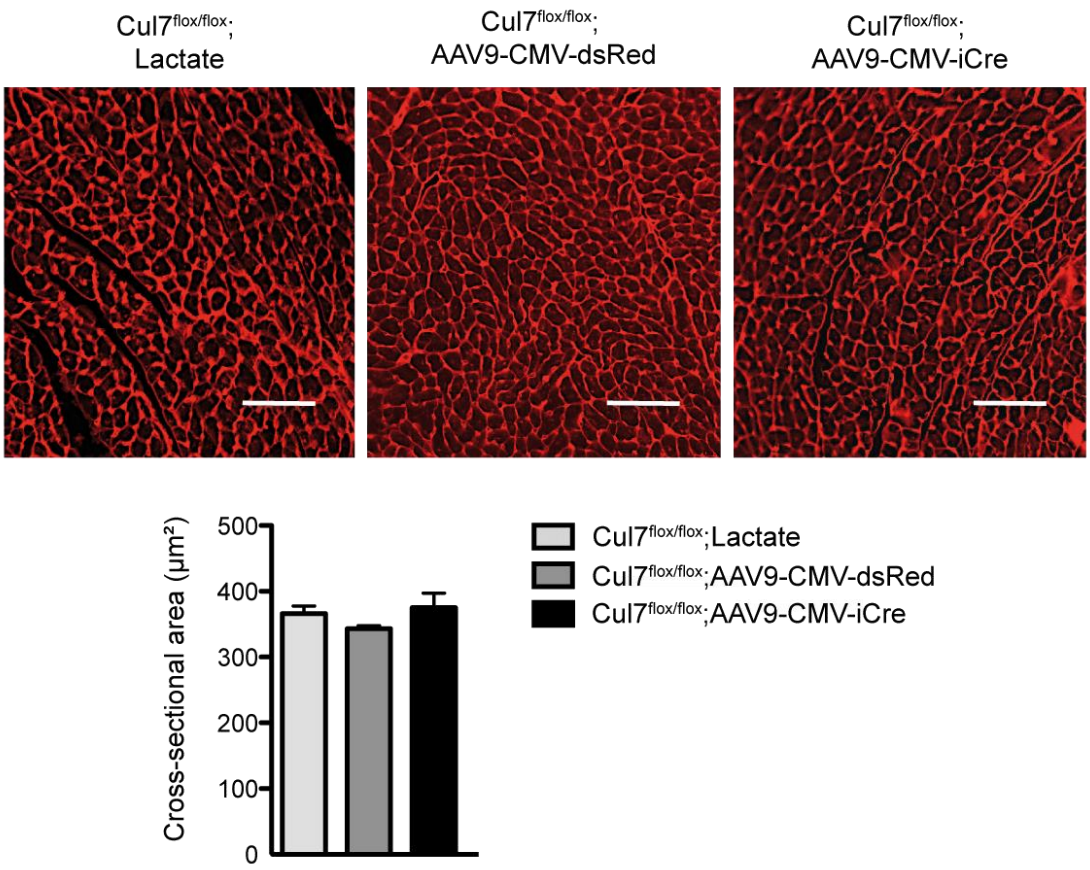

Figure 13: Cross-sectional area of cardiomyocytes under basal conditions. Wheat germ agglutinin staining in representative myocardial sections (upper panel) and quantification of cross-sectional area (lower panel) from automated cardiomyocyte size quantification. Cells were analysed by pixel counting on digitized images in an automated manner. n=4-8 mice/group; * $P < 0.05$ (one-way ANOVA + Bonferroni post-test); scale bar = 100 µm.

7.1.6 Impact of CUL7 depletion on left ventricular fibrosis

Recently it was shown, that mice expressing a dominant negative mutant of Cul7 develop smaller scar sizes as well as less fibrotic cardiac remodelling after myocardial infarction, accompanied by an amelioration of left ventricular function (Hassink, Nakajima et al. 2009). In this thesis, cardiac fibrogenesis was determined by Sirius Red/ Fast Green staining highlighting collagens in red (**Fig. 14**). Under basal conditions, Cul7$^{flox/flox}$;AAV9-CMV-iCre mice showed only a tendency by trend towards less fibrotic area and cardiac remodelling (1 ± 0.04 % interstitial fibrotic area, n=7), which was, however, not statistically significant when compared to respective Cul7$^{flox/flox}$;AAV9-CMV-dsRed control animals (1.3 ± 0.2 % interstitial fibrotic area, n=9, $P > 0.05$).

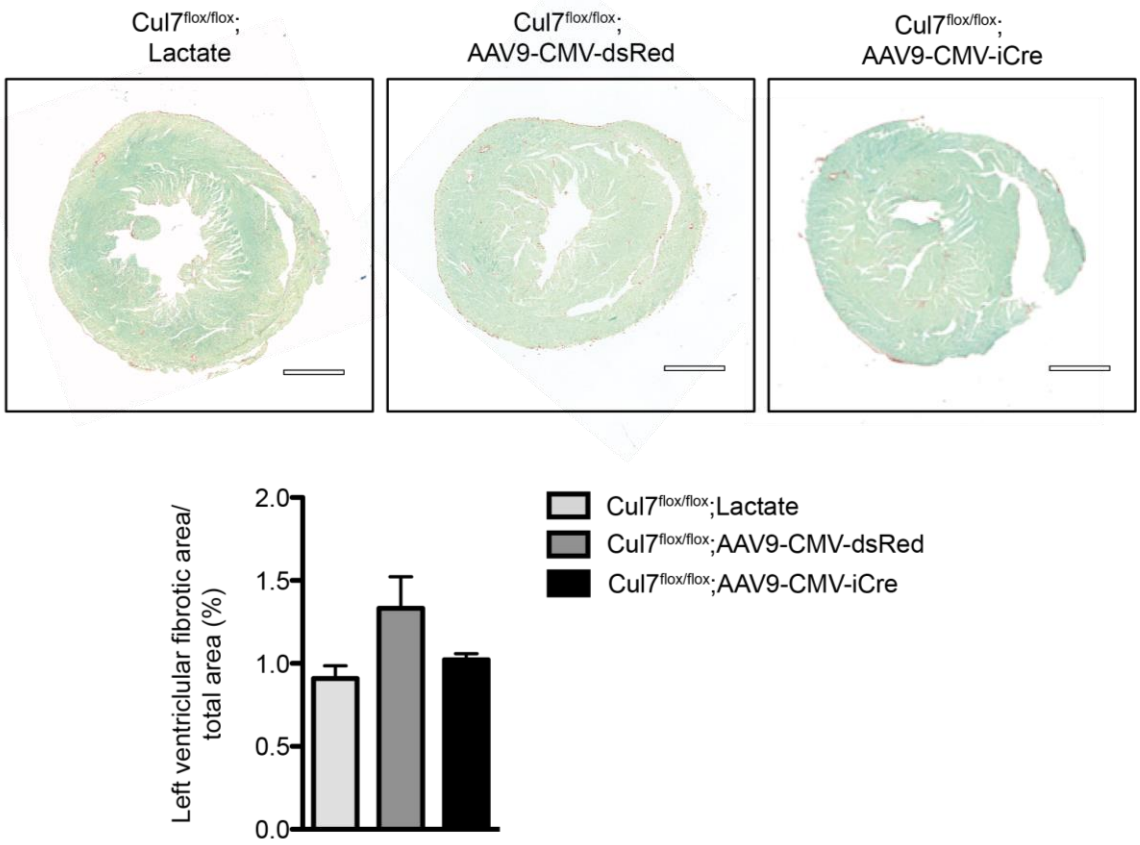

Figure 14: Histological analysis for myocardial fibrosis under basal conditions. Representative heart sections stained for fibrosis (Sirius Red/ Fast Green; upper panel) and corresponding quantitative data (lower panel). Under basal conditions, no significant differences of left ventricular fibrotic area could be observed between the experimental groups. n=6-9 mice/group; * P < 0.05 (one-way ANOVA + Bonferroni post-test); scale bar = 1 mm.

7.2 Influence of CUL7 deletion in maladaptive cardiac hypertrophy

Since, as described above, it is shown that mice expressing a dominant negative mutant of Cul7 develop a phenotype under the stress and inflammation model myocardial infarction (Hassink, Nakajima et al. 2009), within this thesis mice were subjected to transverse aortic constriction surgery to induce a different type of cardiac disease stimulus. This model is broadly used in small animals to examine cardiac hypertrophy and heart failure in vivo (Rockman, Ross et al. 1991). After a short compensatory phase, mice develop pathologic cardiac hypertrophy due to chronic pressure overload as well as a strong fibrotic response in the course of cardiac remodelling. For this purpose, the 3 experimental cohorts Cul7$^{flox/flox}$;Lactate, Cul7$^{flox/flox}$;AAV9-CMV-dsRed and Cul7$^{flox/flox}$;AAV9-CMV-iCre were subjected to TAC or sham surgery at an age of 9 weeks, respectively, and euthanized after 3 weeks of TAC for further histological analysis after the assessment of cardiac function (**Fig. 15**).

Figure 15: Experimental set-up and timeline of the TAC study. For evaluation of the influence of increased afterload, transverse aortic constriction (TAC) surgery was performed at the age of 9 weeks with preceding echocardiographic measurements. Subsequently, after 3 weeks, cardiac characterization of the operated mice was performed by echocardiography, phenotyping, and histological investigation.

7.2.1 Cardiac phenotyping after transverse aortic constriction

To assess the effectiveness of Cul7 ablation under conditions of increased afterload, whole heart samples were obtained after the animals underwent transverse aortic constriction or respective sham operation for 3 weeks (**Fig. 16A**). With these whole heart samples quantitative RT-PCR was performed, showing a downregulation by 59.0 ± 0.1 % of *Cul7* mRNA in the sham group (n=4, $P < 0.01$) and by 50.1 ± 0.2 % in the TAC cohort (n=4-5, $P < 0.05$). Moreover, to elucidate whether the operation was sufficient enough to cause maladaptive cardiac hypertrophy being evident in parameters of cardiac morphology, heart weight/body weight-, heart weight/tibia length- and lung weight/tibia length-ratios were determined. In this regard, a highly statistically significant difference between the sham and the respective TAC groups could be observed (sham vs. TAC for heart weight/body weight- and heart weight/tibia length-ratio: $P < 0.001$) (**Fig. 16B-C**). In the TAC groups 3 weeks after surgery, the heart weight/body weight-ratios had a significant 1.4-1.7-fold increase due to greater heart weight (**Fig. 16B**) in concordance with a significant 1.5-1.7-fold increment of heart weight/tibia length-ratios (n=5-6, $P < 0.001$) (**Fig. 16C**). This underlines the subsequent hypertrophic cardiac response after ligation of the aortic arch when compared to the respective sham cohorts. However, within the TAC cohort, no statistically significant difference in mice either injected with AAV9-CMV-iCre or AAV9-CMV-dsRed could be observed (n=5-6, $P > 0.05$). The lung weight/tibia length-ratio, examining left ventricular heart failure, showed a 3-fold change in aortic-banded, lactate treated animals (sham: 8.6 ± 0.3 mg/mm vs. TAC: 24.1 ± 3.0 mg/mm, n=6, $P < 0.001$) when compared to respective sham control mice pointing out an extensive backward failure for

Cul7$^{flox/flox}$;Lactate mice after TAC surgery, accompanied by the most increased heart weight. These signs of heart insufficiency were not observable in both viral cohorts (**Fig. 16D**).

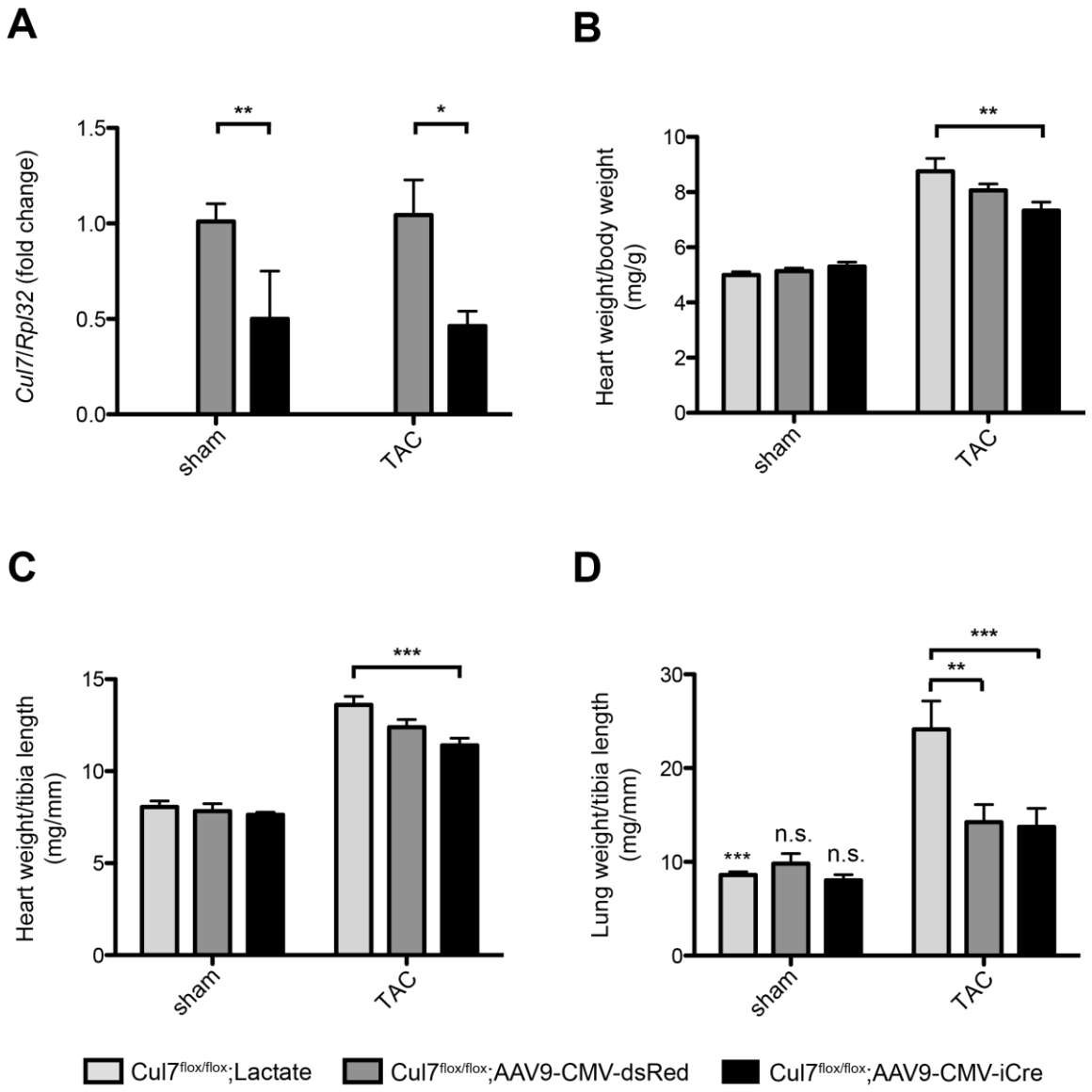

Figure 16: Evaluation of *Cul7* expression levels and cardiac morphology after transverse aortic constriction and sham surgery. (A) Quantitative qPCR analysis for *Cul7* expression in whole heart samples 3 weeks after TAC or sham surgery. n=4-5 mice/group; * $P < 0.05$, ** $P < 0.01$ (student's t-test). Heart weight/body weight- (B), heart weight/tibia length- (C) and lung weight/tibia length-ratio (D). n=5-6 mice/group; ** $P < 0.01$, *** $P < 0.001$. Sham vs. TAC as not indicated otherwise (B-C): *** $P < 0.001$ (two-way ANOVA + Bonferroni post-test).

7.2.2 Assessment of heart function under conditions of increased afterload

To determine the extent of cardiac disease after TAC, cardiac function was assessed by echocardiography to define more precisely the obtained macroscopic and morphologic measurements before and after the surgeries. For this reason, the heart dimensions fractional shortening, ejection fraction, left ventricular internal diameter $_{d/s}$ and left ventricular volume $_{d/s}$ were once again calculated. At baseline prior to the invasive treatment, no significant difference in all aforementioned parameters could be observed, indicating no adverse impacts of the pre-treatment in neonatal mice **(Fig. 17A-C)**. In the functional parameters of heart activity, namely FS, a mild tendency towards an increased FS in knockout mice could be observed, which did not reach statistical significance **(Fig. 17A).** For example, Cul7 deficient mice of the TAC cohort displayed a fractional shortening of 27.7 ± 1.5 % whereas the corresponding Cul7$^{flox/flox}$;AAV9-CMV-dsRed control group showed a FS of 25.7 ± 1.7 % (n=5, P > 0.05). Additionally, as mentioned in 7.1.4, the same observations concerning the volumetric measurements of the heart were made, at the most in both systolic and diastolic left ventricular volumes of the TAC knockout group when compared to the respective TAC control cohorts **(Fig. 17C)**. Taken together, at baseline, heart function of all experimental groups did not differ from each other representing equivalent assumptions prior to transverse aortic constriction surgery (n=4-6, P > 0.05).

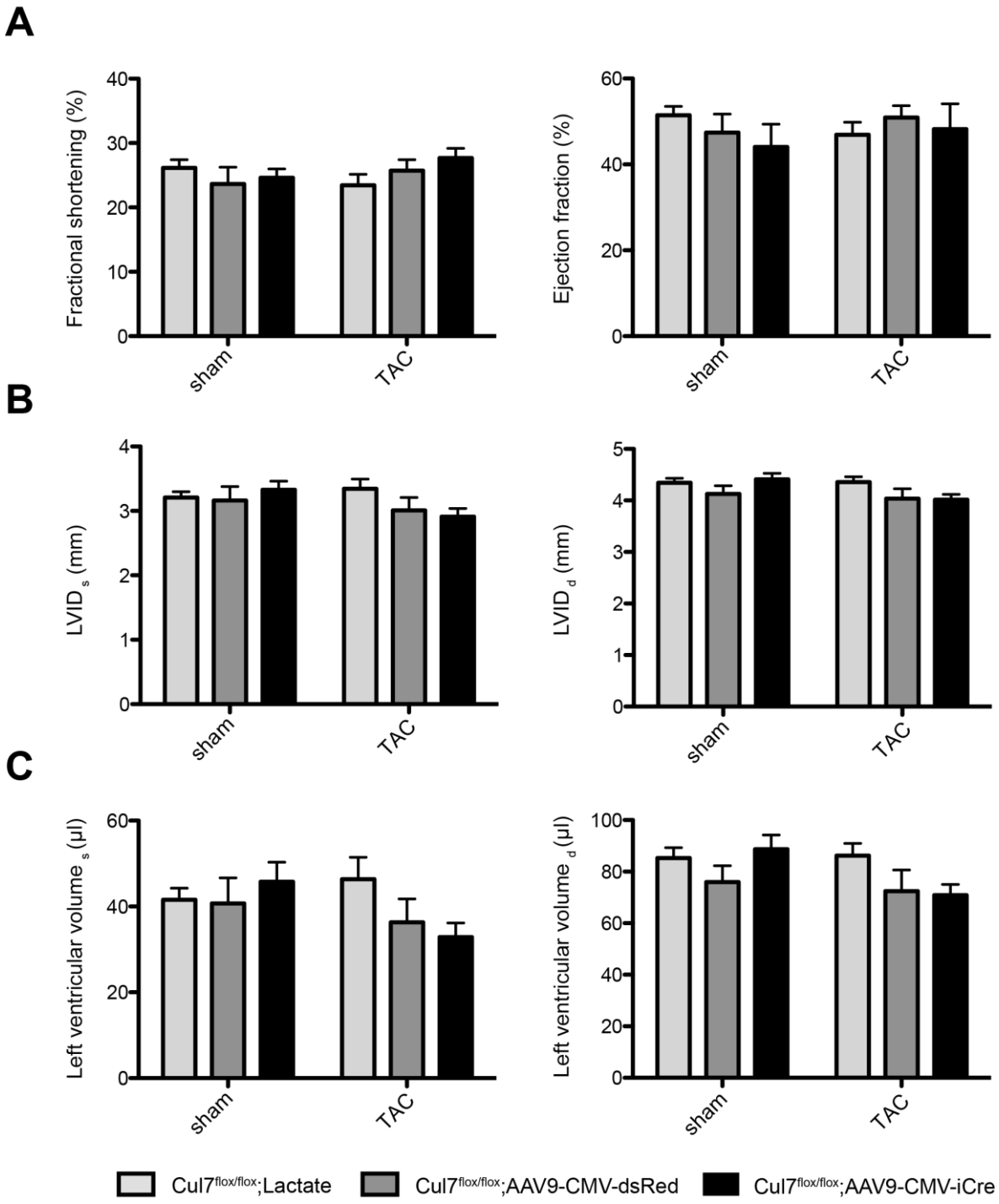

Figure 17: Cardiac morphometric dimensions and function prior to operation procedures. The heart function of the mice was analysed by pulse-wave Doppler echocardiography before TAC and sham surgery. Lanes 1-3 sham cohort, lanes 4-6 TAC cohort. (A) Functional parameters FS and EF before the operation. (B) Left ventricular, systolic (left) and diastolic (right) internal diameter before operation of the sham and the respective TAC cohort. (C) Systolic (left) and diastolic (right) left ventricular volume. n=4-6 mice/group, * $P < 0.05$ (two-way ANOVA + Bonferroni post-test).

After 3 weeks of sustained pressure overload, animals displayed a deterioration of the functional heart parameters FS and EF when compared to their iso-genetic sham-operated control cohort, reaching solid statistical significance (**Fig. 18A)**. In comparison of the sham and the TAC cohort, FS was reduced for 17.5 % within the knockout animals and even more pronounced, for 36.5 % in the respective AAV9-CMV-dsRed injected animals (e.g. FS of AAV9-CMV-dsRed sham group: 23.6 ± 2.2 %, n=4 vs. FS of AAV9-CMV-dsRed TAC group: 15.0 ± 3.4 %, n=5, $P < 0.001$). Furthermore, FS of *Cul7*$^{-/-}$ animals decreased from 27.7 ± 1.5 % prior TAC to 18.0 ± 1.0 % after surgery (n=5-6, $P < 0.001$). In contrast, the sham groups displayed a constantly stable cardiac function (e.g. FS of Cul7$^{flox/flox}$;AAV9-CMV-iCre mice before sham operation: 24.6 ± 1.4 % vs. after sham surgery: 21.8 ± 1.0 %, n=6, $P > 0.05$). These results underline the success of the TAC surgery with subsequent induction of heart disease.

Global heart insufficiency was probably induced within the lactate treated mice which is reflected in all obtained measurements after TAC. The Cul7$^{flox/flox}$;Lactate TAC cohort displayed more impaired heart dysfunction (**Fig. 18A**) and stronger dilation of the left ventricle than both other experimental groups (**Fig. 18B-C**). For instance, lactate treated TAC animals displayed a LVID $_s$ of 4.4 ± 0.3 mm whereas in the corresponding knockout group a LVID $_s$ of 3.4 ± 0.2 mm was measurable (n=6, $P < 0.01$). Nevertheless, after 3 weeks of TAC, there was no alteration in LVID $_{d/s}$ as well as in left ventricular volume $_{d/s}$ when comparing iso-genetic sham and TAC animals injected either with AAV9-CMV-iCre or AAV9-CMV-dsRed, pointing out the initial compensatory hypertrophic phase which is, in general, completely resolved after 5-6 weeks of increased afterload (n=4-6, $P > 0.05$) (**Fig. 18B-C**). Taken together, the increment of afterload by transverse aortic constriction surgery caused depression of cardiac function evidenced by the reduction of fractional shortening and ejection fraction - foremost in the control group which has received lactated Ringer's solution. Ablation of CUL7 under conditions of increased afterload was not sufficient enough to induce an improvement of heart function or rather an amelioration of cardiac dysfunction when comparing Cul7 deficient mice to their corresponding AAV9-CMV-dsRed control cohort, equal to observations that were made under basal conditions.

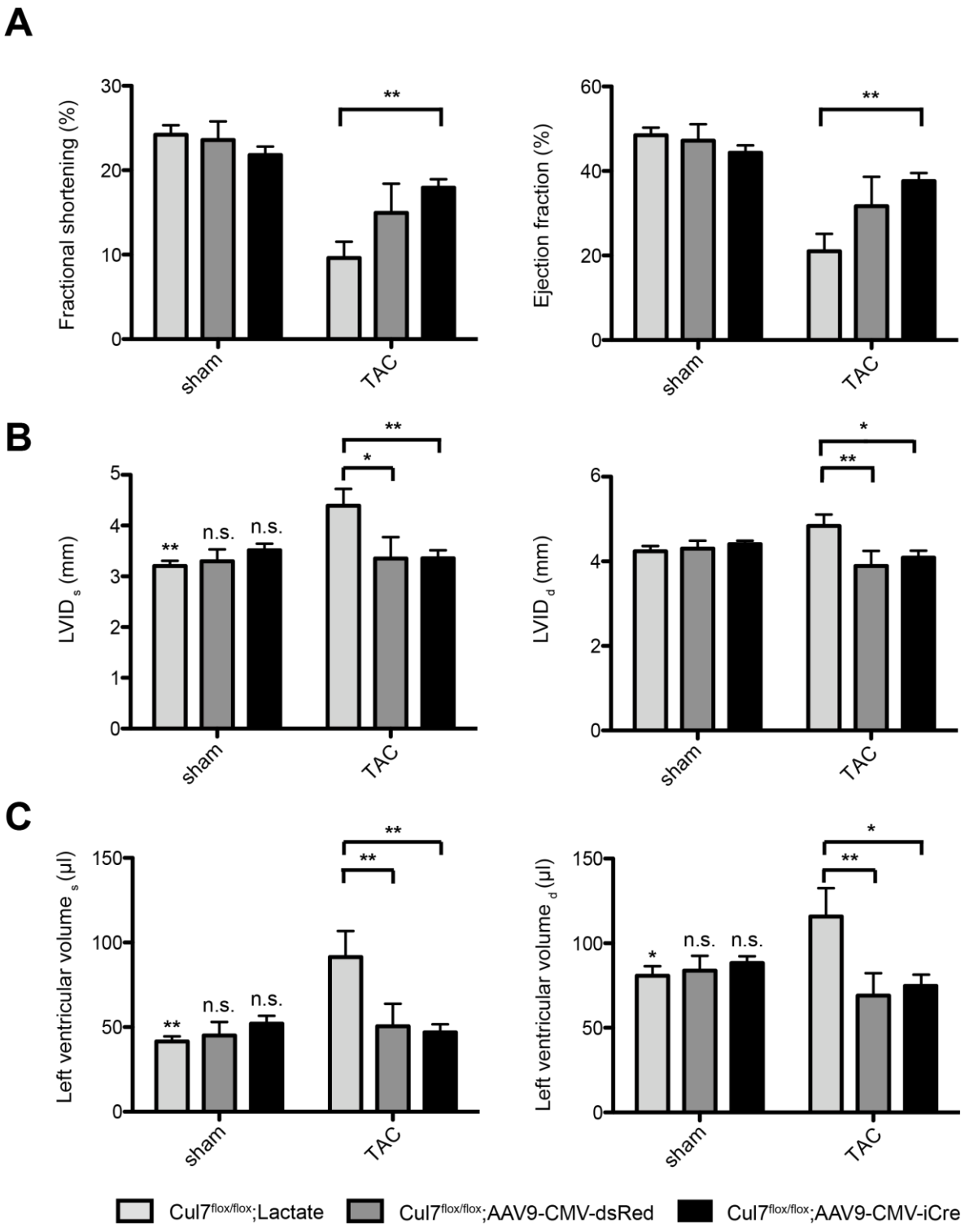

Figure 18: Cardiac morphometric dimensions and function 3 weeks after surgical procedures. Heart function of the mice was analysed by pulse-wave Doppler echocardiography after sham and TAC surgery. Lane 1-3 sham cohort, lane 4-6 TAC cohort. (A) Functional parameters FS and EF after the operation. Sham vs. TAC *** $P < 0.001$ (two-way ANOVA + Bonferroni post-test). (B) Left ventricular systolic (left) and diastolic (right) internal diameter after operation of the sham and the respective TAC cohorts. Sham vs. TAC as not indicated otherwise: n.s. not significant (two-way ANOVA + Bonferroni post-test). (C) Systolic (left) and diastolic (right) left ventricular volume. n=4-6 mice/group; n.s. not significant, * $P < 0.05$, ** $P < 0.01$ (two-way ANOVA + Bonferroni post-test).

7.2.3 No effect on cardiac hypertrophy under sustained pressure overload

To determine the effects of increment of afterload on cardiomyocyte hypertrophy, heart sections were subjected to wheat germ agglutinin staining elucidating cross-sectional area (**Fig. 19)**. After 3 weeks of intervention, the cross-sectional area of aortic-banded Cul7$^{flox/flox}$;Lactate (569.5 ± 14.5 µm^2, n=6, P < 0.01), Cul7$^{flox/flox}$;AAV9-CMV-dsRed (553.1 ± 19.4 µm^2, n=5, P < 0.05), and Cul7$^{flox/flox}$;AAV9-CMV-iCre animals (585.0 ± 7.8 µm^2, n=6, P < 0.001) significantly increased when compared to their respective sham-operated controls (Cul7$^{flox/flox}$;Lactate: 485.5 ± 30.0 µm^2, n=6 vs. Cul7$^{flox/flox}$;AAV9-CMV-dsRed 465.4 ± 20.0 µm^2, n=5 vs. Cul7$^{flox/flox}$;AAV9-CMV-iCre animals 450.7 ± 6.9 µm^2, n=5), demonstrating cardiac hypertrophy induced by transverse aortic constriction in a microscopic or rather a cellular context. However, there was no difference detectable between Cul7 deficient mice and the matching control animals after TAC surgery, taking up the findings under basal conditions.

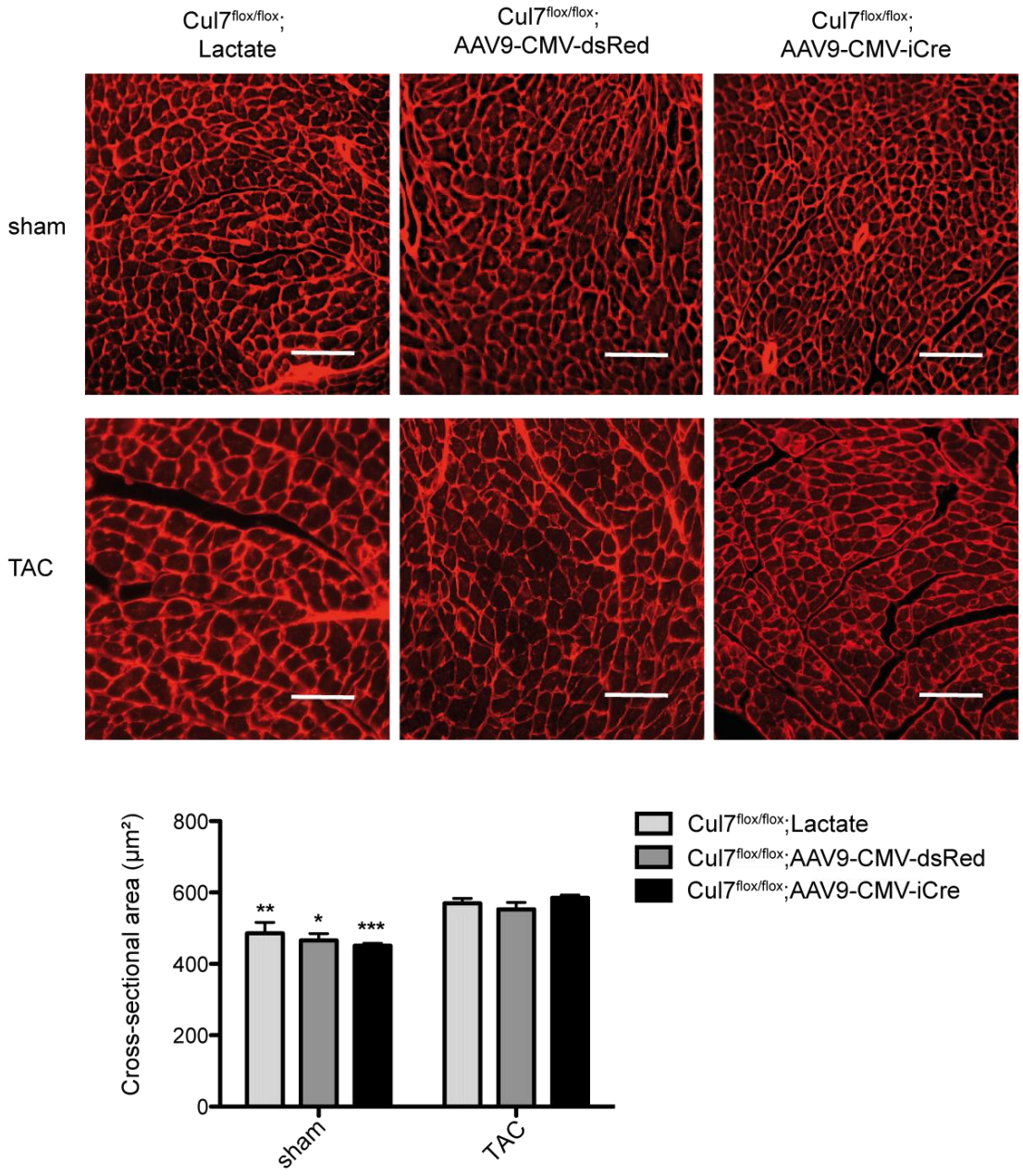

Figure 19: Cardiac hypertrophy under conditions of increased afterload. Wheat germ agglutinin staining on representative myocardial sections of sham-operated animals (upper panel) and mice subjected to transverse aortic constriction (lower panel). Quantification (down below) of cross-sectional area figuring out cardiomyocyte hypertrophy. Cells were analysed by pixel counting on digitized images in an automated manner. n=5-6 mice/group; sham vs. TAC: * $P < 0.05$, ** $P < 0.01$, *** $P < 0.001$ (two-way ANOVA + Bonferroni post-test); scale bar = 100 µm.

7.2.4 Attenuation of interstitial cardiac fibrosis in Cullin7 deficient mice

Since transverse aortic constriction induces a strong fibrotic response primarily in perivascular areas followed by sprawling out the myocardium, the degree of left ventricular fibrosis under conditions of increased afterload was examined by Sirius Red/ Fast Green staining. In mice not expressing CUL7 anymore, a reduction of fibrotic formations after 3 weeks of TAC was observed (**Fig. 20**) when likened to both control cohorts (Cul7$^{flox/flox}$;AAV9-CMV-iCre TAC group: 3.4 ± 0.9 % vs. Cul7$^{flox/flox}$;AAV9-CMV-dsRed TAC group: 6.7 ± 1.1 %, n=5-6, $P < 0.01$). Furthermore, no significant difference in cardiac fibrosis of *Cul7*$^{-/-}$ mice after cardiac insult in between the sham (1.3 ± 0.2 %, n=6) and the TAC group (3.4 ± 0.9 %, n=6, $P > 0.05$) could be detected. When comparing these results in contrast to both other experimental groups, left ventricular fibrosis showed a 5-6-fold increase (Cul7$^{flox/flox}$;AAV9-CMV-dsRed sham: 1.0 ± 0.1 % vs. Cul7$^{flox/flox}$;AAV9-CMV-dsRed TAC: 6.7 ± 1.1 %, n=5, $P < 0.001$). The sham cohorts expressed common values for left ventricular fibrotic area, comparable to the obtained results under basal conditions (7.1.5).

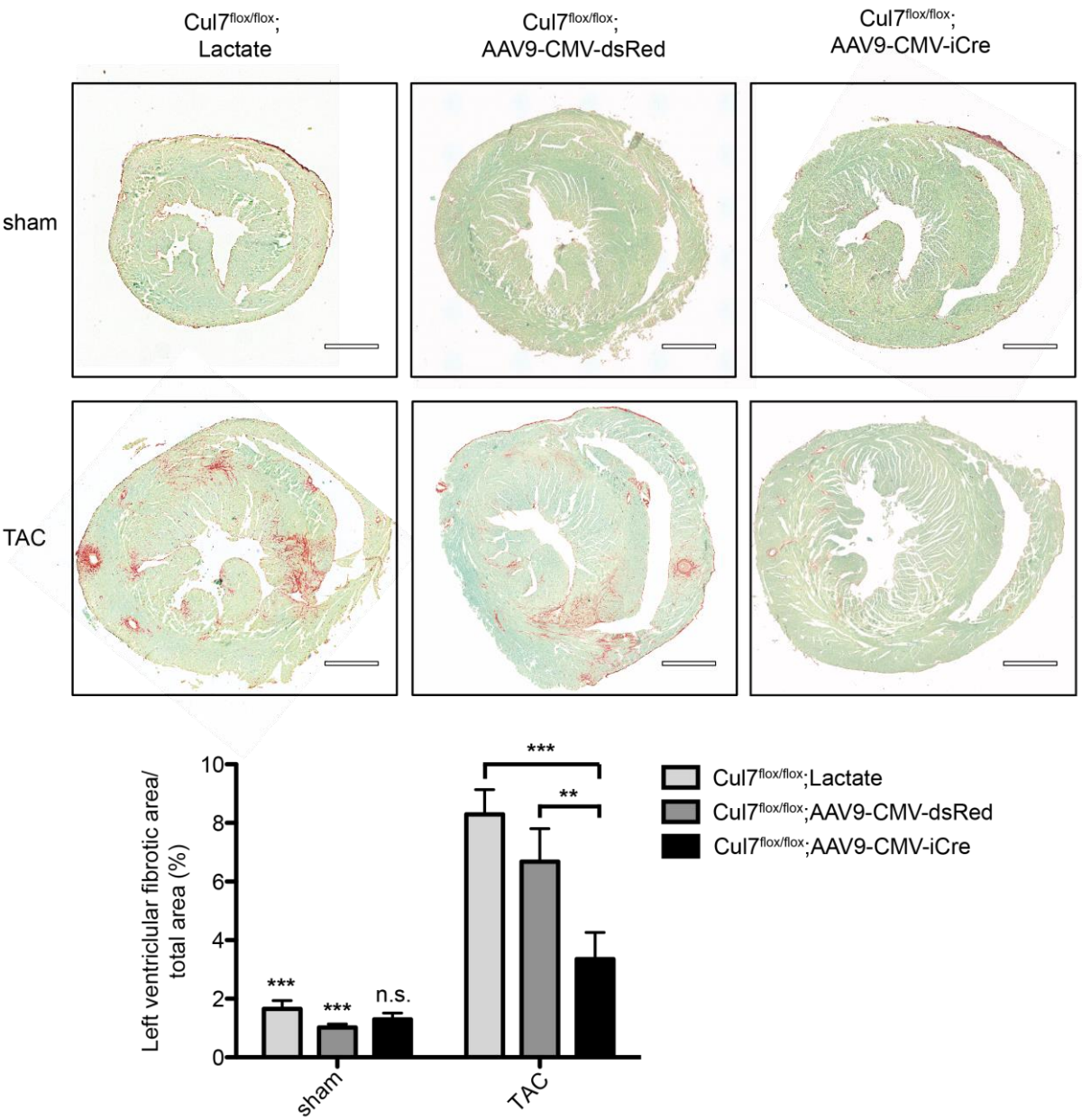

Figure 20: Loss of CUL7 results in less cardiac fibrosis under conditions of increased afterload. Representative myocardial sections stained with Sirius Red/ Fast Green visualizing cardiac fibrosis. The upper panel represents the sham experimental group, the lower one the TAC cohort. Quantification as shown down below. n=5-6 mice/group; n.s. not significant; ** P < 0.01, *** P < 0.001 (two-way ANOVA + Bonferroni post-test); scale bar = 1 mm.

7.3 Illumination of underlying signalling pathways

To further understand the reduced fibrotic response in cardiac disease upon cardiomyocyte-specific CUL7 depletion, some signalling pathways, where Cullin7 takes part in the degradation of several well-known substrate molecules, were investigated to descriptively illuminate underlying mechanisms. Recently, it was shown that the Cullin-RING E3 ubiquitin ligase 7

plays a pivotal role in insulin signalling as well as glucose homeostasis leading to degradation of AKT and ERK (Scheufele, Wolf et al. 2014). Thus, AKT, ERK, as well as IRS-1 were examined for their role as degradation targets of CUL7 and subsequently, well-described targets and key players of fibrogenesis were investigated. Furthermore, apoptosis of cardiomyocytes was determined via TUNEL staining.

7.3.1 Activation of AKT signalling upon Cullin7 ablation in isolated cardiomyocytes

In AMCMs of mice being sacrificed at an age of 8 weeks, the effect of Cullin7 depletion was examined in the PI3K/AKT and MAPK/ERK signalling pathways via assessment of protein levels by immunoblotting. Phosphorylated protein levels were normalized to their total protein amounts. Interestingly, in the cardiomyocyte fraction of knockout mice, phospho-AKT (p-AKT) / total-AKT (t-AKT) ratio was upregulated by the factor of 3 (**Fig. 21A**) when compared to respective AAV9-CMV-dsRed control animals ($n=5$, $P < 0.01$). Similar to results that were found in *Cul7*$^{-/-}$ MEFs displaying a more pronounced upregulation of AKT than of ERK as well as of IRS-1 upon insulin stimulation (Scheufele, Wolf et al. 2014), phospho-ERK (p-ERK) (**Fig. 21B**) activity and IRS-1 (**Fig. 21C**) abundance remained unaltered in comparison to their corresponding control cohorts. However, they show an increment by trend, which is not statistically significant ($n=4-7$, $P > 0.05$). Collectively, these findings support that CUL7 acts as an important component in IRS-1 mediated tyrosine kinase receptor signalling, leading to significant upregulation of phospho-AKT.

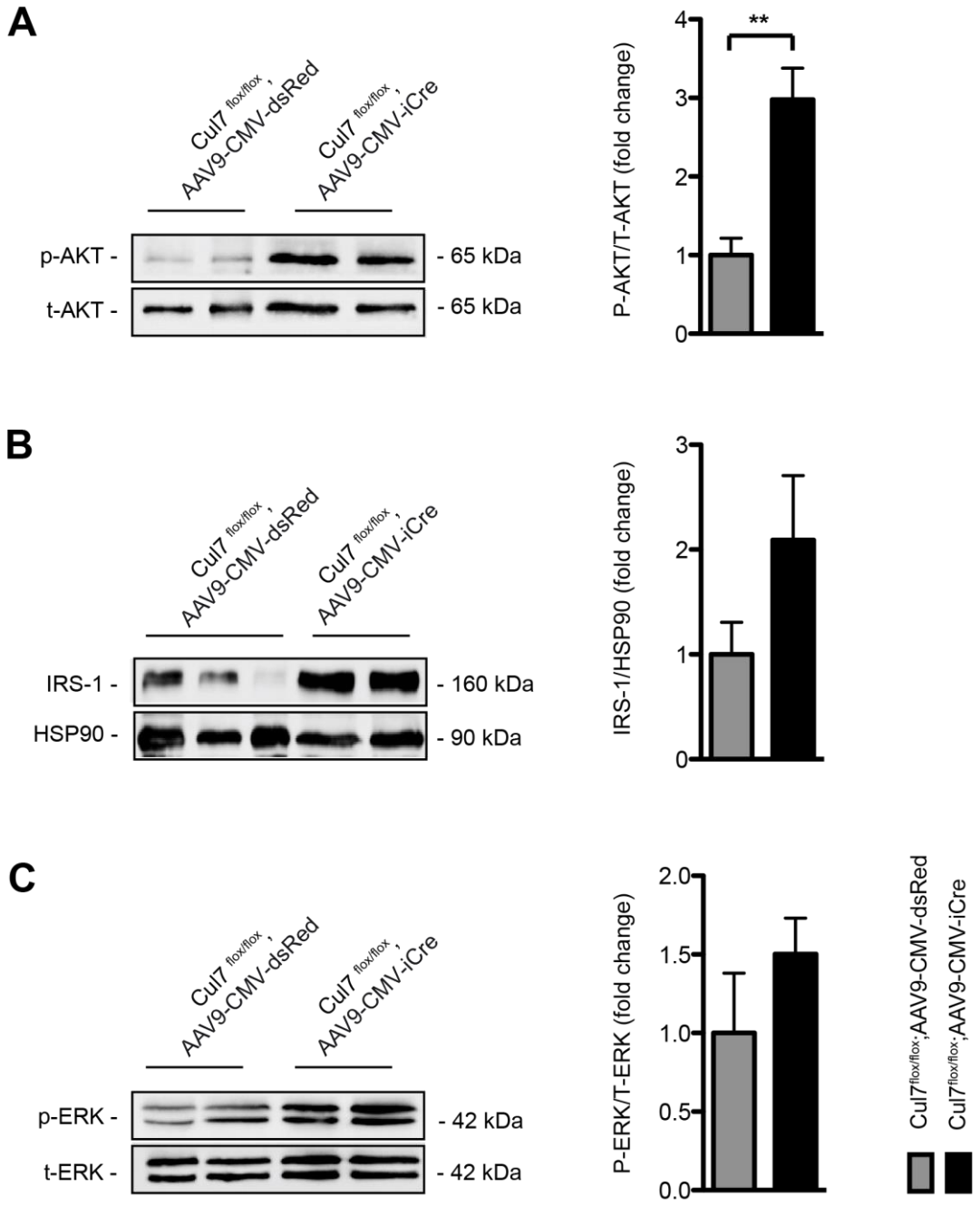

Figure 21: Increase of AKT-signalling due to cardiomyocyte-specific depletion of CUL7. Mice were sacrificed at an age of 8 weeks and protein levels were assessed in AMCMs under basal conditions via immunoblot. Data are shown as fold change normalized to respective Cul7$^{flox/flox}$;AAV9-CMV-dsRed control animals. (A) Representative Western blot for p-AKT abundance relative to t-AKT (left) and quantification of results (right). (B) Representative immunoblot depicted for IRS-1 relative to HSP90 (left) and quantitative data of obtained results (right). (C) Representative immunoblot directed against ERK protein expression (left) with the corresponding quantification of p-ERK/t-ERK ratio (right). n=4-7 mice/group; ** P < 0.01 (student's t-test).

7.3.2 *Tgf-β* downregulation in the whole heart under increment of afterload

By qRT-PCR, different key driving forces of cardiac tissue repair were studied such as transforming growth factor β (TGF-β) and members of the extracellular matrix-associated proteins (CCN proteins) to further understand the amelioration of cardiac remodelling in Cul7 deficient mice. For this purpose, mRNA expression levels of *Tgf-β*, *Ccn1* and *Ccn2*, of the matrix metalloproteases *Mmp2*, *Mmp3* and *Mmp9* as well as the *platelet-derived growth factor-AA (Pdgf-AA*) and *Timp-1* were measured in whole heart samples and compared to respective AAV9-CMV-dsRed control animals (Gourdie, Dimmeler et al. 2016). Cul7 deficient mice suffering from sustained pressure overload displayed a diminution by 68.0 ± 0.2 % of *Tgf-β* mRNA abundance when normalized to *Tgf-β* mRNA levels of $Cul7^{flox/flox}$;AAV9-CMV-dsRed controls (n=5-6, $P < 0.05$). As depicted in **Fig. 22,** expression levels of all other screening-targets were found to be unaltered (n=3-6, $P > 0.05$). Thus, lower *Tgf-β* expression as consequence of CUL7 ablation possibly leads to less fibrogenesis in the diseased heart.

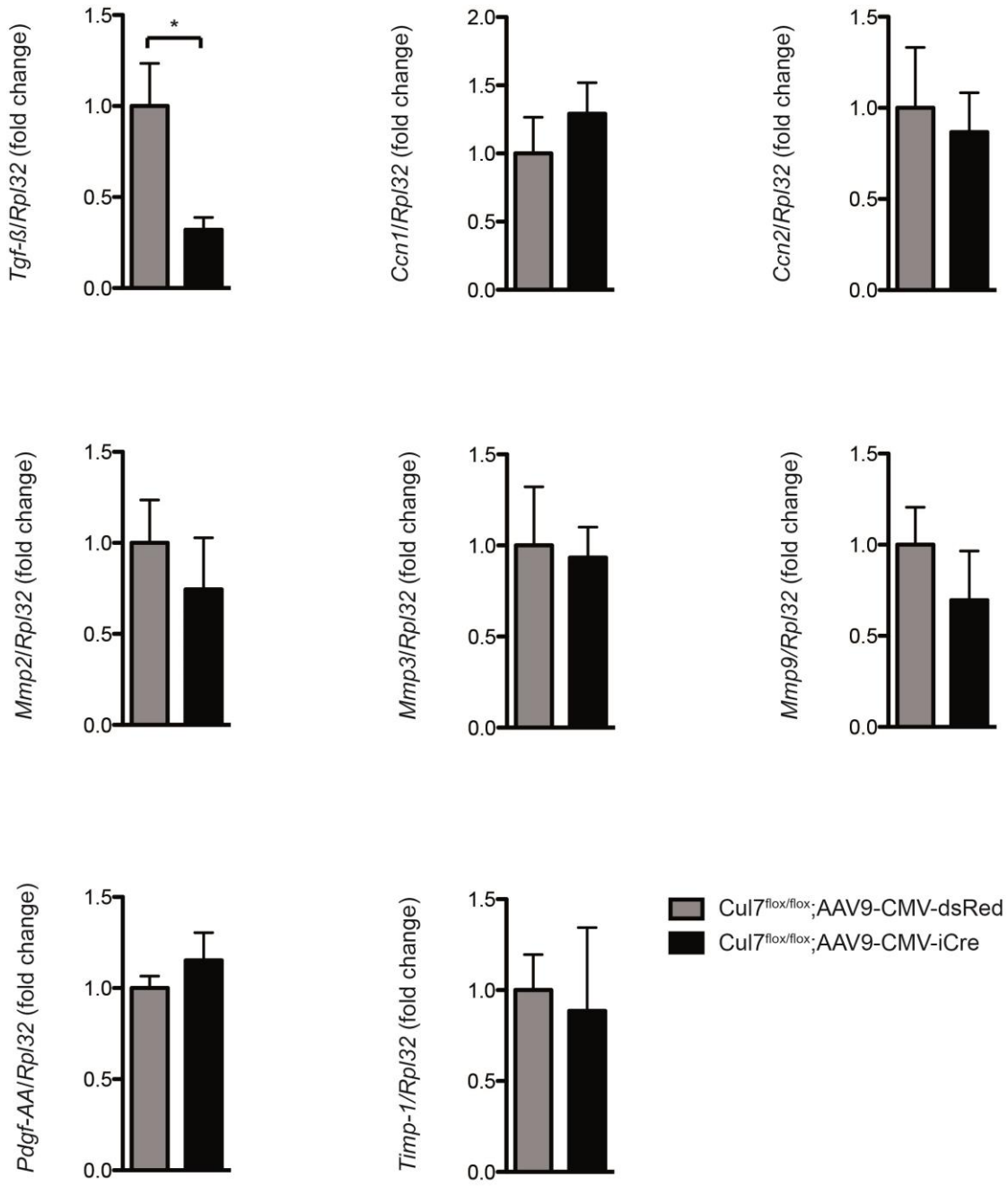

Figure 22: Screening of different key contributors to cardiac fibrosis. Mice undergoing 3 weeks of increment of afterload by TAC were sacrificed at an age of 12 weeks and measurement of mRNA abundance of *Tgf-β*, *Ccn1*, *Ccn2*, *Mmp2*, *Mmp3*, *Mmp9*, *Pdgf-AA* and *Timp-1* was performed in whole heart samples by qRT-PCR analysis. Data are shown as fold change normalized to respective Cul7$^{flox/flox}$;AAV9-CMV-dsRed control animals. n=3-6 mice/group, * $P < 0.05$ (student's t-test).

7.3.3 Decrease of apoptotic cardiomyocytes in the diseased heart

Apoptosis constitutes another important factor influencing cardiac remodelling under adverse cardiac conditions, meaning the replacement of dead cardiomyocytes due to pressure overload, by collagens to rescue heart function and cardiac output. Earlier, it has been reported

that PI3K signalling and its downstream target AKT promote cell survival by phosphorylating and thus inhibiting Bad being a proapoptotic factor (Franke and Cantley 1997). Nevertheless, this was just one of the first explored pathways where AKT mediates cell survival. Hence, in this thesis, apoptosis was assessed via TUNEL staining in heart sections obtained from mice being subjected to increment of afterload for 3 weeks. Since TAC is a disease model not inducing immediate and acute cell death but rather initially shear stress and cardiomyocyte hypertrophy, rates of apoptotic cells are commonly very low. Without disease stimuli, they account about 0.5 % in sham-operated mice (**Fig. 23**). However, 3 weeks of cardiac stress resulted in reduced cardiac apoptosis in Cullin7 deficient mice (0.598 ± 0.3 % apoptotic cells, n=5), which is similar to rates of apoptosis in the Cul7$^{flox/flox}$;AAV9-CMV-iCre sham cohort (0.551 ± 0.1 % apoptotic cells, n=4, P > 0.05). Moreover, a significant difference of cardiomyocyte cell death was shown when comparing both control sham and TAC cohorts reflecting a clear induction of apoptosis by TAC (Cul7$^{flox/flox}$;Lactate, sham: 0.7 ± 0.1 % vs. Cul7$^{flox/flox}$;Lactate, TAC: 1.1 ± 0.1 %, n=5, P < 0.05 and Cul7$^{flox/flox}$;AAV9-CMV-dsRed, sham: 0.7 ± 0.3 % vs. Cul7$^{flox/flox}$;AAV9-CMV-dsRed, TAC: 2.7 ± 0.3 %, n=3, P < 0 .001). This could not be observed in knockout mice, possibly leading to less replacement of dead cells with fibrous connective tissue. Nevertheless, the greater amount of apoptotic cells of the AAV9-CMV-dsRed TAC group is conspicuous when compared to the Cul7$^{flox/flox}$;Lactate TAC cohort, especially regarding the susceptibility of dsRed for aggregation and subsequent cytotoxicity (Zhou, Lin et al. 2011). To evaluate if these results constitute a viral effect or are even obtained from AAV9-CMV-dsRed being a toxic agent and leading to highly increased percentages of apoptotic cardiomyocytes, non-transgenic C57BL/6 wildtype mice were injected with lactated Ringer's solution as well as both viruses. Subsequently, a descriptive TAC-study was performed to reevaluate the observed results.

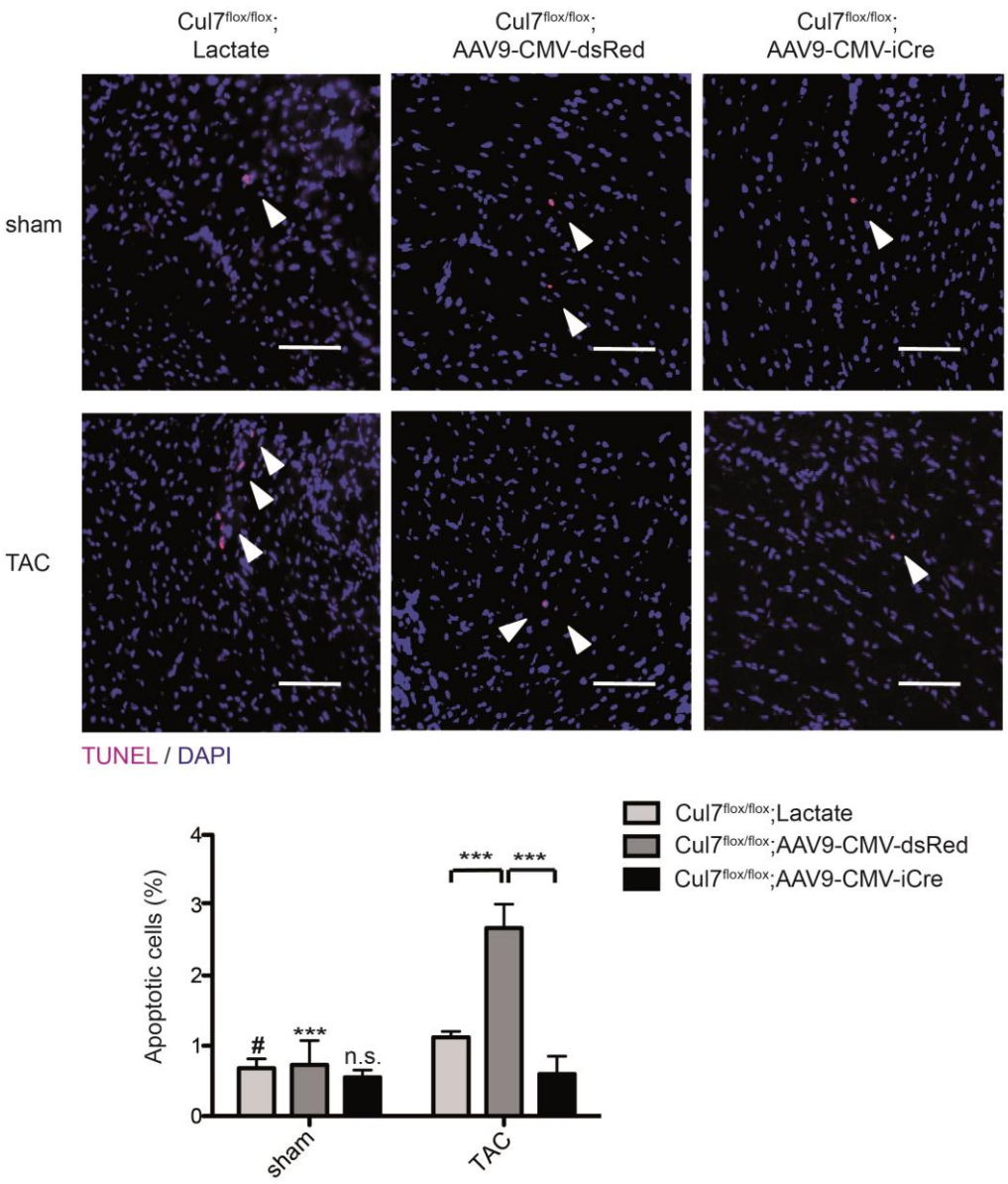

Figure 23: Reduced abundance of apoptotic cardiomyocytes under conditions of increased afterload. Representative myocardial sections stained with TUNEL (red) and DAPI (blue) as counterstaining of sham- (upper panel) and TAC-operated mice (lower panel). Quantification displayed down below as percentage of apoptotic cells to total cardiomyocyte count. Cells were analysed by pixel counting on digitized images in an automated manner. n=3-5 mice/group; n.s. not significant; # $P < 0.05$ (student's t-test), *** $P < 0.001$ (two-way ANOVA + Bonferroni post-test); scale bar = 100 µm.

7.3.4 Assessment of apoptosis in non-transgenic mice

To evaluate the influence of delivery and biodistribution of AAV9-CMV-dsRed in non-transgenic mice, neonatal mice were injected on day 4-5 after birth with lactated Ringer's solution as well as both viruses. They underwent the same operation protocol as the transgenic

mice cohort (see 7.2). At an age of 9 weeks, sham and transverse aortic constriction surgery were performed followed by euthanasia at an age of 12 weeks for further analysis of rates of apoptotic cardiomyocytes. By assessment of heart weight/body weight- (**Fig. 24A**), heart weight/tibia length- (**Fig. 24B**) and lung weight/tibia length-ratio (**Fig. 24C**), it was determined if transverse aortic constriction surgery was successfully performed. As depicted in **Fig. 24**, for all measurements, high statistical significance between all TAC animals and their respective sham-operated controls could be reached, whereas no difference between the different experimental groups of both cohorts was detectable (n=2-6, sham vs. TAC: $P < 0.001$). This further underlines the success of the surgery and a non-harming effect of viral injection on cardiac morphology and physical health of mice.

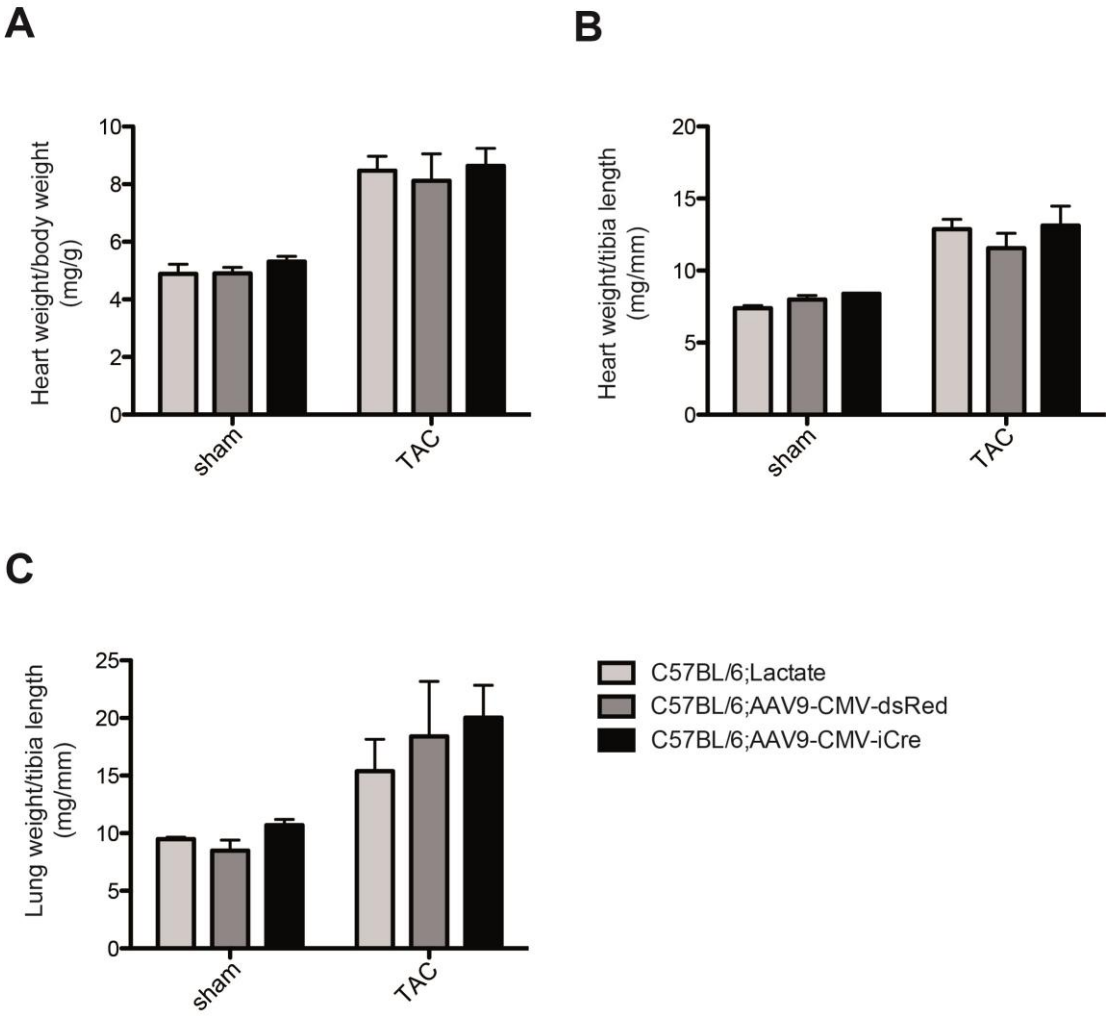

Figure 24: Cardiac phenotyping after sham and transverse aortic constriction surgery in wildtype mice. (A) Heart weight/body weight-, (B) heart weight/tibia length- and (C) lung weight/tibia length-ratios were assessed after 3 weeks of increment of afterload. n=2-6 mice/group. Sham vs. TAC (A-C): *** $P < 0.001$ (two-way ANOVA + Bonferroni post-test).

To clarify whether AAV9-CMV-dsRed injection in neonates leads to more severe cardiomyocyte loss under conditions of cardiac stress because of a cytotoxic potential of the red fluorescent protein dsRed (Strack, Strongin et al. 2008), heart sections from non-transgenic mice were obtained after 3 weeks of increment of afterload and subjected to TUNEL staining (**Fig. 25**). Interestingly, under conditions of increased afterload, C57BL/6;AAV9-CMV-dsRed as well as C57BL/6;AAV9-CMV-iCre mice displayed a higher abundance of apoptotic cardiomyocytes when compared to the C57BL/6;Lactate TAC cohort (C57BL/6;Lactate: 1.3 ± 0.2 % vs. C57BL/6;AAV9-CMV-dsRed: 1.9 ± 0.4 % vs. C57BL/6;AAV9-CMV-iCre: 1.9 ± 0.5 %, n=4-5, $P > 0.05$). In both viral groups, the ratio of TUNEL-positive cardiomyocytes to total cardiomyocytes was statistically not significantly higher when compared to lactate treated animals. This indicates a non-toxic effect of AAV9-CMV-dsRed in this study but rather a mild malign impact of intrapericardial application of adeno-associated viruses in neonates, leading to reduced cell survival under cardiac stress situations such as pressure overload. However, delivery of AAV9-CMV-iCre in transgenic mice led to reduced cardiac apoptosis, further emphasizing the beneficial effect of CUL7 depletion in the heart which balances the feasible pro-apoptotic effect of AAV9 application in this early stage of physical development of mice.

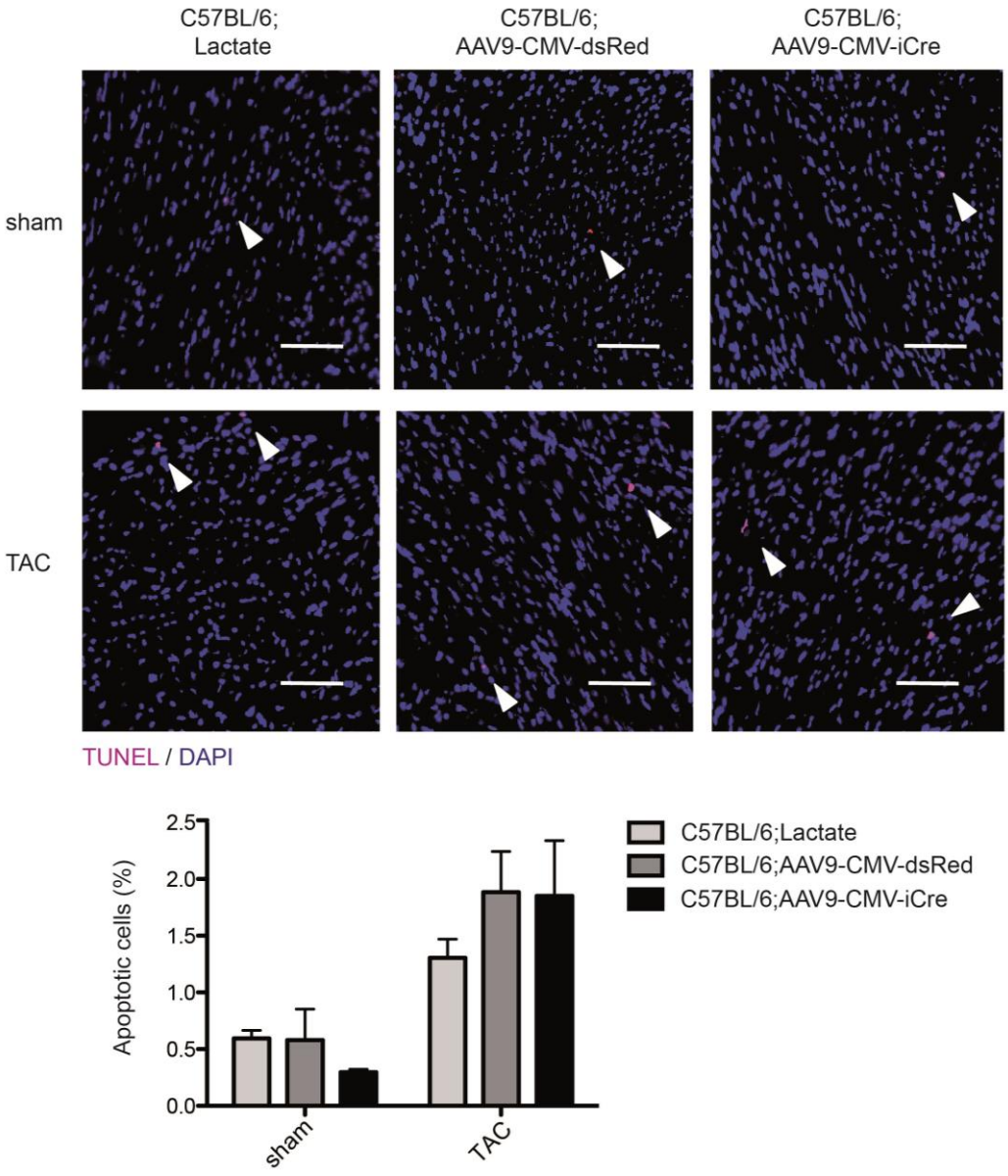

Figure 25: Detection of loss of cardiomyocytes by apoptosis in wildtype mice after 3 weeks of increment of afterload. Representative myocardial sections were taken from hearts of wildtype mice displaying TUNEL-positive cardiomyocytes for the sham cohort (upper panel) and its corresponding TAC group (lower panel). Quantification as shown down below as percentage of TUNEL-positive cardiomyocytes (red) overlaying DAPI (blue) positive nuclei as counterstaining. Cells were analysed by pixel counting on digitized images in an automated manner. n=2-5 mice/group. Sham vs. TAC: *** $P < 0.001$ (two-way ANOVA + Bonferroni post-test); scale bar = 100 µm.

8 DISCUSSION

In recent years, accumulating evidence has suggested a critical role of the UPS in the regulation of signalling pathways in the heart (Tham, Bernardo et al. 2015). In addition, it has been shown that it is involved in cardiac remodelling, e.g. in the context of cardiomyocyte apoptosis as well as cell mass and hypertrophy of the heart (Barac, Emrich et al. 2017).

In this dissertation, I provide comprehensive evidence for an essential role of the ubiquitin ligase component Cul7 in cardiac remodelling and myocardial fibrosis. I show that CM-specific downregulation of Cul7 results in reduced interstitial fibrosis upon pressure overload and is accompanied by a significant reduction of myocardial cell apoptosis. In addition, targeted ablation of Cul7 in CM significantly downregulated mRNA levels of the fibrosis-modifying gene *tgfb1* under conditions of increased afterload. Furthermore, transgenic Cul7 deficient mice displayed an increased activation of the PI3K/AKT signalling pathway. In summary, these data indicate that Cul7 acts as a pro-fibrotic factor in the heart upon cardiac injury.

8.1 Sufficient downregulation of CUL7 via AAV9-mediated gene transfer

Cardiac gene transfer is a potentially useful strategy for treatments of cardiovascular diseases, with the number of clinical trials ongoing for transgene expression through adeno-associated viral vectors (AAVs) increasing tremendously over the past decade (Asokan, Schaffer et al. 2012, Herrmann and Grimm 2018). To date, they have been developed for treatments of numerous diseases e.g. for gene transduction in the lung (Kurosaki, Uchibori et al. 2017), the brain (Chow, Guzman et al. 2017) or in the liver (Meliani, Boisgerault et al. 2017). In contrast to adenoviruses, AAVs typically lead to lower immune and inflammatory response, are not cell cycle-dependent in terms of their capacity to infect quiescent and dividing cells, and show the ability to provide long-term gene expression, i.e. they are not silenced in transduced cells. Moreover, AAVs do not integrate into the host's genome (Luo, Luo et al. 2015, Ziegler, Ishikawa et al. 2018). However, drawbacks of AAV-mediated gene transfer are their relatively small insert capacity (approximately 5 kb) of coding sequences into the native vector as well as the recently detected presence of neutralizing antibodies in humans that are capable of blocking the vector transduction completely (Mingozzi, Anguela et al. 2013). As members of the *Parvoviridae* family which are DNA viruses, AAVs are non-enveloped viruses with an icosahedral capsid structure built from 3 capsid proteins named VP1, VP2 and VP3 arising from the *Cap* (Capsid) gene. Aside from the *Cap* region, the single-stranded DNA genome carries the *Rep* (Replication) sequence which is required for viral genome replication and packaging. Both, *Rep* and *Cap* have multiple open reading frames (ORFs) and are flanked by

palindromic inverted terminal repeat sequences (ITRs), which function as viral origins of replication required for encapsidation, too. Recombinant AAV (rAAV) vectors are created by the replacement of the wild type *Rep* and *Cap* genes with the expression cassette of interest between the two ITRs, being the only required elements in cis of the original AAV genome for gene expression purposes. Importantly, AAVs are dependent on co-infection with other viruses, mainly adenoviruses or herpesvirus, for replication. Therefore, for the production of transduction vectors, “helper” sequences derived from the adenovirus genome, like in this thesis pDP9rs, are required (Chiorini, Wiener et al. 1996, Fang, Lai et al. 2012, Greenberg 2017, McClements and MacLaren 2017, Naso, Tomkowicz et al. 2017).

To date, 13 distinct human AAV serotypes (AAV1 - AAV13) have been described whereby over 100 different kinds of AAVs have been isolated yet. This number is certainly likely to expand due to the key role of rAAVs in human gene therapy (Giacca 2007). Generally, inherent to their viral biology, host tropism differs among AAV species, but nevertheless, the molecular basis of the varied tissue-tropisms has not been fully elucidated yet. Whereas AAV1 - AAV6 serotype vectors infect tissue culture cells to variable grades of efficiency, AAV7 - AAV13 serotype vectors do not achieve a transduction in vitro. In contrast, these serotypes efficiently transduce various tissues and organs in vivo (Srivastava 2016). In the heart, Fang and colleagues revealed that AAV9 shows the strongest cardiac tropism under the main established serotypes of AAV e.g. AAV5 or AAV6. The highest level of cardiac gene expression was thereby achieved by intracoronary delivery of AAV9 prior to intravenous injection. Also, global gene transfer of AAV9 was discovered in the liver independent of the used type of injection method (Fang, Lai et al. 2012).

Apart from the tissue tropism inherent to AAV vectors, the promoter used to drive transgene expression also plays an important role in tissue-specific transduction as well as its permanency. Therefore, different promoters have been described in AAV transduction and for most vectors, strong, constitutively active promoters are desired for high-level expression of the gene of interest. Frequently used promoters of this kind include the CMV (cytomegalovirus) promoter, the EF1a (elongation factor 1a), the SV40 (simian virus 40) and the CAG (CMV, chicken β-actin, rabbit β-globin) enhancer (Naso, Tomkowicz et al. 2017). Recently it was shown that application of AAV9, harbouring the CMV promoter, resulted in effective transgene expression in cardiomyocytes in a mouse model providing a tropic and global cardiac specificity of AAV9, which was confirmed by high DNA copy numbers. Nevertheless, lower expression levels were detected in the liver and other organs as well (Chen, He et al. 2015). In this regard, it has been demonstrated that the transduction of organs by AAV9 is age-dependent and can be reduced by injection of neonates. Therefore, new-born mice injected intra-arterially with AAV9 showed poor transduction of the liver, kidney, and aorta in comparison to adult mice, even independent of delivery routes (Bostick, Ghosh et al. 2007).

Summarizing, for optimal and highly efficient cardiac gene transfer via AAV9 with minimum off-tissue-targeting, injection of AAV9 into the pericardial space of neonates via a subxiphoid approach is an effective and fast method. Therefore, a vector dose of 2.5×10^{11}, which is resolved in 50 µl carrier solution, can be used. In the described experimental setting, AAV9-mediated gene transfer has a quick onset and is relatively stable for at least 1 year after intrapericardial injection (Bish, Morine et al. 2008). Moreover, transduction efficacy is dose-, as well as virus-dependent (Gruntman, Bish et al. 2013). This is the reason why in this thesis, 5×10^{11} genome copies of AAV9, dissolved in 50 µl lactated Ringer's solution, were injected in the pericardial sack of each male litter to obtain optimal results with a limited number of vector genomes reaching other organs.

In the present study, the mediated gene editing is based on overexpression of a Cre recombinase via cardiac-specific gene transfer through AAV9 under the control of a CMV-enhancer in transgenic homozygous floxed male neonates. As controls, male littermates injected with AAV9-CMV-dsRed and lactated Ringer's solution, being the control for the viral infection, were examined. By means of this method, a stable depletion of *Cul7* mRNA abundance of approximately 60 % could be observed in whole heart samples as well as in isolated cardiac myocytes, analysed in 8 week old mice under basal conditions. Since cardiomyocytes occupy approximately 80 % of cardiac tissue volume, the findings of the whole heart samples are consistent with the observations that were made in the isolated cell fraction (Vliegen, van der Laarse et al. 1991). Remarkably, cardiac fibroblasts were not targeted and AAV9-CMV-dsRed application did not affect the protein expression level of Cullin7. Moreover, in isolated cardiomyocytes, protein levels were markedly reduced by 80 %, which is in concordance with other studies using the same knockout strategy (Ramanujam, Sassi et al. 2016). Regarding the morphological assessment of the physical health of AAV9-injected mice, they did not show any pathological alterations in the analysed morphometric parameters at the time of dissection (weights of heart, lung, bodyweight and tibia length) reflecting the results from other studies using the AAV9 injection method. In this context, the investigators also do not observe any adverse effects that were associated with the AAV9 delivery system (Werfel, Jungmann et al. 2014, Kreusser, Lehmann et al. 2016). Furthermore, this is in agreement with previous findings indicating a very mild immune response to systemic AAV application in mice, which is only limited to several hours post-injection and does not lead to a decline of the physical state (Zaiss, Liu et al. 2002).

Strikingly, mice injected with AAV9-CMV-dsRed displayed a moderate diminution of heart weight/body weight- as well as heart weight/tibia length-ratio in comparison to the respective CUL7 depleted animal group. Moreover, no significant alteration in cardiac function between the experimental groups was detectable, but yet an improvement by trend in EF as well as in FS of $Cul7^{flox/flox}$;AAV9-CMV-iCre mice when compared to the control cohort, foremost aged 4

and 8 weeks. This was accompanied by not statistically significant decreased values of LVID $_{d/s}$ and left ventricular volumes $_{d/s}$. These findings might reflect the moderate increment of morphologic parameters like heart weight/tibia length-ratio indicating that Cul7 deficient mice show mild cardiac hypertrophy and subsequently an improved pump function due to an increase of muscle strength and ventricular mass, resulting in moderate reduced systolic and diastolic volumes as well as diameter parameters. However, these observations could not be confirmed by the assessment of cardiomyocyte size via WGA-based quantification, as we only observed a trend towards an increased cross-sectional area. In addition, for the measurement of cardiac fibrosis in *Cul7*$^{-/-}$ mice, a statistically non-significant amelioration was observable.

Moreover, as described above, AAV9 vectors display a systemic, multiorgan transduction profile following intravenous or pericardial administration presenting a substantial, albeit relatively lower expression level than in the heart (Bish, Morine et al. 2008, Zincarelli, Soltys et al. 2008). Also in this study, transduction of the virus was detected in several organs, e.g. the liver, the lung, the spleen and the kidney which was, however, not statistically significant by virtue of great variances of the knockdown efficiency in these organs. This may further accentuate the heart as well as the cardiomyocyte tropism of AAV9, meaning that AAV9 application is not able to induce a stable and enduring depletion of CUL7 in types of tissue other than the myocardium. Additionally, no morphological changes in these organs could be observed, concluding that the AAV9 approach is a suitable tool for investigation of Cul7 ablation in CM in vivo, with, however, minor extracardiac effects not being completely excluded. Nevertheless, further optimization of AAV9-derived vectors for tissue-detargeting is required. Therefore, a change of amino acid residues at different positions or a combination with point mutations onto AAV9 vector templates could lead to selectively ablated tissue tropism (Pulicherla, Shen et al. 2011). To further improve cardiospecifity of AAV9, transcriptional targeting elements such as microRNA-122 target sequences (Geisler, Jungmann et al. 2011), cardiac-specific promoters (Pacak, Sakai et al. 2008) or diminution of the CRISPR/Cas9 gene editing system to enable its packaging into AAV capsids (French and Annex 2014), would allow selective delivery of therapeutic transgenes to the heart by AAV9-mediated gene editing.

Previously, it was demonstrated in vitro that the cytotoxicity of DsRed and DsRed-Express2 is correlated with the downregulation of Bcl-xL, which is actually acting as an anti-apoptotic agent (Strack, Keenan et al. 2011, Zhou, Lin et al. 2011). Thus, it has been investigated whether the results in this thesis constitute an effect of viral application or if they are even obtained from AAV9-CMV-dsRed itself, leading to highly increased percentages of apoptotic cardiomyocytes. Therefore, non-transgenic C57BL/6 wildtype mice were injected with lactated Ringer's solution as well as both the viruses and underwent the same experimental protocol to perform a descriptive TAC study. Interestingly, the ratio of TUNEL-positive cardiomyocytes to total

cardiomyocyte count was statistically not significantly higher in the non-transgenic AAV9-CMV-dsRed-TAC group when compared to both other experimental cohorts, suggesting a non-toxic effect of its application in this study. Furthermore, several studies demonstrate that systemic AAV9 administration in mice has no influence on physical health and common biomarkers of cardiac and renal function as well as liver injury at different time points after application. Thus, only statistically non-significant changes were detected in plasma levels of lactate dehydrogenase (LDH) and creatine kinase (CK) revealing cardiac damage, aspartate aminotransferase (AST) and alanine aminotransferase (ALT) indicating liver injury and creatinine and blood urea nitrogen (BUN) pointing out kidney toxicity when compared to normal saline-treated controls animals. These data suggest that the AAV9-mediated transgene expression did not cause noticeable organ damage. Moreover, when assessing rates of apoptosis no impact on the number of TUNEL-positive cardiomyocytes and hepatocytes was observed when compared to non-transduced cells (Werfel, Jungmann et al. 2014, Chen, He et al. 2015, Chen, Zhai et al. 2017). Nevertheless, the reduced abundance of apoptotic CM after delivery of AAV9-CMV-iCre in transgenic mice must be underlined emphasizing the beneficial effect of CUL7 depletion in the heart, hence balancing a feasible pro-apoptotic effect of adeno-associated virus application.

8.2 Restraint of myocardial fibrosis upon cardiomyocyte-specific inactivation of CRL7

Cullin7 depletion does not improve heart function after transverse aortic constriction.

The effect of pressure overload was investigated in Cullin7 deficient mice by transverse aortic constriction as initially described by Rockmann et al. in 1991 (Rockman, Ross et al. 1991). Mimicking human hypertensive disease, TAC initially leads to a compensatory phase of heart hypertrophy, which is often associated with a temporary enhancement of cardiac contractility (Gomes, Falcão-Pires et al. 2013). After this initial compensatory phase, the response to the chronic hemodynamic overload becomes maladaptive and harmful, resulting in cardiac dilatation and heart failure (deAlmeida, van Oort et al. 2010). Before using the TAC model, we confirmed Cul7 expression levels by quantitative reverse transcription-PCR. We observed a downregulation by 60 % for *Cul7* mRNA abundance within the sham group and 50 % within the TAC cohort when compared to their respective AAV9-CMV-dsRed injected littermates. This is in alignment with other studies indicating that CUL7 abundance is upregulated by trend for 1.2-1.4-fold in the diseased heart in comparison to respective sham animals (Scheufele 2018).

Taken together, these findings may possibly emphasize the increased abundance of *Cul7* mRNA in the Cul7$^{flox/flox}$;AAV9-CMV-iCre TAC group, revealing a yet not examined forced expression of Cullin7 in chronic cardiac disease. Furthermore, to corroborate the operation sufficiency apparent in parameters of cardiac morphology, the heart weight/body weight-, heart weight/tibia length- and lung weight/ tibia length-ratios were calculated. In this regard, a statistically significant difference between the sham and the respective TAC groups could be observed. For instance, the heart weight/body weight-ratios in the TAC groups had a significant 1.4-1.7-fold increase due to greater heart weight in concordance with a significant 1.5-1.7-fold increment of the heart weight/tibia length-ratios, underlining the subsequent hypertrophic response after ligation of the aortic arch.

Surprisingly, the increment of afterload by TAC led to a global heart insufficiency within the lactate treated cohort which is reflected in all obtained values after TAC surgery. After 3 weeks of chronic hemodynamic overload, the mice which had received lactated Ringer's solution displayed a stronger dilation of the left ventricle, alongside with a statistically significant depression of cardiac function, evidenced by the reduction of FS and EF when compared to both other cohorts. These findings were further underlined by their morphological appearance, indicating severely higher weights of the lung as well as the heart. Since this thesis was performed as a double-blind study and there is no evidence in the literature indicating neither a beneficial effect of viral injection in the heart and other tissues nor a harmful consequence of lactated Ringer's solution on heart function, the cardiac decompensation in Cul7$^{flox/flox}$;Lactate mice was conceivably an unlucky event perchance leading to rigorously backward heart failure in comparison to both other experimental groups.

Ablation of CUL7 under conditions of increased afterload was not sufficient enough to induce an improvement of heart function or rather an amelioration of cardiac dysfunction when comparing Cul7 deficient mice to their corresponding AAV9-CMV-dsRed control cohort, which is in line with the observations under basal conditions. In summary, ablation of CUL7 had no effect on cardiac output under conditions of increased afterload as well as under basal conditions.

Amelioration of interstitial cardiac fibrosis upon pressure overload.

To further examine the impact of pressure overload in mice ablated from CUL7, cardiac sections of all examined experimental groups were stained with WGA to examine left ventricular hypertrophy. Within the mice subjected to increment of afterload, there was no significant alteration in cross-sectional area detectable for the 3 different genotypes, whereas a statistically significant difference could be observed between the respective sham and TAC cohorts. These data are contrasting to the findings of Nakajima et al., who observed a great

reduction of hypertrophic cardiomyocyte cell growth in response to myocardial infarction in mice expressing a Cul7 dominant-negative interfering transgene (Nakajima, Nakajima et al. 2004). In this study, no changes in cardiomyocyte hypertrophy could be detected neither under basal conditions nor under longstanding pressure overload. The different results of both studies in terms of the development of cardiac hypertrophy might be related to different experimental periods as well as to the used models to induce cardiac stress. Generally, the heart responds to sustained insults such as ischemia and pressure overload with a dynamic remodelling process that finally leads to heart failure. However, progression to heart failure, using for example TAC, is variable and depends on the severity and duration of the constriction, as well as other factors such as mouse strain, age, and location of the band (Mohammed, Storlie et al. 2012). Chronic hypertension leads to progressive myocardial hypertrophy, interstitial fibrosis, increased left ventricular stiffness, as well as low cardiac output (Gradman and Alfayoumi 2006). In contrast, following myocardial infarction, the loss of viable myocytes leads amongst other things to the degradation of collagen and other extracellular matrix modifications. Subsequently, the infarcted area is thinned, followed by reactive hypertrophy and fibrosis of the non-infarcted myocardium. In turn, this leads to impaired systolic function (Jugdutt 2003, Ertl and Frantz 2005, Weinheimer, Lai et al. 2015). In summary, the reasons for the obtained different results of both studies remain to be elucidated but might be explained by the different characteristics and activated downstream signalling pathways upon TAC and MI as well as by the usage of an AAV-knockout approach in comparison to a dominant-negative interfering transgene expression.

Nevertheless, a noticeable reduction of cardiac interstitial fibrosis could be observed in myocardial sections upon pressure overload for 3 weeks. Remarkably, fibrogenesis was reduced by approx. 50 % in the TAC cohort in CUL7 deficient mice in comparison to the respective AAV9-CMV-dsRed littermates. In addition, no significant difference between the sham and the TAC cohort of mice being delivered with AAV9-CMV-iCre was detectable, while in both other experimental cohorts a 5-6-fold increase was observed concerning the fibrotic response upon TAC surgery. These findings are in concordance with previous studies of the role of Cullin7 in the heart, which demonstrated decrement of fibrotic scar formation and preservation of cardiac function after myocardial infarction. However, the latter contrasts with the findings of this study presumably due to the different stimuli of cardiac injury (TAC vs. MI) (Hassink, Nakajima et al. 2009). Interestingly, a previous study reported a pro-fibrotic role of Cul7 in patients having a 6p21.1 amplification, representing the human Cul7 gene locus, suffering from metabolic syndrome-associated hepatocellular carcinoma. Peri-tumoral liver areas were strongly correlated with advanced fibrosis and elevated CUL7 protein concentrations in these patients (Paradis, Albuquerque et al. 2013). In addition, it has been found that Cul7 downregulation in HCC cells inhibited epithelial-mesenchymal transition

(EMT). This is a process, during which the adhesion of epithelial cells and matrix to the surrounding cells is reduced. They get similar in morphology to fibroblasts, consequently acquiring an enhanced migration ability. Hence, EMT has been recognized to play fundamental roles in several processes during embryonic development, chronic inflammation and particularly during fibrogenesis (Asli and Harvey 2013, Zhang, Yang et al. 2016). Furthermore, an essential role for Cullin7 in diabetic cardiomyopathy (DCM) has been recently described. Myocardial fibrosis and collagen deposition are the main structural changes observed in DCM due to altered glucose uptake and metabolism. In this regard, the E3 ligase CUL7 degrades the insulin receptor substrates in an ubiquitin-proteasome-dependent way, which causes insulin resistance thereby leading to unfavorable cardiac fibrosis (Bai, Wang et al. 2016). These data suggest collectively that CRL7 generally regulates pro-fibrotic mechanisms that are effective in different organs and diseases. In summary, the alteration of CUL7 activity demonstrates its impact upon extensive deposition of extracellular matrix proteins and fibrosis, further underlining that inactivation of CUL7 has a marked effect on cardiac fibrogenesis and protects the heart from pathological fibrosis under conditions of increased afterload as well as after myocardial infarction.

8.3 Activation of pro-survival pathways following depletion of CUL7

Since cardiomyocytes have only a very limited proliferative capacity, an essential reparative mechanism to prevent cardiac rupture upon sustained pressure or myocardial infarction is replacement fibrosis and scar formation (Bradley, Spaletra et al. 2018). Consequently, cardiomyocyte replacement does not occur in the damaged heart which is typically characterized by loss of cardiomyocytes due to apoptosis, necrosis or phagocytosis, leading to compensatory growth of the remaining cardiac cells as well as reparative fibrosis. Thereby, a progressive deterioration of cardiac function is induced. Thus, a selection of critical pro-survival pathways has been investigated to study their role in Cul7-mediated fibrosis (Piek, de Boer et al. 2016).

Enhanced activation of PI3K/AKT signalling pathways in cardiac myocytes depleted of Cul7.

In this study, a 3-fold upregulation of p-AKT in isolated cardiomyocytes was observed when compared to the respective AAV9-CMV-dsRed control mice. Surprisingly, protein expression levels of IRS-1 and phosphorylation status of ERK1/2 remained unchanged in mice ablated of Cullin7. This is in concordance with findings indicating that the loss of the *Cul7* allele results in

hyperactivation of the PI3K/AKT signalling pathway upon insulin stimulation in skeletal muscle and plasma glucose clearance in vivo, revealing its fundamental role in the regulation for glucose homeostasis and energy metabolism (Scheufele, Wolf et al. 2014). In the heart, there is abundant evidence that activation of PI3K/AKT signalling has cardioprotective effects by regulating various cellular functions e.g. limiting apoptotic cell death in the myocardium (Yao, Han et al. 2014). It has been pointed out that embryonic stem cells and transplanted hearts showed a significant decrease of apoptosis upon doxorubicin-induced cardiomyopathy as a consequence of an upregulation of the AKT pathway. This led to reduced cardiac fibrosis, which was attributable to a downregulation of MMP-9 activity (Singla 2015). In addition, Xu and colleagues recently demonstrated a key role of p-AKT in the reduction of cardiac cell death following myocardial ischemia/reperfusion injury via Substance P in H9c2 cells (Xu, Gu et al. 2017). This was further evidenced via Ghrelin being able to reduce the hypoxia/reperfusion damage in neonatal rat cardiomyocytes by inhibiting apoptosis through activation of the AKT/mTOR signalling pathway (Wang, Lu et al. 2017). These data are additionally substantiated by Matsui et al. showing that adenoviral gene transfer of activated AKT protects cardiomyocytes from apoptosis in response to hypoxia in vitro (Matsui, Li et al. 1999) and diminishes cardiac cell death as well as fibrotic scar size following ligation of the left anterior descending coronary artery accompanied by restoration of cardiac function in vivo (Matsui, Tao et al. 2001).

In conclusion, AKT is an important functional modulator in cardiomyocytes, affecting cell survival and cardiac fibrogenesis and is, thus, crucial in modulating the outcome of ischaemic heart disease. Its ability to improve the stability of surviving cells is probably a contributing mechanism to the in vivo beneficial effects observed by Cul7 depletion. Nevertheless, other apoptosis-related signalling pathways may modulate also overall cardiac function in vivo by affecting both, cardiomyocyte death and the function of surviving cells. Hence, to further substantiate these findings, rates of cardiac apoptotic myocytes were assessed.

Reduction of myocardial cell apoptosis under conditions of increased afterload.

In TAC mice depleted of CUL7, apoptotic cells were diminished by approximately 81 % when compared to the respective AAV9-CMV-dsRed TAC cohort. Remarkably, no significant difference between the sham and the TAC knockout group could be observed. In line with this finding are the observations of Nakajima and colleagues, indicating that expression of a dominant-interfering mutant of Cul7 was associated with an induction of cardiomyocyte DNA synthesis and cell cycle re-entry in the interventricular septa as well as in the infarct border zone after MI. This was concomitant with a reduction in hypertrophic cardiomyocyte growth 4 weeks after permanent coronary artery occlusion. This suggests that cell cycle activation might

partially counteract the adverse ventricular remodelling that occurs after cardiac injury (Nakajima, Nakajima et al. 2004). Collectively, these data indicate that loss of Cul7, thereby inactivating CRL7 ubiquitin ligase function, results in reduced myocardial cell apoptosis under conditions of increased afterload which in turn reduces the need for hypertrophic growth and for replacing fibrosis, as evidenced in this thesis.

Reduced myocardial expression of *Tgf-β1* upon genetic ablation of Cul7.

In order to clarify the pro-fibrotic role of CRL7 under sustained pressure overload, different key contributors to cardiac fibrosis were screened via qPCR in whole heart samples. This preselection included *Tgf-β*, *Ccn1* and *Ccn2*, the matrix metalloproteases *Mmp2*, *Mmp3* and *Mmp9* as well as *Pdgf-AA* and *Timp-1* (Gourdie, Dimmeler et al. 2016). Noticeably, only *Tgf-β* showed a marked downregulation by approx. 60 % among the examined molecules in *Cul7*$^{-/-}$ TAC mice when compared to its respective dsRed TAC cohort. Previously, it has been demonstrated that TGF-β receptor and PI3K/AKT signalling pathways show various mechanisms of crosstalk. Technically, both pathways were initially thought to be linear signalling conduits thereby being involved in the control of numerous responses like proliferation, apoptosis, fibrosis and cell migration. Up to now, direct and indirect interplays between both pathways have been shown (Zhang, Zhou et al. 2013). Therefore, AKT interacts directly with unphosphorylated SMAD3, a key component of the TGF-β mediated downstream signalling and sequesters it outside the nucleus. This association between AKT and SMAD3 prevents TGF-β-mediated phosphorylation of SMAD3, which then impedes the formation of the SMAD3/SMAD4 heteromeric complex. Thus, AKT inhibits SMAD3-mediated transcription leading to downregulation of TGF-β/SMAD induced gene expression for apoptosis, fibrosis, and TGF-β expression. This is explained by TGF-β acting as an autocrine secreted molecule (Kim, Angel et al. 1990, Zhang, Zhou et al. 2013). Collectively, it should not be forgotten that the signalling cascade, as delineated in **Fig. 26**, is just one potential mechanism how the obtained results of this work could fit together. CUL7 ablation leads to less degradation of IRS-1, thus, downstream effector p-AKT is increased, leading to stronger inhibition of SMAD proteins and their colocalization to the nucleus. However, these pathways were not fully studied since SMAD3/4 expression levels were not investigated and IRS-1 protein level did not exhibit a statistically significant upregulation.

Moreover, Ding and co-workers revealed that TGF-β/SMAD4 signalling can restrict the tumorigenic effects of the PI3K/AKT pathway in prostate cancer. For this purpose, they generated phosphatase and tensin homologue (PTEN) deficient mice, which is a protein negatively regulating intracellular levels of PI3K/AKT signalling in cells thereby functioning as a tumour suppressor (Haddadi, Lin et al. 2018). Upon genetic deletion of SMAD4 in PTEN$^{-/-}$

mice, lethal and metastatic prostate cancer emerged with 100 % penetrance indicating that TGF-β/SMAD4 is a critical suppressor of tumour progression via PI3K/AKT (Ding, Wu C– et al. 2011). In conclusion, these signalling pathways influence each other on multiple layers demonstrating that more studies are needed to further understand the molecular mechanisms how CRL7 restrains cardiac fibrosis. Moreover, it has been suggested that CUL7 acts as a pro-apoptotic agent in a non-proteolytic manner due to its noncanonical BH3 region. This is a single sequence motif defining molecules that belong to the BCL-2 members, which is a group of proteins that regulate programmed cell death and e.g. mitochondrial physiology (Aouacheria, Combet et al. 2015). It was shown that overexpression of CUL7 in NIH-3T3 cells promoted apoptosis in a manner that was dependent on the integrity of the BH3 domain. In addition, deletion of the BH3 motif abolished apoptosis activity of Cullin7, which is independent of p53 expression as a proteolytic target of CRL7 (Tsai, Pasumarthi et al. 2000).

Surprisingly, all other investigated targets remained to be unaltered albeit most of them intercommunicate with TGF-β mediated signalling pathways, since TGF- β plays a key role as fibrogenic cytokine of the ECM. Stimulation of TGF-β induces the transformation of fibroblasts to myofibroblasts (Sappino, Schurch et al. 1990), which express and secrete much higher levels of ECM proteins, enhances excessive production of ECM and restrains its degradation (Meng, Nikolic-Paterson et al. 2016), mediated by inhibition of MMPs and synthesis of protease inhibitors, especially TIMPs (Segura, Frazier et al. 2014). TIMPs are also secreted by myofibroblasts with TIMP-1 being the major cardiac TIMP strongly induced in the failing heart (Lindsey, Yabluchanskiy et al. 2015). Furthermore, 2 members of the CCN family, which is a group of 6 genes encoding for yet related cysteine-rich proteins, have been investigated. This family includes cysteine-rich 61 (Cyr-61/CCN1), connective tissue growth factor (CTGF/CCN2), the both being examined in this study, as well as nephroblastoma over-expressed gene (Nov/CCN3), CCN4 (WISP-1/Elm1), CCN5 (WISP-2/Rcop1) and CCN6 (WISP-3CCN) (Klenotic, Zhang et al. 2016). CCN1 is a secretory protein that is expressed at sites of wound healing to induce fibroblast senescence through activation of p53 and $p16^{INK4a}$ pathways. Recently, it was demonstrated that induction of the cellular senescence program in cardiofibroblasts by cardiotropic expression of the matricellular protein CCN1 via AAV9 had cardioprotective effects and led to reduced fibrosis and improved cardiac function after TAC (Meyer, Hodwin et al. 2016). Thereby, senescent cells are not simply cell cycle-arrested cells; they also affect bystander cells through the secretion of bioactive molecules, termed the senescence-associated secretory phenotype (SASP), thus influencing surrounding interstitial cells, like fibroblasts by induction of senescence in a paracrine manner as it was shown for the lung (Kadota, Fujita et al. 2017) and the liver (Salama, Sadaie et al. 2014). Thus, it is tempting to speculate that the reduction of cardiac fibrosis observed in $Cul7^{flox/flox}$;AAV9-CMV-iCre mice after 3 weeks of pressure overload could have been mediated by induction of a senescent

phenotype in the heart independent of TGF-β and AKT. For CCN2, there are some studies demonstrating that this protein is enhanced in cardiovascular diseases e.g. under conditions of increased afterload. Herein, it was shown that antagonizing the function of CTGF with a monoclonal antibody protects mice from TAC-induced left ventricular remodelling and dysfunction. Thus, *CTGF*$^{-/-}$ mice revealed less cardiac hypertrophy and lower collagen formation due to less activation of genes regulating ECM production in response to sustained pressure overload (Szabo, Magga et al. 2014). Moreover, CTGF was induced by TGF-β in cardiac fibroblasts and myocytes, thereby mediating AngII induced heart failure and upregulation of CTGF-stimulated fibroblast proliferation in vitro (Ahmed, Oie et al. 2004). However, despite the described interactions between TGF-β and these mediators of cardiac fibrosis, in this study, their mRNA expression levels remained remarkably unaltered in the challenged heart. Clearly, more investigations and studies are needed to further dissect the mechanism between the observed alterations of signalling pathways and the anti-fibrotic phenotype. Thus, it awaits upcoming research whether pharmacological targeting of CRL7 is a useful strategy to restrain cardiac fibrosis.

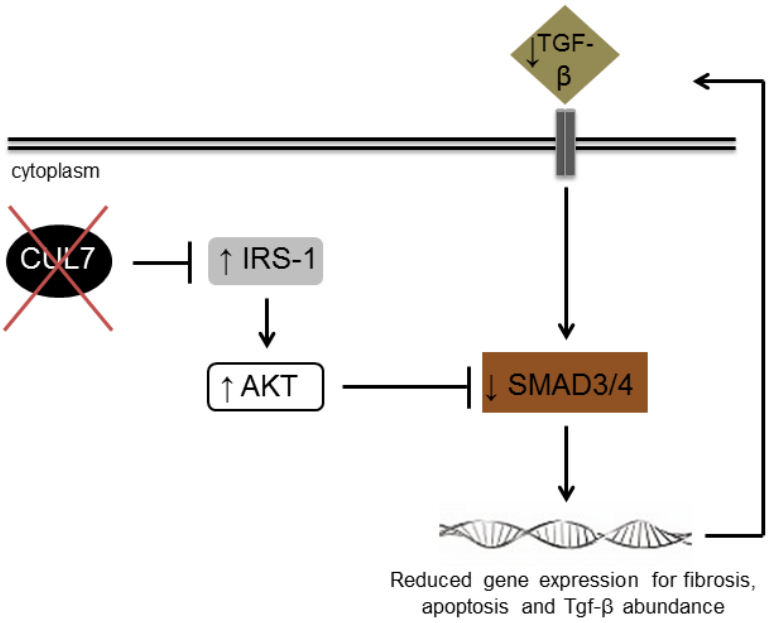

Figure 26: Likeable mechanism of the observed cardiac phenotype in aortic-banded Cullin7 deficient mice. CUL7 ablation leads to less degradation of IRS-1, a well-known substrate target of CRL7. Hence, downstream effector AKT is increased thereby leading to stronger inhibition of SMAD proteins and their colocalization to the nucleus. Finally, gene expression for fibrosis, apoptosis and TGF-β protein abundance, being an autocrine secreted molecule, is reduced.

9 ACKNOWLEDGEMENTS

Firstly, I would like to express my gratitude and special thanks to Prof. Dr. Dr. Stefan Engelhardt for providing me the opportunity to write this thesis at the Institute of Pharmacology and Toxicology (IPT) at the Technical University of Munich. As my first supervisor, I would like to thank him for every advice, his great support, constant supervision, and inspiring ideas leading to persistent progress of this work.

Moreover, I deeply want to thank my second supervisor and mentor Prof. Dr. Antonio Sarikas, for guiding me and for his tremendous encouragement and support in any scientific, methodical or even private question. Thank you for accompanying me during this dissertation and improving my research as well as for every advice, leading to further development of my scientific understanding and personality in the last years.

Equally important for me is to thank all lab members and former colleagues for supporting my work and encouraging me along this sometimes troublesome way. Building a great team, you always helped me and made things easier once a while. At this point, I would especially like to express my deepest gratitude to Kathleen Meyer being my mentor in mind and encouraging me every day, giving me strength and leading this project to success with her kindness and warm charisma. Also, I would like to profoundly thank Florian Scheufele and Deepak Ramanujam, supporting me in any scientific question and being such friendly and helpful persons.

Last but not least, I am truly grateful to have such a great family and friends who unlimitedly encouraged and supported me this way at any time point, without this work would have been impossible. Particularly, I want to thank Myrto Boukovala for her unlimited understanding on a very unique level, care, encouragement and deep friendship. Moreover, I want to express my deepest gratitude to my parents and to Christian being the best brother I can imagine. Finally, Michi, thank you for all your love, support and strength no matter what.

10 REFERENCES

Ahmed, M. S., E. Oie, L. E. Vinge, A. Yndestad, G. Oystein Andersen, Y. Andersson, T. Attramadal and H. Attramadal (2004). "Connective tissue growth factor--a novel mediator of angiotensin II-stimulated cardiac fibroblast activation in heart failure in rats." J Mol Cell Cardiol **36**(3): 393-404.

An, J., Z. Liu, Q. Liang, Y. Pan, H. Li, R. Wang and Y. Jin (2017). "Overexpression of Rabl3 and Cullin7 is associated with pathogenesis and poor prognosis in hepatocellular carcinoma." Hum Pathol **67**: 146-151.

Aouacheria, A., C. Combet, P. Tompa and J. M. Hardwick (2015). "Redefining the BH3 Death Domain as a 'Short Linear Motif'." Trends Biochem Sci **40**(12): 736-748.

Aoyagi, T. and T. Matsui (2011). "Phosphoinositide-3 kinase signaling in cardiac hypertrophy and heart failure." Curr Pharm Des **17**(18): 1818-1824.

Arai, T., J. S. Kasper, J. R. Skaar, S. H. Ali, C. Takahashi and J. A. DeCaprio (2003). "Targeted disruption of p185/Cul7 gene results in abnormal vascular morphogenesis." Proc Natl Acad Sci U S A **100**(17): 9855-9860.

Asli, N. S. and R. P. Harvey (2013). "Epithelial to mesenchymal transition as a portal to stem cell characters embedded in gene networks." Bioessays **35**(3): 191-200.

Asokan, A., D. V. Schaffer and R. Jude Samulski (2012). "The AAV Vector Toolkit: Poised at the Clinical Crossroads." Molecular Therapy **20**(4): 699-708.

Ayoub, K. F., N. V. K. Pothineni, J. Rutland, Z. Ding and J. L. Mehta (2017). "Immunity, Inflammation, and Oxidative Stress in Heart Failure: Emerging Molecular Targets." Cardiovasc Drugs Ther **31**(5-6): 593-608.

Azevedo, P. S., B. F. Polegato, M. F. Minicucci, S. A. Paiva and L. A. Zornoff (2016). "Cardiac Remodeling: Concepts, Clinical Impact, Pathophysiological Mechanisms and Pharmacologic Treatment." Arq Bras Cardiol **106**(1): 62-69.

Bai, T., F. Wang, N. Mellen, Y. Zheng and L. Cai (2016). "Diabetic cardiomyopathy: role of the E3 ubiquitin ligase." Am J Physiol Endocrinol Metab **310**(7): E473-483.

Barac, Y. D., F. Emrich, E. Krutzwakd-Josefson, S. Schrepfer, L. C. Sampaio, J. T. Willerson, R. C. Robbins, A. Ciechanover, F. W. Mohr, D. Aravot and D. A. Taylor (2017). "The ubiquitin-proteasome system: A potential therapeutic target for heart failure." J Heart Lung Transplant **36**(7): 708-714.

Bish, L. T., K. Morine, M. M. Sleeper, J. Sanmiguel, D. Wu, G. Gao, J. M. Wilson and H. L. Sweeney (2008). "Adeno-associated virus (AAV) serotype 9 provides global cardiac gene transfer superior to AAV1, AAV6, AAV7, and AAV8 in the mouse and rat." Hum Gene Ther **19**(12): 1359-1368.

Bloom DE, C. E., Jané-Llopis E, Abrahams-Gessel S, Bloom LR, Fathima S, Feigl AB, Gaziano T, Mowafi M, Pandya A, Prettner K, Rosenberg L, Seligman B, Stein AZ, Weinstein C. (2011). "The Global Economic Burden of Non-communicable Diseases." World Economic Forum.

Bostick, B., A. Ghosh, Y. Yue, C. Long and D. Duan (2007). "Systemic AAV-9 transduction in mice is influenced by animal age but not by the route of administration." Gene Ther **14**(22): 1605-1609.

Bradley, J. M., P. Spaletra, Z. Li, T. E. Sharp, 3rd, T. T. Goodchild, L. G. Corral, L. Fung, K. W. H. Chan, R. W. Sullivan, C. A. Swindlehurst and D. J. Lefer (2018). "A novel fibroblast activation inhibitor attenuates left ventricular remodeling and preserves cardiac function in heart failure." Am J Physiol Heart Circ Physiol **315**(3): H563-h570.

Brunt, E. M. (2013). "A novel genetic marker of liver disease aetiology in hepatocellular carcinoma: culling the metabolic syndrome." Gut **62**(6): 808-809.

Chen, B. D., C. H. He, X. C. Chen, S. Pan, F. Liu, X. Ma, X. M. Li, M. T. Gai, J. Tao, Y. T. Ma, Y. N. Yang and X. M. Gao (2015). "Targeting transgene to the heart and liver with AAV9 by different promoters." Clin Exp Pharmacol Physiol **42**(10): 1108-1117.

Chen, P. and G. D. Yao (2016). "The role of cullin proteins in gastric cancer." Tumour Biol **37**(1): 29-37.

Chen, Q., H. Zhai, X. Li, Y. Ma, B. Chen, F. Liu, H. Lai, J. Xie, C. He, J. Luo, J. Gao and Y. Yang (2017). "Recombinant adeno-associated virus serotype 9 in a mouse model of atherosclerosis: Determination of the optimal expression time in vivo." Mol Med Rep **15**(4): 2090-2096.

Chen, S., J. Wu, Y. Lu, Y. B. Ma, B. H. Lee, Z. Yu, Q. Ouyang, D. J. Finley, M. W. Kirschner and Y. Mao (2016). "Structural basis for dynamic regulation of the human 26S proteasome." Proc Natl Acad Sci U S A **113**(46): 12991-12996.

Chiorini, J. A., S. M. Wiener, L. Yang, R. H. Smith, B. Safer, N. P. Kilcoin, Y. Liu, E. Urcelay and R. M. Kotin (1996). The Roles of AAV Rep Proteins in Gene Expression and Targeted Integration. Adeno-Associated Virus (AAV) Vectors in Gene Therapy. K. I. Berns and C. Giraud. Berlin, Heidelberg, Springer Berlin Heidelberg**:** 25-33.

Chow, R. D., C. D. Guzman, G. Wang, F. Schmidt, M. W. Youngblood, L. Ye, Y. Errami, M. B. Dong, M. A. Martinez, S. Zhang, P. Renauer, K. Bilguvar, M. Gunel, P. A. Sharp, F. Zhang, R. J. Platt and S. Chen (2017). "AAV-mediated direct in vivo CRISPR screen identifies functional suppressors in glioblastoma." Nat Neurosci **20**(10): 1329-1341.

Ciechanover, A. (2015). "The unravelling of the ubiquitin system." Nat Rev Mol Cell Biol **16**(5): 322-324.

Collins, G. A. and A. L. Goldberg (2017). "The Logic of the 26S Proteasome." Cell **169**(5): 792-806.

deAlmeida, A. C., R. J. van Oort and X. H. Wehrens (2010). "Transverse aortic constriction in mice." J Vis Exp(38).

Deshaies, R. J. and C. A. Joazeiro (2009). "RING domain E3 ubiquitin ligases." Annu Rev Biochem **78**: 399-434.

Dias, D. C., G. Dolios, R. Wang and Z. Q. Pan (2002). "CUL7: A DOC domain-containing cullin selectively binds Skp1.Fbx29 to form an SCF-like complex." Proc Natl Acad Sci U S A **99**(26): 16601-16606.

Ding, Z., J. Wu C–, G. C. Chu, Y. Xiao, D. Ho, J. Zhang, S. R. Perry, E. S. Labrot, X. Wu, R. Lis, Y. Hoshida, D. Hiller, B. Hu, S. Jiang, H. Zheng, A. H. Stegh, K. L. Scott, S. Signoretti, N. Bardeesy, Y. A. Wang, D. E. Hill, T. R. Golub, M. J. Stampfer, W. H. Wong, M. Loda, L. Mucci, L. Chin and R. A. DePinho (2011). "SMAD4–dependent barrier constrains prostate cancer growth and metastatic progression." Nature **470**(7333): 269-273.

Ertl, G. and S. Frantz (2005). "Healing after myocardial infarction." Cardiovasc Res **66**(1): 22-32.

Fahlbusch, F. B., Y. Dawood, A. Hartner, C. Menendez-Castro, S. C. Nogel, A. Tzschoppe, H. Schneider, P. Strissel, M. W. Beckmann, E. Schleussner, M. Ruebner, H. G. Dorr, R. L. Schild, W. Rascher and J. Dotsch (2012). "Cullin 7 and Fbxw 8 expression in trophoblastic cells is regulated via oxygen tension: implications for intrauterine growth restriction?" J Matern Fetal Neonatal Med **25**(11): 2209-2215.

Fang, H., N. C. Lai, M. H. Gao, A. Miyanohara, D. M. Roth, T. Tang and H. K. Hammond (2012). "Comparison of adeno-associated virus serotypes and delivery methods for cardiac gene transfer." Hum Gene Ther Methods **23**(4): 234-241.

Franke, T. F. and L. C. Cantley (1997). "Apoptosis. A Bad kinase makes good." Nature **390**(6656): 116-117.

French, B. A. and B. H. Annex (2014). "AAV9 and Cre: a one-two punch for a quick cardiac knockout." Cardiovasc Res **104**(1): 3-4.

Geisler, A., A. Jungmann, J. Kurreck, W. Poller, H. A. Katus, R. Vetter, H. Fechner and O. J. Muller (2011). "microRNA122-regulated transgene expression increases specificity of cardiac gene transfer upon intravenous delivery of AAV9 vectors." Gene Ther **18**(2): 199-209.

Giacca, M. (2007). "Virus-mediated gene transfer to induce therapeutic angiogenesis: where do we stand?" Int J Nanomedicine **2**(4): 527-540.

Glickman, M. H. and A. Ciechanover (2002). "The ubiquitin-proteasome proteolytic pathway: destruction for the sake of construction." Physiol Rev **82**(2): 373-428.

Gomes, A. C., I. Falcão-Pires, A. L. Pires, C. Brás-Silva and A. F. Leite-Moreira (2013). "Rodent models of heart failure: an updated review." Heart Failure Reviews **18**(2): 219-249.

Gourdie, R. G., S. Dimmeler and P. Kohl (2016). "Novel therapeutic strategies targeting fibroblasts and fibrosis in heart disease." Nat Rev Drug Discov **15**(9): 620-638.

Gradman, A. H. and F. Alfayoumi (2006). "From left ventricular hypertrophy to congestive heart failure: management of hypertensive heart disease." Prog Cardiovasc Dis **48**(5): 326-341.

Greenberg, B. (2017). "Gene therapy for heart failure." Trends Cardiovasc Med **27**(3): 216-222.

Guo, H., F. Wu, Y. Wang, C. Yan and W. Su (2014). "Overexpressed ubiquitin ligase Cullin7 in breast cancer promotes cell proliferation and invasion via down-regulating p53." Biochem Biophys Res Commun **450**(4): 1370-1376.

Haddadi, N., Y. Lin, G. Travis, A. M. Simpson, N. T. Nassif and E. M. McGowan (2018). "PTEN/PTENP1: 'Regulating the regulator of RTK-dependent PI3K/Akt signalling', new targets for cancer therapy." Mol Cancer **17**(1): 37.

Haque, Z. K. and D. Z. Wang (2017). "How cardiomyocytes sense pathophysiological stresses for cardiac remodeling." Cell Mol Life Sci **74**(6): 983-1000.

Hartmann, T., X. Xu, M. Kronast, S. Muehlich, K. Meyer, W. Zimmermann, J. Hurwitz, Z. Q. Pan, S. Engelhardt and A. Sarikas (2014). "Inhibition of Cullin-RING E3 ubiquitin ligase 7 by simian virus 40 large T antigen." Proc Natl Acad Sci U S A **111**(9): 3371-3376.

Hasegawa, K., H. Tanaka, Y. Higuchi, M. Yamashita and H. Tsukahara (2016). "Changes in facial appearance from neonate to adult in 3-M syndrome patient with novel CUL7 gene mutations." J Pediatr Endocrinol Metab **29**(2): 241-246.

Hassink, R. J., H. Nakajima, H. O. Nakajima, P. A. Doevendans and L. J. Field (2009). "Expression of a transgene encoding mutant p193/CUL7 preserves cardiac function and limits infarct expansion after myocardial infarction." Heart **95**(14): 1159-1164.

Herrmann, A. K. and D. Grimm (2018). "High-Throughput Dissection of AAV-Host Interactions: The Fast and the Curious." J Mol Biol.

Hershko, A. and A. Ciechanover (1998). "The ubiquitin system." Annu Rev Biochem **67**: 425-479.

Huber, C., D. Dias-Santagata, A. Glaser, J. O'Sullivan, R. Brauner, K. Wu, X. Xu, K. Pearce, R. Wang, M. L. Uzielli, N. Dagoneau, W. Chemaitilly, A. Superti-Furga, H. Dos Santos, A. Megarbane, G. Morin, G. Gillessen-Kaesbach, R. Hennekam, I. Van der Burgt, G. C. Black, P. E. Clayton, A. Read, M. Le Merrer, P. J. Scambler, A. Munnich, Z. Q. Pan, R. Winter and V. Cormier-Daire (2005). "Identification of mutations in CUL7 in 3-M syndrome." Nat Genet **37**(10): 1119-1124.

Jugdutt, B. I. (2003). "Ventricular remodeling after infarction and the extracellular collagen matrix: when is enough enough?" Circulation **108**(11): 1395-1403.

Kadota, T., Y. Fujita, Y. Yoshioka, J. Araya, K. Kuwano and T. Ochiya (2017). "Emerging role of extracellular vesicles as a senescence-associated secretory phenotype: Insights into the pathophysiology of lung diseases." Mol Aspects Med.

Kasper, J. S., H. Kuwabara, T. Arai, S. H. Ali and J. A. DeCaprio (2005). "Simian virus 40 large T antigen's association with the CUL7 SCF complex contributes to cellular transformation." J Virol **79**(18): 11685-11692.

Kehat, I. and J. D. Molkentin (2010). "Molecular pathways underlying cardiac remodeling during pathophysiological stimulation." Circulation **122**(25): 2727-2735.

Kennedy, A. L., J. P. Morton, I. Manoharan, D. M. Nelson, N. B. Jamieson, J. S. Pawlikowski, T. McBryan, B. Doyle, C. McKay, K. A. Oien, G. H. Enders, R. Zhang, O. J. Sansom and P. D. Adams (2011). "Activation of the PIK3CA/AKT pathway suppresses senescence induced by an activated RAS oncogene to promote tumorigenesis." Mol Cell **42**(1): 36-49.

Kim, S. J., P. Angel, R. Lafyatis, K. Hattori, K. Y. Kim, M. B. Sporn, M. Karin and A. B. Roberts (1990). "Autoinduction of transforming growth factor beta 1 is mediated by the AP-1 complex." Mol Cell Biol **10**(4): 1492-1497.

Kim, S. S., M. Shago, L. Kaustov, P. C. Boutros, J. W. Clendening, Y. Sheng, G. A. Trentin, D. Barsyte-Lovejoy, D. Y. Mao, R. Kay, I. Jurisica, C. H. Arrowsmith and L. Z. Penn (2007). "CUL7 is a novel antiapoptotic oncogene." Cancer Res **67**(20): 9616-9622.

Klenotic, P. A., C. Zhang and Z. Lin (2016). "Emerging roles of CCN proteins in vascular development and pathology." J Cell Commun Signal **10**(3): 251-257.

Koegl, M., T. Hoppe, S. Schlenker, H. D. Ulrich, T. U. Mayer and S. Jentsch (1999). "A novel ubiquitination factor, E4, is involved in multiubiquitin chain assembly." Cell **96**(5): 635-644.

Kohrman, D. C. and M. J. Imperiale (1992). "Simian virus 40 large T antigen stably complexes with a 185-kilodalton host protein." J Virol **66**(3): 1752-1760.

Kong, C., J. J. Lange, D. Samovski, X. Su, J. Liu, S. Sundaresan and P. D. Stahl (2013). "Ubiquitination and degradation of the hominoid-specific oncoprotein TBC1D3 is regulated by protein palmitoylation." Biochem Biophys Res Commun **434**(2): 388-393.

Kong, C., D. Samovski, P. Srikanth, M. J. Wainszelbaum, A. J. Charron, J. Liu, J. J. Lange, P. I. Chen, Z. Q. Pan, X. Su and P. D. Stahl (2012). "Ubiquitination and degradation of the hominoid-specific oncoprotein TBC1D3 is mediated by CUL7 E3 ligase." PLoS One **7**(9): e46485.

Kravtsova-Ivantsiv, Y. and A. Ciechanover (2012). "Non-canonical ubiquitin-based signals for proteasomal degradation." J Cell Sci **125**(Pt 3): 539-548.

Kreusser, M. M., L. H. Lehmann, N. Wolf, S. Keranov, A. Jungmann, H. J. Grone, O. J. Muller, H. A. Katus and J. Backs (2016). "Inducible cardiomyocyte-specific deletion of CaM kinase II protects from pressure overload-induced heart failure." Basic Res Cardiol **111**(6): 65.

Kurosaki, F., R. Uchibori, N. Mato, Y. Sehara, Y. Saga, M. Urabe, H. Mizukami, Y. Sugiyama and A. Kume (2017). "Optimization of adeno-associated virus vector-mediated gene transfer to the respiratory tract." Gene Ther **24**(5): 290-297.

Kwon, Y. T. and A. Ciechanover (2017). "The Ubiquitin Code in the Ubiquitin-Proteasome System and Autophagy." Trends Biochem Sci **42**(11): 873-886.

Li, D. Z., S. F. Liu, L. Zhu, Y. X. Wang, Y. X. Chen, J. Liu, G. Hu, X. Yu, J. Li, J. Zhang, Z. X. Wu, H. Lu, W. Liu and B. Liu (2017). "FBXW8-dependent degradation of MRFAP1 in anaphase controls mitotic cell death." Oncotarget **8**(57): 97178-97186.

Li, L., D. Fan, C. Wang, J. Y. Wang, X. B. Cui, D. Wu, Y. Zhou and L. L. Wu (2011). "Angiotensin II increases periostin expression via Ras/p38 MAPK/CREB and ERK1/2/TGF-beta1 pathways in cardiac fibroblasts." Cardiovasc Res **91**(1): 80-89.

Li, Q., Y. Xu, X. Li, Y. Guo and G. Liu (2012). "Inhibition of Rho-kinase ameliorates myocardial remodeling and fibrosis in pressure overload and myocardial infarction: role of TGF-beta1-TAK1." Toxicol Lett **211**(2): 91-97.

Lindsey, M. L., R. P. Iyer, M. Jung, K. Y. DeLeon-Pennell and Y. Ma (2016). "Matrix metalloproteinases as input and output signals for post-myocardial infarction remodeling." J Mol Cell Cardiol **91**: 134-140.

Lindsey, M. L., A. Yabluchanskiy and Y. Ma (2015). "Tissue Inhibitor of Metalloproteinase-1: Actions beyond Matrix Metalloproteinase Inhibition." Cardiology **132**(3): 147-150.

Ling, H., T. Zhang, L. Pereira, C. K. Means, H. Cheng, Y. Gu, N. D. Dalton, K. L. Peterson, J. Chen, D. Bers and J. H. Brown (2009). "Requirement for Ca2+/calmodulin-dependent kinase II in the transition from pressure overload-induced cardiac hypertrophy to heart failure in mice." J Clin Invest **119**(5): 1230-1240.

Liu, Y., L. Fallon, H. A. Lashuel, Z. Liu and P. T. Lansbury, Jr. (2002). "The UCH-L1 gene encodes two opposing enzymatic activities that affect alpha-synuclein degradation and Parkinson's disease susceptibility." Cell **111**(2): 209-218.

Luo, J., Y. Luo, J. Sun, Y. Zhou, Y. Zhang and X. Yang (2015). "Adeno-associated virus-mediated cancer gene therapy: current status." Cancer Lett **356**(2 Pt B): 347-356.

Ma, Y., H. Zou, X. X. Zhu, J. Pang, Q. Xu, Q. Y. Jin, Y. H. Ding, B. Zhou and D. S. Huang (2017). "Transforming growth factor beta: A potential biomarker and therapeutic target of ventricular remodeling." Oncotarget **8**(32): 53780-53790.

Maillet, M., J. H. van Berlo and J. D. Molkentin (2013). "Molecular basis of physiological heart growth: fundamental concepts and new players." Nat Rev Mol Cell Biol **14**(1): 38-48.

Malumbres, M. and M. Barbacid (2001). "To cycle or not to cycle: a critical decision in cancer." Nat Rev Cancer **1**(3): 222-231.

Matsui, T., L. Li, F. del Monte, Y. Fukui, T. F. Franke, R. J. Hajjar and A. Rosenzweig (1999). "Adenoviral gene transfer of activated phosphatidylinositol 3'-kinase and Akt inhibits apoptosis of hypoxic cardiomyocytes in vitro." Circulation **100**(23): 2373-2379.

Matsui, T., J. Tao, F. del Monte, K. H. Lee, L. Li, M. Picard, T. L. Force, T. F. Franke, R. J. Hajjar and A. Rosenzweig (2001). "Akt activation preserves cardiac function and prevents injury after transient cardiac ischemia in vivo." Circulation **104**(3): 330-335.

McClements, M. E. and R. E. MacLaren (2017). "Adeno-associated Virus (AAV) Dual Vector Strategies for Gene Therapy Encoding Large Transgenes." Yale J Biol Med **90**(4): 611-623.

McDowell, G. S. and A. Philpott (2013). "Non-canonical ubiquitylation: mechanisms and consequences." Int J Biochem Cell Biol **45**(8): 1833-1842.

Meliani, A., F. Boisgerault, Z. Fitzpatrick, S. Marmier, C. Leborgne, F. Collaud, M. Simon Sola, S. Charles, G. Ronzitti, A. Vignaud, L. van Wittenberghe, B. Marolleau, F. Jouen, S. Tan, O. Boyer, O. Christophe, A. R. Brisson, C. A. Maguire and F. Mingozzi (2017). "Enhanced liver gene transfer and evasion of preexisting humoral immunity with exosome-enveloped AAV vectors." Blood Adv **1**(23): 2019-2031.

Men, X., L. Wang, W. Yu and Y. Ju (2015). "Cullin7 is required for lung cancer cell proliferation and is overexpressed in lung cancer." Oncol Res **22**(2): 123-128.

Meng, X. M., D. J. Nikolic-Paterson and H. Y. Lan (2016). "TGF-beta: the master regulator of fibrosis." Nat Rev Nephrol **12**(6): 325-338.

Meyer, K., B. Hodwin, D. Ramanujam, S. Engelhardt and A. Sarikas (2016). "Essential Role for Premature Senescence of Myofibroblasts in Myocardial Fibrosis." J Am Coll Cardiol **67**(17): 2018-2028.

Mingozzi, F., X. M. Anguela, G. Pavani, Y. Chen, R. J. Davidson, D. J. Hui, M. Yazicioglu, L. Elkouby, C. J. Hinderer, A. Faella, C. Howard, A. Tai, G. M. Podsakoff, S. Zhou, E. Basner-Tschakarjan, J. F. Wright and K. A. High (2013). "Overcoming preexisting humoral immunity to AAV using capsid decoys." Sci Transl Med **5**(194): 194ra192.

Mohammed, S. F., J. R. Storlie, E. A. Oehler, L. A. Bowen, J. Korinek, C. S. Lam, R. D. Simari, J. C. Burnett, Jr. and M. M. Redfield (2012). "Variable phenotype in murine transverse aortic constriction." Cardiovasc Pathol **21**(3): 188-198.

Mozaffarian, D., E. J. Benjamin, A. S. Go, D. K. Arnett, M. J. Blaha, M. Cushman, S. R. Das, S. de Ferranti, J. P. Despres, H. J. Fullerton, V. J. Howard, M. D. Huffman, C. R. Isasi, M. C. Jimenez, S. E. Judd, B. M. Kissela, J. H. Lichtman, L. D. Lisabeth, S. Liu, R. H. Mackey, D. J. Magid, D. K. McGuire, E. R. Mohler, 3rd, C. S. Moy, P. Muntner, M. E. Mussolino, K. Nasir, R. W. Neumar, G. Nichol, L. Palaniappan, D. K. Pandey, M. J. Reeves, C. J. Rodriguez, W. Rosamond, P. D. Sorlie, J. Stein, A. Towfighi, T. N. Turan, S. S. Virani, D. Woo, R. W. Yeh and M. B. Turner (2016). "Heart Disease and Stroke Statistics-2016 Update: A Report From the American Heart Association." Circulation **133**(4): e38-360.

Nakajima, H., H. O. Nakajima, S. C. Tsai and L. J. Field (2004). "Expression of mutant p193 and p53 permits cardiomyocyte cell cycle reentry after myocardial infarction in transgenic mice." Circ Res **94**(12): 1606-1614.

Naso, M. F., B. Tomkowicz, W. L. Perry and W. R. Strohl (2017). "Adeno-Associated Virus (AAV) as a Vector for Gene Therapy." BioDrugs **31**(4): 317-334.

Okabe, H., S. H. Lee, J. Phuchareon, D. G. Albertson, F. McCormick and O. Tetsu (2006). "A critical role for FBXW8 and MAPK in cyclin D1 degradation and cancer cell proliferation." PLoS One **1**: e128.

Olgar, Y., M. C. Celen, B. E. Yamasan, N. Ozturk, B. Turan and S. Ozdemir (2017). "Rho-kinase inhibition reverses impaired Ca(2+) handling and associated left ventricular dysfunction in pressure overload-induced cardiac hypertrophy." Cell Calcium **67**: 81-90.

Pacak, C. A., Y. Sakai, B. D. Thattaliyath, C. S. Mah and B. J. Byrne (2008). "Tissue specific promoters improve specificity of AAV9 mediated transgene expression following intra-vascular gene delivery in neonatal mice." Genet Vaccines Ther **6**: 13.

Paradis, V., M. Albuquerque, M. Mebarki, L. Hernandez, S. Zalinski, S. Quentin, J. Belghiti, J. Soulier and P. Bedossa (2013). "Cullin7: a new gene involved in liver carcinogenesis related to metabolic syndrome." Gut **62**(6): 911-919.

Pasumarthi, K. B., S. C. Tsai and L. J. Field (2001). "Coexpression of mutant p53 and p193 renders embryonic stem cell-derived cardiomyocytes responsive to the growth-promoting activities of adenoviral E1A." Circ Res **88**(10): 1004-1011.

Pfeffer, M. A. and E. Braunwald (1990). "Ventricular remodeling after myocardial infarction. Experimental observations and clinical implications." Circulation **81**(4): 1161-1172.

Philips, N., T. Keller and S. Gonzalez (2004). "TGF beta-like regulation of matrix metalloproteinases by anti-transforming growth factor-beta, and anti-transforming growth factor-beta 1 antibodies in dermal fibroblasts: Implications for wound healing." Wound Repair Regen **12**(1): 53-59.

Piek, A., R. A. de Boer and H. H. Sillje (2016). "The fibrosis-cell death axis in heart failure." Heart Fail Rev **21**(2): 199-211.

Pulicherla, N., S. Shen, S. Yadav, K. Debbink, L. Govindasamy, M. Agbandje-McKenna and A. Asokan (2011). "Engineering liver-detargeted AAV9 vectors for cardiac and musculoskeletal gene transfer." Mol Ther **19**(6): 1070-1078.

Ramanujam, D., Y. Sassi, B. Laggerbauer and S. Engelhardt (2016). "Viral vector-based targeting of miR-21 in cardiac non-myocyte cells reduces pathologic remodeling of the heart." Mol Ther.

Rockman, H. A., R. S. Ross, A. N. Harris, K. U. Knowlton, M. E. Steinhelper, L. J. Field, J. Ross, Jr. and K. R. Chien (1991). "Segregation of atrial-specific and inducible expression of an atrial natriuretic factor transgene in an in vivo murine model of cardiac hypertrophy." Proc Natl Acad Sci U S A **88**(18): 8277-8281.

Salama, R., M. Sadaie, M. Hoare and M. Narita (2014). "Cellular senescence and its effector programs." Genes Dev **28**(2): 99-114.

Sappino, A. P., W. Schurch and G. Gabbiani (1990). "Differentiation repertoire of fibroblastic cells: expression of cytoskeletal proteins as marker of phenotypic modulations." Lab Invest **63**(2): 144-161.

Sarikas, A., T. Hartmann and Z. Q. Pan (2011). "The cullin protein family." Genome Biol **12**(4): 220.

Sarikas, A., X. Xu, L. J. Field and Z. Q. Pan (2008). "The cullin7 E3 ubiquitin ligase: a novel player in growth control." Cell Cycle **7**(20): 3154-3161.

Scheufele, F. (2018). Generation and characterization of cardiomyocyte-specific inducible Cullin7 knock-out mice., Technische Universität München.

Scheufele, F., B. Wolf, M. Kruse, T. Hartmann, J. Lempart, S. Muehlich, A. F. Pfeiffer, L. J. Field, M. J. Charron, Z. Q. Pan, S. Engelhardt and A. Sarikas (2014). "Evidence for a regulatory role of Cullin-RING E3 ubiquitin ligase 7 in insulin signaling." Cell Signal **26**(2): 233-239.

Schirone, L., M. Forte, S. Palmerio, D. Yee, C. Nocella, F. Angelini, F. Pagano, S. Schiavon, A. Bordin, A. Carrizzo, C. Vecchione, V. Valenti, I. Chimenti, E. De Falco, S. Sciarretta and G. Frati (2017). "A Review of the Molecular Mechanisms Underlying the Development and Progression of Cardiac Remodeling." Oxid Med Cell Longev **2017**: 3920195.

Segura, A. M., O. H. Frazier and L. M. Buja (2014). "Fibrosis and heart failure." Heart Failure Reviews **19**(2): 173-185.

Seth, M., Z. S. Zhang, L. Mao, V. Graham, J. Burch, J. Stiber, L. Tsiokas, M. Winn, J. Abramowitz, H. A. Rockman, L. Birnbaumer and P. Rosenberg (2009). "TRPC1 channels are critical for hypertrophic signaling in the heart." Circ Res **105**(10): 1023-1030.

Shimizu, I. and T. Minamino (2016). "Physiological and pathological cardiac hypertrophy." J Mol Cell Cardiol **97**: 245-262.

Shioi, T., J. R. McMullen, O. Tarnavski, K. Converso, M. C. Sherwood, W. J. Manning and S. Izumo (2003). "Rapamycin attenuates load-induced cardiac hypertrophy in mice." Circulation **107**(12): 1664-1670.

Shiojima, I., K. Sato, Y. Izumiya, S. Schiekofer, M. Ito, R. Liao, W. S. Colucci and K. Walsh (2005). "Disruption of coordinated cardiac hypertrophy and angiogenesis contributes to the transition to heart failure." J Clin Invest **115**(8): 2108-2118.

Singla, D. K. (2015). "Akt-mTOR Pathway Inhibits Apoptosis and Fibrosis in Doxorubicin-Induced Cardiotoxicity Following Embryonic Stem Cell Transplantation." Cell Transplant **24**(6): 1031-1042.

Skaar, J. R., L. Florens, T. Tsutsumi, T. Arai, A. Tron, S. K. Swanson, M. P. Washburn and J. A. DeCaprio (2007). "PARC and CUL7 form atypical cullin RING ligase complexes." Cancer Res **67**(5): 2006-2014.

Sohal, D. S., M. Nghiem, M. A. Crackower, S. A. Witt, T. R. Kimball, K. M. Tymitz, J. M. Penninger and J. D. Molkentin (2001). "Temporally regulated and tissue-specific gene manipulations in the adult and embryonic heart using a tamoxifen-inducible Cre protein." Circ Res **89**(1): 20-25.

Spaich, S., H. A. Katus and J. Backs (2015). "Ongoing controversies surrounding cardiac remodeling: is it black and white-or rather fifty shades of gray?" Front Physiol **6**: 202.

Srivastava, A. (2016). "In vivo tissue-tropism of adeno-associated viral vectors." Curr Opin Virol **21**: 75-80.

Strack, R. L., R. J. Keenan and B. S. Glick (2011). "Noncytotoxic DsRed derivatives for whole-cell labeling." Methods Mol Biol **699**: 355-370.

Strack, R. L., D. E. Strongin, D. Bhattacharyya, W. Tao, A. Berman, H. E. Broxmeyer, R. J. Keenan and B. S. Glick (2008). "A noncytotoxic DsRed variant for whole-cell labeling." Nat Methods **5**(11): 955-957.

Szabo, Z., J. Magga, T. Alakoski, J. Ulvila, J. Piuhola, L. Vainio, K. I. Kivirikko, O. Vuolteenaho, H. Ruskoaho, K. E. Lipson, P. Signore and R. Kerkela (2014). "Connective tissue growth factor inhibition attenuates left ventricular remodeling and dysfunction in pressure overload-induced heart failure." Hypertension **63**(6): 1235-1240.

Tanaka, K., T. Suzuki, N. Hattori and Y. Mizuno (2004). "Ubiquitin, proteasome and parkin." Biochim Biophys Acta **1695**(1-3): 235-247.

Tham, Y. K., B. C. Bernardo, J. Y. Ooi, K. L. Weeks and J. R. McMullen (2015). "Pathophysiology of cardiac hypertrophy and heart failure: signaling pathways and novel therapeutic targets." Arch Toxicol **89**(9): 1401-1438.

Toba, H., P. L. Cannon, A. Yabluchanskiy, R. P. Iyer, J. D'Armiento and M. L. Lindsey (2017). "Transgenic overexpression of macrophage matrix metalloproteinase-9 exacerbates age-related cardiac hypertrophy, vessel rarefaction, inflammation, and fibrosis." Am J Physiol Heart Circ Physiol **312**(3): H375-h383.

Tsai, S. C., K. B. Pasumarthi, L. Pajak, M. Franklin, B. Patton, H. Wang, W. J. Henzel, J. T. Stults and L. J. Field (2000). "Simian virus 40 large T antigen binds a novel Bcl-2 homology domain 3-containing proapoptosis protein in the cytoplasm." J Biol Chem **275**(5): 3239-3246.

Tsutsumi, T., H. Kuwabara, T. Arai, Y. Xiao and J. A. Decaprio (2008). "Disruption of the Fbxw8 gene results in pre- and postnatal growth retardation in mice." Mol Cell Biol **28**(2): 743-751.

van Berlo, J. H., M. Maillet and J. D. Molkentin (2013). "Signaling effectors underlying pathologic growth and remodeling of the heart." J Clin Invest **123**(1): 37-45.

Vliegen, H. W., A. van der Laarse, C. J. Cornelisse and F. Eulderink (1991). "Myocardial changes in pressure overload-induced left ventricular hypertrophy. A study on tissue composition, polyploidization and multinucleation." Eur Heart J **12**(4): 488-494.

Wang, H., Y. Chen, P. Lin, L. Li, G. Zhou, G. Liu, C. Logsdon, J. Jin, J. L. Abbruzzese, T. H. Tan and H. Wang (2014). "The CUL7/F-box and WD repeat domain containing 8 (CUL7/Fbxw8) ubiquitin ligase promotes degradation of hematopoietic progenitor kinase 1." J Biol Chem **289**(7): 4009-4017.

Wang, L., Y. Lu, X. Liu and X. Wang (2017). "Ghrelin protected neonatal rat cardiomyocyte against hypoxia/reoxygenation injury by inhibiting apoptosis through Akt-mTOR signal." Mol Biol Rep **44**(2): 219-226.

Wei, M., X. Zhao, M. Liu, Z. Huang, Y. Xiao, M. Niu, Y. Shao and L. Kleiman (2015). "Inhibition of HIV-1 assembly by coiled-coil domain containing protein 8 in human cells." Sci Rep **5**: 14724.

Weinheimer, C. J., L. Lai, D. P. Kelly and A. Kovacs (2015). "Novel mouse model of left ventricular pressure overload and infarction causing predictable ventricular remodelling and progression to heart failure." Clin Exp Pharmacol Physiol **42**(1): 33-40.

Werfel, S., A. Jungmann, L. Lehmann, J. Ksienzyk, R. Bekeredjian, Z. Kaya, B. Leuchs, A. Nordheim, J. Backs, S. Engelhardt, H. A. Katus and O. J. Muller (2014). "Rapid and highly efficient inducible cardiac gene knockout in adult mice using AAV-mediated expression of Cre recombinase." Cardiovasc Res **104**(1): 15-23.

WHO. (2015). "http://www.who.int/mediacentre/factsheets/fs310/en/."

Wu, Q. Q., Y. Xiao, Y. Yuan, Z. G. Ma, H. H. Liao, C. Liu, J. X. Zhu, Z. Yang, W. Deng and Q. Z. Tang (2017). "Mechanisms contributing to cardiac remodelling." Clin Sci (Lond) **131**(18): 2319-2345.

Xi, J., S. T. Zeng, L. Guo and J. Feng (2016). "High Expression of Cullin7 Correlates with Unfavorable Prognosis in Epithelial Ovarian Cancer Patients." Cancer Invest **34**(3): 130-136.

Xu, X., A. Sarikas, D. C. Dias-Santagata, G. Dolios, P. J. Lafontant, S. C. Tsai, W. Zhu, H. Nakajima, H. O. Nakajima, L. J. Field, R. Wang and Z. Q. Pan (2008). "The CUL7 E3 ubiquitin ligase targets insulin receptor substrate 1 for ubiquitin-dependent degradation." Mol Cell **30**(4): 403-414.

Xu, Y., Q. Gu, J. Tang, Y. Qian, X. Tan, Z. Yu and C. Qu (2017). "Substance P Attenuates Hypoxia/Reoxygenation-Induced Apoptosis Via the Akt Signalling Pathway and the NK1-Receptor in H9C2Cells." Heart Lung Circ.

Yao, H., X. Han and X. Han (2014). "The cardioprotection of the insulin-mediated PI3K/Akt/mTOR signaling pathway." Am J Cardiovasc Drugs **14**(6): 433-442.

Zaiss, A. K., Q. Liu, G. P. Bowen, N. C. Wong, J. S. Bartlett and D. A. Muruve (2002). "Differential activation of innate immune responses by adenovirus and adeno-associated virus vectors." J Virol **76**(9): 4580-4590.

Zhang, D., G. Yang, X. Li, C. Xu and H. Ge (2016). "Inhibition of Liver Carcinoma Cell Invasion and Metastasis by Knockdown of Cullin7 In Vitro and In Vivo." Oncol Res **23**(4): 171-181.

Zhang, L., F. Zhou and P. ten Dijke (2013). "Signaling interplay between transforming growth factor-beta receptor and PI3K/AKT pathways in cancer." Trends Biochem Sci **38**(12): 612-620.

Zhou, J., J. Lin, C. Zhou, X. Deng and B. Xia (2011). "Cytotoxicity of red fluorescent protein DsRed is associated with the suppression of Bcl-xL translation." FEBS Lett **585**(5): 821-827.

Ziegler, T., K. Ishikawa, R. Hinkel and C. Kupatt (2018). "Translational aspects of AAV-mediated cardiac gene therapy." Hum Gene Ther.

Zincarelli, C., S. Soltys, G. Rengo and J. E. Rabinowitz (2008). "Analysis of AAV serotypes 1-9 mediated gene expression and tropism in mice after systemic injection." Mol Ther **16**(6): 1073-1080.